



Vrije Universiteit Brussel

Faculteit Wetenschappen en Bio-ingenieurswetenschappen
Vakgroep Fysica- Interuniversity Institute for High Energies

**Search for high-energy neutrinos from
obscured flat spectrum radio AGN using
the IceCube neutrino observatory**

Giuliano Alexander Maggi Olmedo

Proefschrift ingediend met het oog op het behalen van de academische
graad van Doctor in de Wetenschappen

Promotor: **Prof. Dr. Nick van Eijndhoven**
Co-promotor: **Dr. Krijn D. de Vries**

Brussel, België
June 2017

Doctoral Examination Committee

Prof. Nick van Eijndhoven (promotor), VUB-DNTK
Dr. Krijn de Vries (co-promotor), VUB-DNTK
Prof. Jorgen D'Hondt (voorzitter), VUB-DNTK
Prof. Stijn Buitink (secretaris), VUB-DNTK
Prof. Dominique Maes, VUB-DBIT
Prof. Alberto Mariotti, VUB-DNTK
Prof. Julia Tjus, University of Bochum (Germany)
Prof. Kumiko Kotera, Institut d'Astrophysique de Paris (IAP, France)

Esta tesis la dedico a mis padres, Patricia y Hernán.

Contents

Acknowledgements	6
1 Introduction	7
2 Physics processes in (obscured) AGN	12
2.1 AGN Components	15
2.2 The AGN Spectral Features	18
2.3 Blazars	27
2.4 AGN Obscuration	30
2.4.1 Ionized material in obscured AGN	31
3 Neutrino Production in AGN	36
3.1 Neutrino Overview	36
3.2 Neutrino Production in AGN	41
3.2.1 Neutrino energy in $p\gamma$ interaction.	44
3.2.2 Neutrino Production in Obscured AGN	45
4 Obscured Flat Spectrum Radio AGN.	52
4.1 The Catalogs	53
4.2 A Limited Volume Sample of Galaxies	57
4.3 Flat Spectrum Radio AGN	58
4.4 Limited Volume Flat Spectrum Radio AGN	62
4.5 Obscured Flat Spectrum Radio AGN Selection	64
4.5.1 Obscured Flat Spectrum Radio AGN Population	68
4.5.2 Estimation of the fraction of protons interacting with the obscuring material in Obscured Flat Spectrum Ra- dio AGN	71

5	The IceCube Neutrino Observatory	78
5.1	The IceCube Detector	78
5.1.1	Detector Location and Geometry	78
5.1.2	The Various Signals in the Detector	80
5.1.3	Triggering Filtering and Transfer System	87
5.2	Event Simulation in the IceCube Experiment.	89
5.3	Other Directional Reconstructions at Level2	91
5.4	High Performance Track Directional Reconstructions	93
5.4.1	SplineReco Directional Reconstruction	93
5.4.2	Paraboloid, a Directional Uncertainty Estimator	94
6	Statistical Concepts	99
6.1	The Likelihood function	100
6.2	Test Statistic	103
6.3	Discovery Potential	103
6.4	The Sensitivity	104
7	IceCube Event Selection for the Obscured Flat Spectrum	
	Radio AGN Population	106
7.1	The Point Source Event Selection	108
7.1.1	Point Source BDT Variables	110
7.2	An Alternative Event Selection	113
7.2.1	BDT Performance in the Alternative Event Selection	116
7.2.2	Event Selection Results in terms of the Discovery Potential	119
7.3	Comparison between the Alternative Sample and the Standard Point Source Sample.	120
7.4	The Final Sample for this Analysis, “The Reprocessed Point Source Sample”	129
8	Results and Discussion	134
	Summary	140
	Outlook	143
	Abbreviations	145
	Appendices	161

A	Table with AGN in a limited volume sample and with a radio jet pointing towards Earth	162
B	BDT Variables	165
C	Comparison between the Reprocessed Point Source and Diffuse Samples	171
D	Test Statistic Background Distribution for the Obscured Flat Spectrum Radio AGN	174

Acknowledgements

I would like to thank the people that supported me during my PhD, both on an academic as well as on a personal level.

Thanks a lot to all my friends for sharing your time and nice moments we had during my stay in Brussels. I really had a great time with them, specially with Estefanía and Mauricio.

I thank my colleagues for providing the friendly environment that we have in the IIHE, and the discussions that helped with my work. I consider many of them as friends as well, Elisa, Jan K., Jan L. and Krijn.

I thank my supervisor, Nick van Eijndhoven, first for accepting me as his PhD student, and for proposing me a great research project, from which I earned the experience as an experimental physicist, as well as the phenomenological aspects of AGN. I appreciate a lot all the help given by the secretary of the VUB-IIHE, Marleen Goeman.

I also would like to thank the IceCube Collaboration, mainly the Point Source working group, for the great discussions about the analysis presented in this thesis. Furthermore, I appreciate a lot all the support that I received from the IceCube software coordinator, Alex Olivas, and the whole IceCube Software Strike Team. I indeed learned a lot working with them.

In the last part of my thesis, the remarks provided by the jury members for evaluating my PhD work were extremely valuable, thanks a lot all the members of my jury.

Chapter 1

Introduction

Currently, one of the main open issues in astroparticle physics is to find the origin of the cosmic-rays, which were proposed in 1912 by Victor Hess to explain the increase of the radiation at increasing altitudes [1]. Several experiments have been initiated to detect cosmic-rays, find out the type of particles they are, and mainly, to answer the question of the origin of those extraterrestrial particles. Currently, the main experiments are the Pierre Auger Observatory [2] and the Telescope Array Experiment [3]. They indeed have measured the energy spectrum and investigated the cosmic-ray composition [4, 5], which might range from protons to nuclei of Iron [6]. Nevertheless, the question of their origin has not been answered yet [7]. The main reason that cosmic-ray sources have not yet been identified is due to the fact that most cosmic-rays are charged particles, which implies that they are deflected by (inter) galactic magnetic fields.

However, there is some consensus about the possible origin of Ultra High Energy Rays (UHECRs) above 10^{18} eV. Their origin is believed to be from extragalactic sources since the galactic magnetic field is not able to contain them. This approach can be understood through the Larmor radius $r_L = 1.08 \text{pc} \frac{E/\text{PeV}}{Z \cdot B/\mu\text{G}}$ [8, 9, 10], and the so-called, Hillas diagram [11], which shows a relation between magnetic field strength B and the extension R of source candidates as can be seen from fig. 1.1. This indicates that the more potential sources of UHECRs above 10^{18} eV are Active Galactic Nuclei (AGN) and Gamma Ray Bursts (GRBs), where the general accepted mechanism for high-energy particle production is Fermi shock acceleration [12].

A GRB is one of the more violent and energetic astrophysical events which takes place at the end of the life of a massive star [13]. When a star

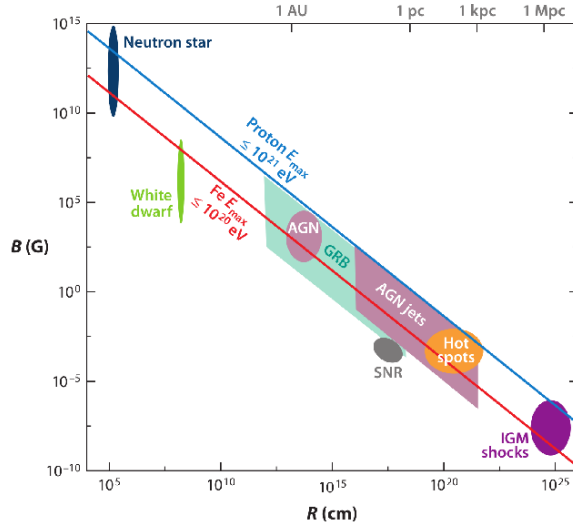


Figure 1.1: The Hillas diagram, which shows source candidates for UHECRs. Uncertainties are shown on the parameters of the astrophysical candidates. Credit: Kotera & Olinto [10]

runs out of fuel, the thermal force can not balance the gravitational force and the star collapses and forms a extremely dense object, as a Black Hole. In a few seconds, this can release more energy than the sun would emit in its entire life. Part of this energy is emitted in a jet, which could contain UHECRs and photons [10, 14, 15, 16, 13, 17, 18, 19, 20, 21].

An Active Galactic Nucleus (AGN) is regarded to be the compact core of a galaxy, which has an extremely massive Black Hole in its center. The Black Hole is surrounded by an accretion disc, which is formed by matter falling into the Black Hole and producing ambient photons [22]. Often an AGN contains a jet perpendicular to its accretion disc, and if the jet exists and is pointing towards us, we call the object a Blazar. If hadronic acceleration takes place in the jet, cosmic-rays can be accelerated to extreme energies up to several EeV.

In case hadronic acceleration takes place in an astrophysical environment, UHECRs might interact with ambient photons in the jet ($p\gamma$). This intercation can produce a shower of several hadrons as long as the process reaches certain energy thresholds, whereas some of these hadrons can decay and produce high-energy neutrinos. Several authors aim to the $p\gamma$ interaction as the main mechanism for producing astrophysical high-energy neut-

rinos (see for example [20, 21, 18]). However, in this thesis we will consider an unexplored class of objects until now, which may give rise to additional processes for producing astrophysical high-energy neutrinos, which is lead by proton-matter interaction.

High-energy neutrinos play an important role in the study of the origin of UHECRs. Due to the fact that neutrinos are chargeless particles and have a very low interaction probability compared with other particles, for example photons, they can travel long distances in the Universe without being affected by extragalactic magnetic fields and are rarely attenuated by matter in the intergalactic medium. These special neutrino characteristics make neutrinos to play an important role as a messenger of astrophysical phenomena. Furthermore, astrophysical neutrino detection can be associated with other astrophysical messengers as cosmic-rays, photons and gravitational waves, providing complementary information on the underlying (astro)physical processes. In view of this, recently a network of astrophysical partner observatories has been formed, called: Astrophysical Multimessenger Observatory Network (AMON) [23], which aims to study cosmic events using these astrophysical multimessengers.

Due to the small neutrino cross section, large volume detectors have to be built to detect these weakly interacting particles. Examples are the Baikal detector [24] in the Siberian lake Baikal, the ANTARES detector in the Mediterranean sea [25] and the IceCube Neutrino Observatory at the South Pole [26].

Despite their low interaction rate and the high background rate coming from atmospherical events, the detection of astrophysical high-energy neutrino is hard but not imposible. the IceCube Collaboration already reported in 2013 the detection of two high-energy neutrinos events with an energy of a few PeV, which opened up the field of the neutrino astronomy. The IceCube Collaboration made a follow up analysis of those two high-energy neutrino events, obtaining a first evidence for the detection of High-Energy Extraterrestrial Neutrinos [27, 28]. Nevertheless, so far, their sources are unknown.

IceCube also reported an upper limit on the flux of high-energy neutrinos associated with the prompt emission of GRBs [29, 30]. This upper limit is lower than the model predictions [14, 15, 17, 20]. As is explained in [29]: “This implies that GRBs are not the only sources of cosmic rays with energies $> 10^{18}$ eV or that the efficiency of neutrino production is much lower than has been predicted” (see direct citation in: second page as written in arXiv:1204.4219). After high-energy neutrino emission from prompt GRBs got ruled out, AGN became the more interesting candidates to search for

high-energy neutrino emission.

AGN have been investigated by the IceCube Collaboration as well. Nevertheless, also here no significant evidence for high-energy neutrino emission has been observed. For instance, results shown in [31] based on very bright AGN, with emission at high-energies in the electromagnetic spectrum did not show a strong correlation. Another example is what is described in [32]; here the investigated AGN are characterized by emitting flares and by investigating a time correlation with γ -ray as detected by The Fermi satellite [33]. Neither here neutrino signal was found. Consequently, upper limits have been set for the investigated objects.

As pointed out above, until now, several authors in the neutrino astronomy field aim the photo-meson production as the main mechanism to produce astrophysical high-energy neutrinos. In this thesis, it is presented a search for astrophysical high-energy neutrino emission from a specific class of AGN, starting from a different approach. This idea consists of an AGN that could be surrounded by a column of dust, gas or a combination of both, which in addition has a radio jet pointing towards us. Consequently, if there is hadronic acceleration in the jet, for example proton acceleration, these hadrons can interact with the surrounding dust yielding a hadron beam dump in addition to the $p\gamma$ interactions. This process would produce a shower of hadrons, like for instance charged pions and kaons, that subsequently will decay producing neutrinos. In this scenario the high-energy neutrino flux increases compared to the $p\gamma$ scenario only. This implies that the neutrino detection probability at Earth would be larger than by searching just for high-energy neutrinos coming from bright AGN that have a jet pointing towards us, but are not surrounded by dust. Hence, the class of AGN that is aimed at in this thesis are, so-called, *Obscured Flat Spectrum Radio AGN*, which is introduced in [34, 35].

Obscured Flat Spectrum Radio AGN are also characterized by a low X -ray intensity due to it is attenuated by the column of dust that surrounds the AGN. This causes the phenomenon of AGN Obscuration, hence the column of dust also will be called “Obscuring Material”. The level of X -ray attenuation will be correlated with the amount of protons that will interact with the obscuring material, and consequently give indications of the amount of neutrinos that will be produced in certain Obscured Flat Spectrum Radio AGN.

Due to a hadronic acceleration that is expected in Obscured AGN, these objects are thought to be sources of cosmic-rays. Nevertheless, in case of an obscured AGN, a cosmic-ray flux is expected to be reduced due to the beam dump effect. Therefore, this class of AGN falls into of what is known

as “Hidden Cosmic Ray Accelerators” [36]. This has been proposed in view of the tension between the high-energy neutrinos detected by IceCube and the γ -rays observed by the Fermi Space Telescope [33]. The lack of γ -rays as measured by the Fermi observatory, might be attributed to an absorber for the highest frequencies in the electromagnetic band that is located in the line of sight of the γ -ray telescope. Hence, if Obscured AGN are the sources that emit high-energy neutrinos, the γ -ray flux from this class of AGN is expected to be attenuated due to the obscuring material in our line of sight, as well as the cosmic-ray flux.

Since AGN are crucial in this thesis, I will start with a review of AGN, as outlined in Chapter 2. This review includes a discussion of the AGN components, the electromagnetic AGN emission and other relevant features that will be used in this analysis. This is followed by Chapter 3, which explains the different particle physics processes that can take place in AGN, specially in an Obscured Flat Spectrum Radio AGN. Afterwards, a method to select Obscured Flat Spectrum Radio AGN is presented in Chapter 4, which is based on the orientation of the AGN radio jet, and the level of X -ray attenuation. In this thesis the neutrino emission from Obscured Flat Spectrum Radio AGN has been studied using data and resources from the IceCube Collaboration. Consequently, in Chapter 5, an overview of the IceCube detector is presented. This is followed in Chapter 7 by a description of the IceCube event selection that was developed for the selected AGN population listed in Chapter 4.

This thesis ends with the presentation of the results of the search for neutrino emission from Obscured Flat Spectrum Radio AGN with the IceCube neutrino observatory, which is exposed in Chapter 8. This analysis has been performed by analyzing four years of IceCube data (2012-2015), and searching for a directional correlation between the observed neutrinos and the investigated Obscured Flat Spectrum Radio AGN.

Chapter 2

Physics processes in (obscured) AGN

In this thesis we investigate a sub-class of AGN, as described in Chapter 4. Thus, it is instructive to review the components, radiation processes and main features of an AGN.

An Active Galactic Nucleus (AGN) is the central part of a galaxy hosting a massive Black Hole, which is surrounded by an accretion disk, and often perpendicular to this disk two back to back relativistic jets. Besides that, an AGN has some dust components, a wide dusty torus with the shape of a donut, and further away from the torus a cloud of dust [22]. In fig. 2.1 a view of the different components of an AGN can be seen. The galaxies that are hosting these kind of objects are named active galaxies, for distinguishing them from the inactive galaxies [22], also called normal or regular galaxies.

Until 2011 we had knowledge of a million of AGN, classified by their color, spectroscopy and redshift [22]. This classification implies that they can adopt different names according to those characteristics, subsequently, they can be grouped by categories. Three of the more commonly used categories are: *Seyfert Galaxies*, *Quasars* and *Blazars*. The spectra of these three classes of AGN differ mainly in their radio observations, due to the boost of low frequency emission to higher energies of the electromagnetic spectra. As will be explained along this Chapter, the boosting effect is related to the viewing angle to the AGN. As illustrated in fig. 2.2, Blazars are AGN viewed directly inside of the jet, therefore, the radio spectra of Blazars are stronger than Seyfert galaxies and Quasars.

On the other hand, Quasars are the brightest objects in the universe. The brightness provides a division criterium with respect to Seyfert Galax-

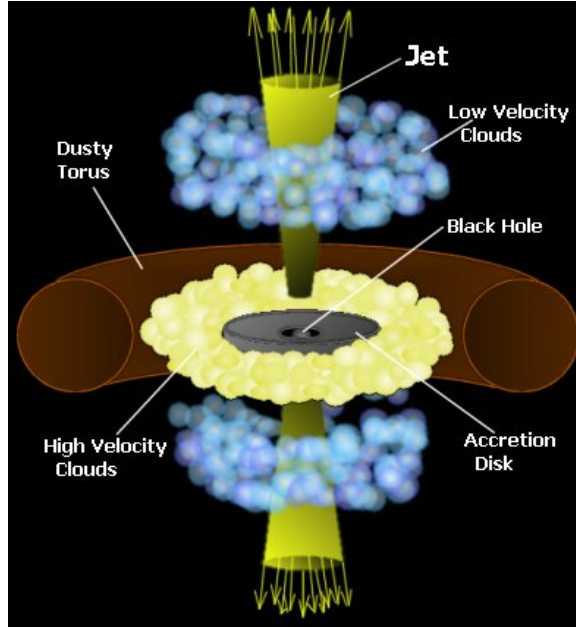


Figure 2.1: An artistic view of an AGN with its main 5 components. Credits: [37].

ies, which are low-luminosity sources. Some authors propose that the bolometric luminosity of the central source to distinguish Seyfert Galaxies from Quasars should be $L_{bol} = 10^{45} \text{erg s}^{-1}$ [22]. Another feature for distinguishing Quasars from Seyfert Galaxies is that the former are believed to exist for a long time due to their large redshifts. Hence, often an AGN with a redshift ≥ 0.2 is classified as a Quasar [22].

Notice that the AGN “zoo” is larger, and sources can not only be classified according to their viewing angle. As indicated in fig. 2.3, they can also be classified by their radio loudness. In a radio loud object, a large fraction of the bolometric luminosity originates from radio emission from the jet, whereas in a radio quiet source this is rather insignificant [38]. The differences between radio loud and quiet galaxies could be associated with the spin of the central black hole [38].

Within the radio galaxies, we can distinguish a sub-class, called Fanaroff-Riley (FR) galaxies, which are radio loud galaxies with an AGN. This category can be divided in FR-I and FR-II objects, where the latter have a brighter core and jet than the former [39]. Furthermore, the brightest regions in FR-I objects are located closer to the central engine than those of

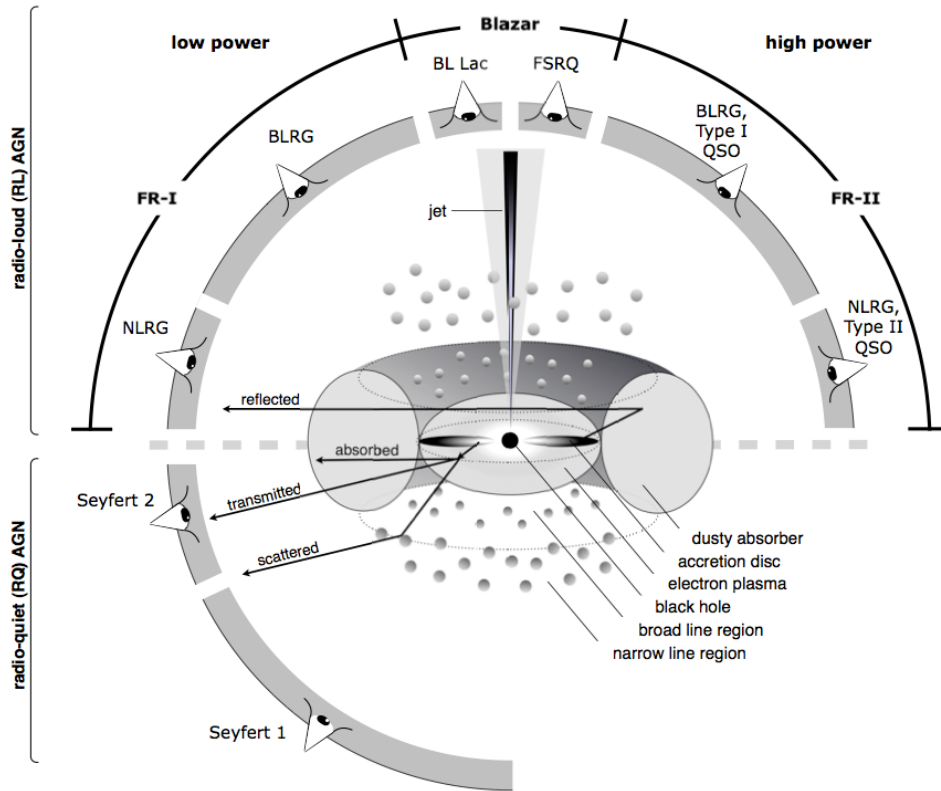


Figure 2.2: The unified AGN Model. Credits: Beckmann & Shrader (2012).

thee FR-II ones. This may reflect a more powerful jet and consequently a more beamed acceleration for the FR-II objects compared to the FR-I ones. In addition, in the “Unified Schemes” of AGN, a BL Lac object can be thought of as an FR-I galaxy, but with a small viewing angle with respect to the jet, between 20-30 degrees [40]. By contrast, FSRQ are thought to be FR II galaxies with a viewing angle smaller than 15° with respect to the jet.

In absence of dense material in astrophysical objects, we would see a continuous emission within the electromagnetic spectrum. Nonetheless, we observe emission and absorption lines from astrophysical sources, which can be caused by dust or gas clouds surrounding the astrophysical object. In the case of AGN, the width of the optical emission lines constitute a different manner for AGN classification, referred to as Type 1 and Type 2. Type 1

Radio Loudness	Optical Emission Line Properties		
	Type 2 (Narrow Line)	Type 1 (Broad Line)	Type 0 (Unusual)
Radio-quiet:	Seyfert 2	Seyfert 1 QSO	
Radio-loud:	FRI NLRG { FR II	BLRG SSRQ FSRQ	BL Lacs Blazars { (FSRQ)
	decreasing angle to line of sight ->		

Table 1: AGN Taxonomy: A Simplified Scheme.

Figure 2.3: AGN classification according to different properties. FR refers to Fanaroff-Riley galaxies, NLRG means Narrow Line Radio Galaxy, BLRG indicates Broad Line Radio Galaxy and SSRQ is the abbreviation for Steep Spectrum Radio Quasars. Credits: [40].

AGN have broader emission lines than Type 2 AGN [40], where the width of the emission lines can be attributed, for example, to the temperature and velocity of the material that absorbs the central radiation, which gives rise to Doppler Broadening. As illustrated in fig. 2.2 and exposed in fig. 2.3, Type 2 AGN are objects that are seen at large viewing angles with respect to the jet. In this case, the broad line emission, which originates from the hot central part of the AGN, is blocked by the dusty torus, giving place to narrow line emission.

2.1 AGN Components

As mentioned above, one can distinguish 5 main components in an AGN: a Black Hole, an Accretion Disk, a Dusty Torus, a Relativistic Jet and a Cloud of Dust. In this section a description for those components is given.

- A Black Hole is an astrophysical object formed for instance after the death of a massive star. The star collapses because its engine is not longer able to produce radiation pressure, after which, the pressure due to the gravitational force wins over the radiation force leading to collapse [41]. Subsequently, an enormous amount of matter is left in a small region of space deforming the space time. Black Holes are

predicted by the theory of general relativity [42] and the first direct detection of gravitational waves resulting from the merger of two black holes was reported in 2016 by The Ligo collaboration [43].

The radiation emission process from an AGN is not completely clear so far, nevertheless, the engine to produce energy in an AGN is due to the accretion of matter onto a Black Hole. The emitted energy from AGN is limited by the so-called Eddington luminosity [22, 44], defined as:

$$L_{Edd} = \frac{4\pi cGM\mu m_p}{\sigma_T} = 1.5 \cdot 10^{38} (M/M_\odot) \text{erg s}^{-1}, \quad (2.1)$$

where σ_T is the Thompson cross section [45, 46], μ the mean number of nucleons per electron and m_p is the mass of the proton.

The Eddington luminosity L_{Edd} is the maximum luminosity that an astrophysical object of mass M can emit in a certain amount of time. The above equation arises from the astrophysical body condition $f_{rad} = f_g$, where f_{rad} and f_g are the radiation force acting on a gas particle of mass m_p and the gravitational force per particle respectively. If $f_{rad} > f_g$, the gas is simply blown away. By contrast, if $f_{rad} < f_g$ a spherical accretion of fully ionized gas onto the Black Hole takes place.

- The Accretion Disk is a disk shaped amount of matter rotating around of the Black Hole. While the disk is rotating around its axes, the gas, which composes it, falls into the Black Hole. Subsequently, gravitational potential energy is converted into kinetic energy, which in turn can be transformed in electromagnetic radiation [22]. However, due to the increase in kinetic energy the gas can also escape from the disk. This boosted gas also can interact with regions of gas in the disk, subsequently, heating the gas to very high temperatures. The produced radiation, as a result of those processes, can be observed at frequencies in the electromagnetic spectrum as infrared, ultraviolet and X-ray.

In an initial state, the matter falling into the Black Hole is at low temperature, hence, when the matter starts to fall in, the temperature grows, which regulates the temperatures in the disk and the overall luminosity. The rate at which the temperatures and luminosity increase, is directed by the mass and spin of the Black Hole [47]. As the mass and spin of the Black Hole increase, the accretion process is faster, and the energy conversion is accelerated.

- The Dusty Torus is a column of matter in shape of a torus or donut wrapping around the accretion disk and the Black Hole, depending of the line of sight. In general this torus, as shown in fig. 2.1, is in the same plane as the accretion disk and perpendicular to the Jet. Nevertheless, as will be explained in section 2.4, sometimes this torus could be tilted, giving rise to the *AGN obscuration phenomenon*.

The AGN-torus is the outer part of an AGN, which can extend from 0.1 to 10 pc from the central Black Hole [48], containing matter in dust and gas state. As mentioned before, the central Black Hole properties, as its mass, define what happens in its nearby area, and consequently, the gas density in the torus can range from $10^4 - 10^7 \text{ cm}^{-3}$ [22]. The broad range of densities implies different torus configurations like a continuous density (continuous torus) or with gaps giving place to a clumpy structure (clumpy torus). The emitted spectrum in both cases can show different signatures [49]. The AGN-torus description will be extended in section 2.4, since the torus properties play an important role in our discussion of Obscured Flat Spectrum Radio AGN.

- Clouds of Dust: As shown in fig. 2.1, some clouds of material may be located away from the accretion disk, moving at very high speed, which prevents them from falling into the accretion disk. These clouds of dust can reach high temperatures due to the interaction with the jet.

Another feature of this cloudy region is related to broad emission lines, which can be attributed to a Keplerian motion of these dust concentrations [49], so-called Comets. This Keplerian motion has been observed in AGN and produces a strong X-ray variability [50].

- The relativistic AGN-jet is a jet perpendicular to the accretion disk, with an extension from parsec to megaparsec scales [51]. Currently, the jet formation is unknown, nevertheless, the more common consensus about how this might be formed, which suggests that the matter falling into the Black Hole releases gravitational binding energy which is converted into kinetic energy of the ejected matter along the rotational axes of the accretion disk [52].

A well known example of an AGN with a jet, is the radio galaxy Cygnus A. This AGN shows the jet structure reaching out from the center of the galaxy [53]. In fig. 2.4, the Cygnus A galaxy is shown, displaying the presence of two back to back jets in the shape of lobes which are extended along $\sim \text{kpc}$ scales.

An AGN-jet is known to emit in multiple wavelengths as γ -ray, X -ray, UV and mainly in radio. Moreover, the emission in the radio band of the electromagnetic spectrum was an important key to discover the lobe structure as explained in [53]. Here, the radio emission is due to synchrotron radiation as will be described in the next section. Radio emission from AGN allows to separate AGN in radio-loud and radio-quiet AGN, reflecting different characteristics of the AGN as outlined later on.

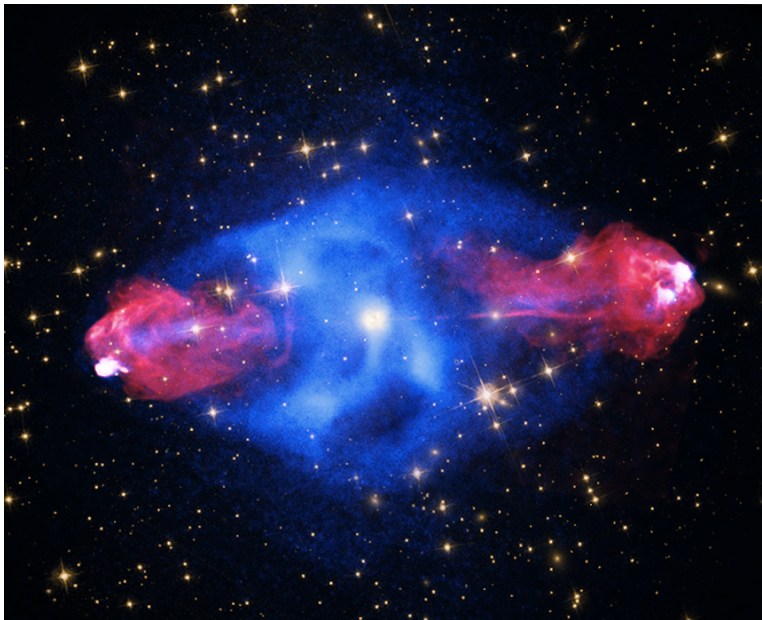


Figure 2.4: The radio galaxy Cygnus A showing the two back to back jets with a lobe structure. The blue color indicates X -ray emission as observed by the Chandra telescope, and the red one shows radio observations by VLA. Credits of the picture: NASA

2.2 The AGN Spectral Features

For reasons already mentioned in the introduction and which will be discussed in Chapter 4, the research developed in this thesis is mainly focused on radio and X -ray emission from AGN. Nevertheless, an overview of the

different radiative processes will be outlined to provide a general view on the AGN spectrum.

AGN can emit in different wavelength bands, giving a special signature about their spectra [22]. The measured fluxes at Earth cover frequencies in the whole electromagnetic spectrum. The different spectra can be classified in two groups according to the radiation engine. One of this is the thermal radiation which depends on the temperature of the source as Infrared, Optical and Ultra Violet emission, whereas non-thermal does not, as is the case for radio, X -ray and γ -ray radiation.

- Radio Emission: The radio spectrum is quite broad, covering a range between 3 kHz to 300 GHz ($\iff 1.2 \cdot 10^{-11}$ eV to $1.2 \cdot 10^{-3}$ eV) and is present in various environments, where AGN are not the exception. The main characteristic of such sources is the presence of lobes coming out of the center of the emitting objects as shown in fig. 2.4.

Dedicated telescopes have been built to detect radio emission from AGN, as is the case for the Very Large Array (VLA) [54] located in New Mexico, U.S., which covers the radio frequency range of 0.073-50 GHz in the full Northern sky and in the Southern hemisphere above a declination of -40° . On the other hand, for sources in the Southern hemisphere, the Molonglo Observatory Synthesis Telescope [55] in Australia is used, which operates at a single frequency of 0.843 GHz and covers the Southern sky below a declination of -30° . Both devices have been designed to have the same sensitivity. The radio survey constructed from VLA data is the NRAO VLA Sky Survey (NVSS) [56], whereas for the Molonglo observatory it is the Sydney University Molonglo Sky Survey SUMMS [57].

The responsible physical process for the radio emission in an AGN is Synchrotron radiation [22]. The emission in this electromagnetic band occurs mainly in the AGN-jet, due to electron acceleration in the presence of a magnetic field B . The maximum emitted power by an electron is given by [22]:

$$P = 2\sigma_T c \gamma^2 \beta 2U_B \sin^2 \alpha, \quad (2.2)$$

which is beamed in the direction of the motion of the electron, where α indicates the angle between the electron velocity and the magnetic field orientation, and σ_T is the Thompson cross section, γ the Lorentz factor, $\beta = v/c$ and U_B is the energy density of the magnetic field B .

It follows that the average power emitted by the electron is given by

$$\bar{P} = (4/3)\sigma_T c \gamma^2 \beta^2 U_B, \quad (2.3)$$

The additional factor 2/3 comes from the averaging of the sine square function over the full angular range.

- The Optical and Ultra Violet emissions cover a small range in the electromagnetic spectrum compared with the radio range. For the Optical part of the spectrum, this varies in the range of 400-789 THz (\iff 1.65-3.26 eV), and the Ultra Violet spectrum ranges from 750 THz-30 PHz (\iff 3.10-124 eV). Optical and Ultra Violet emission from AGN have been observed by optical telescopes at ground [58]. This Black Body emission is mainly attributed to processes taking place in a region of the AGN that surrounds the accretion disk, called Hot Corona (or Accretion Disk Corona). Furthermore, this region contains hot electrons that scatter photons from the accretion disk. These processes between photons and hot electron produce X-ray emission, are explained below.

Processes taking place in the central engine are not completely well understood. This is mainly because of the small region of the accretion flow, which is hard to resolve in detail when performing observations. Nevertheless, the heating process of the gas could be explained by accelerated gas particles interacting with the accretion disk, as described in the previous section.

The Black Hole mass is concentrated in a small region of the space-time defined by the Gravitational Radius or Schwarzschild Radius [42]:

$$R_G = \frac{2GM}{c^2}. \quad (2.4)$$

The accretion flow region is limited to a distance of order of $\sim 10R_G$.

If one considers a Black Hole mass of 10^8 solar masses, the resulting size for the central flow region becomes $\sim 10R_G = 5 \cdot 10^{-5}$ pc.

Furthermore, several AGN show a thermal emission at ~ 1000 Angstrom corresponding to 10^4 K (~ 100 nm $\iff \sim 10^{15}$ Hz $\iff 12$ eV). This emission is called *Big Blue Bump* and is attributed to direct emission from the accretion disc or radiation emitted from the central engine of the AGN [59]. This radiation from the central engine is reprocessed by optically thick clouds that absorb the incoming radiation and re emit it as a Black Body radiation [59, 60].

On the other hand, thermal radiation in the Infrared band also has been observed in AGN [61]. These observations mainly show emission in the Near and Mid Infrared with a peak in the range of $0.3\text{-}30 \cdot 10^3$ nm [22]. The responsible process for this radiation might be big blue bump photons re-interacting with surrounding dust [62]. By contrast, Far infrared emission is not representative for the process taking place in an AGN, instead, this is associated to emission from young stars in the host galaxy. The infrared emission is represented by the bump in the infrared part of the AGN spectra shown in fig. 2.6. Fig. 2.5 illustrates the position of the Infrared band in the electromagnetic spectrum, which shows that the Near infrared is close to the optical band, whereas the Far Infrared is closer to the microwaves.

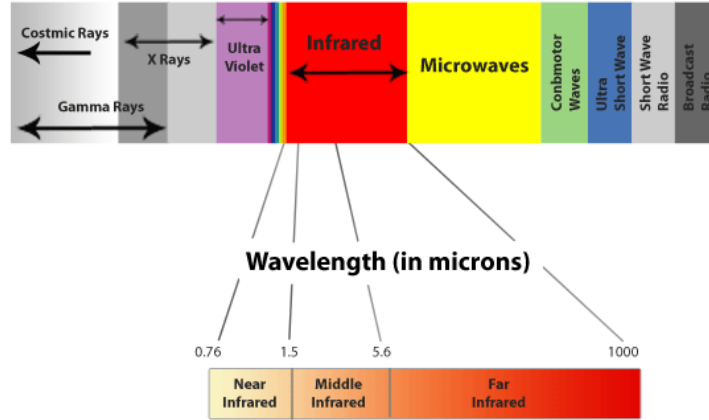


Figure 2.5: The Infrared band in the electromagnetic spectrum. The frequency (ν) ranges for some sub-electromagnetic domains are: Radio: 3 kHz-300 GHz, Optical: 400 THz-789 THz, Ultra Violet: 750 THz-30 PHz, X-ray: $3 \cdot 10^{16} - 3 \cdot 10^{19}$ Hz, γ -ray: $> 10^{19}$ Hz. The corresponding energy (E) range can be obtained by using the relation: $E = h\nu$, where $h \sim 4.1 \cdot 10^{-15} \text{eV} \cdot \text{s}$ is the Planck constant. Credits of the picture: [63].

- The X-ray frequency range is not so broad as the radio spectrum; it covers three orders of magnitude from $3 \cdot 10^{16}$ - $3 \cdot 10^{19}$ Hz (\iff 100 eV to 100 keV). These high-energies make that extraterrestrial X-rays can not be detected directly by telescopes at ground, since they can not pass through the atmosphere due to the small wavelength.

Telescopes dedicated to X-ray detection have been launched to orbit

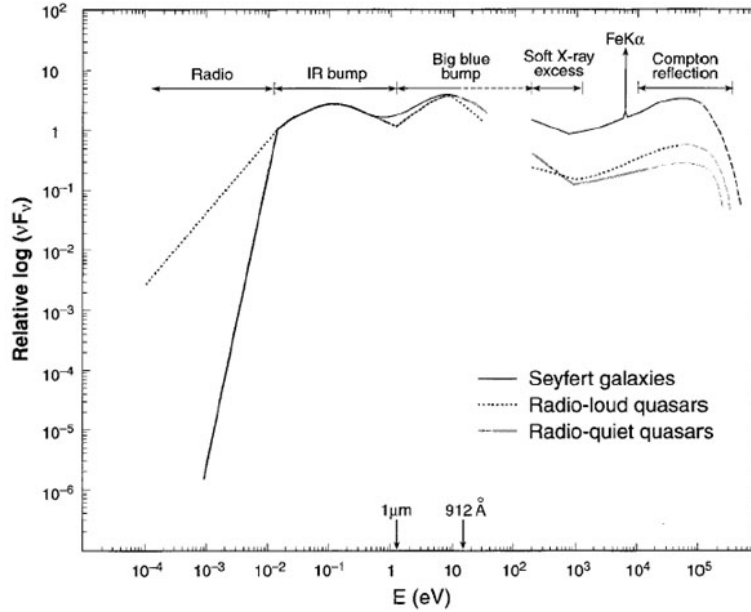


Figure 2.6: The AGN Spectra, where the Big Blue Bump can be observed. Credits: Koratkar and Blaes [64]

around the Earth to avoid the shielding caused by the atmosphere. Some of the main telescopes able to detect X -rays from astrophysical sources are: Chandra [65], Suzaku [66], ASCA [67] and XMM-Newton [68]. In addition to this, multiple wave length devices as Swift [69], ROSAT [70] and Fermi [33] are also sensitive to X -ray detection.

These X -ray spatial telescopes are operated by different spacial agencies. In the case of Chandra, Suzaku, Swift, and Fermi they are administrated by The National Space Administration (NASA) [71], where XMM-Newton is managed by The European Space Agency (ESA) [72]. Furthermore, joint efforts have been undertaken to launch other devices as ROSAT and ASCA, where ROSAT is administrated by NASA and The German Aerospace Center (DLR) [73], whereas ASCA by NASA and The Institute of Space and Astronautical Science (ISAS) [74].

To show some features of an X -ray telescope, the Rosat telescope is shown in fig. 2.7. This telescope was launched in 1990, and more than 60000 X -ray sources have been detected with this device [70]. Rosat covers the X -ray energy band 0.1-2 keV, with an extension to the

ultraviolet band of 0.04 keV - 0.2 keV. The position of the observed sources can be determined with a precision of 10 arcsec.

As will be shown lateron, this telescope provides the largest data set for selecting Obscured Flat Spectrum Radio AGN.

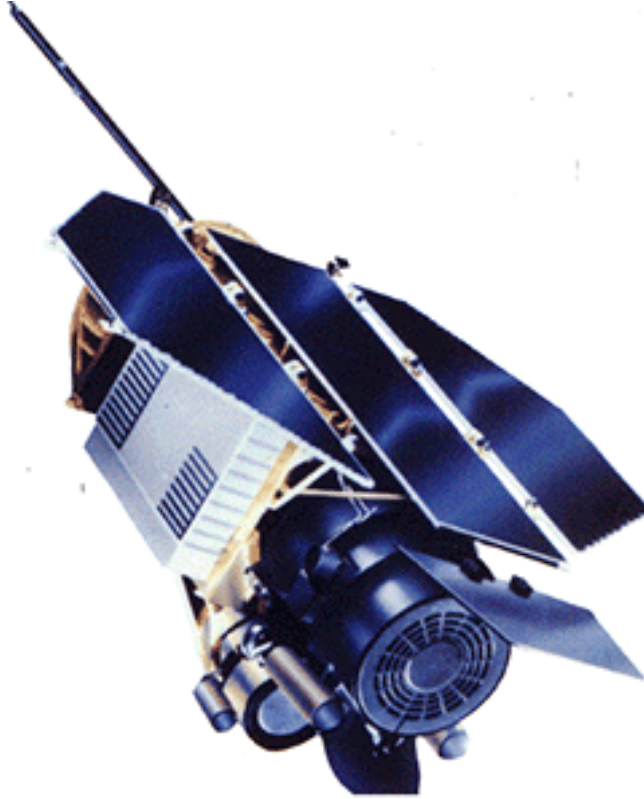


Figure 2.7: The Rosat telescope launched in 1990, dedicated to *X*-ray detection. Credits: [70]

The *X*-ray emission is attributed to the inverse-Compton and self-Compton scattering in the jet, direct emission from the accretion disc, or due to reflection from dusty components of the AGN [22]. The physical process that causes the inverse-Compton emission is due to a type of Compton scattering, in the sense that there is an electron interacting with a photon. Nevertheless, in this case the electron is not at rest, hence, the electron can transfer energy to the photon. The final

photon increases its energy in a Lorentz factor γ^2 ¹. By contrast, self-Compton Scattering consists of a set of electrons under the presence of a magnetic field, which later will emit radiation by Synchrotron process. Subsequently, this radiation process will fill the environment with photons, which can interact with their mother electrons [76].

The *X-ray* observations in the range of 1-100 keV are referred to as The *Primary Emission*, and is associated to inverse-Compton scattering between electrons in the jet with photons (optical-UV) that could be emitted from the accretion disk [77]. By contrast, *X-ray* emission below 1 keV is known as *The Soft X-ray Emission Component*, and is shown in fig. 2.8. This soft emission is suggested to be associated to processes taking place in the accretion disc corona [78].

Fig. 2.8 shows the power law of the primary emission (green line) with a high-energy cut-off at 100-300 keV. The curve between 1-100 keV can be modeled by a first order power law, where the Frequency Spectral Index (FSI) for this energy domain depends of the class of AGN. The FSI is normally referred as α , and is determined by the relation between the flux and the frequency given by $F_\nu = \nu^\alpha$. For instance, the values of the FSI for Quasars and Seyfert galaxies range between -0.8 and -1 [52]. Nevertheless, the consensus for the value of the frequency spectral index in the hard *X-ray* band corresponds to ~ -0.9 [64].

However, the primary emission can suffer multiple reflections before leaving the AGN proximity, as shown in fig. 2.9. That reflection can be due to Thomson scattering by ionized gas that is present in different parts of the AGN, for example, the dusty torus [77]. This reflection is exposed by the humpback distribution shown in fig. 2.8.

Another component of the *X-ray* spectra observed in fig. 2.8, is the sharp peak in between 2-10 keV that corresponds to the iron emission line at an energy of 6.4 keV [77]. The radiation is associated to processes taking place in the internal structure of the accretion disc.

- γ -ray emission from AGN is not very common, most of the AGN are radio-loud, but this is not the same at the highest frequencies of the electromagnetic spectrum, $E_\gamma \sim 100\text{keV}$ ($\iff \nu_\gamma \sim 10^{19}\text{Hz}$), where

¹The γ^2 factor is due to the photon energy in the observer frame and can be written as $\langle E \rangle = h\nu = \frac{P_{IC}}{\rho}$, where ρ is the scattered power per photon energy, given by $\rho = \frac{\sigma_T c U_{rad}}{h\nu_0}$, and the electron power is $P_{IC} = \frac{4}{3} \sigma_T c \beta^2 \gamma^2 U_{rad}$ [75]

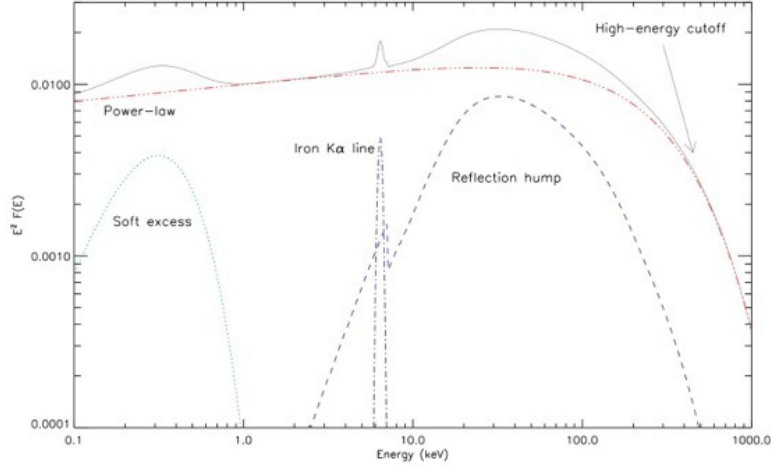


Figure 2.8: X-ray AGN spectrum in the range 0.1 to 1000 keV. The grey line shows the total spectrum. Credits: [79]

AGN show weak emission. Nevertheless, a small AGN sample (10%) does not follow this tendency [22]. These high-energy emitting AGN show emission up to TeV energies, which has been detected by dedicated devices as The Fermi Spacial Telescope [33, 81] and also by devices at ground, for example, The H.E.S.S gamma-ray observatory [82].

The mechanism to produce gamma-ray photons associated with astrophysical objects, such as AGN and GRBs, is not fully understood yet. This might be associated with either leptonic or hadronic processes in the environment of the astrophysical sources, which are referred to *Leptonic* and *Hadronic* Models respectively [83, 84, 85, 86]

The Leptonic Model refers to gamma-ray emission in processes where a lepton is involved, as for example, an electron. The responsible processes can be self-Compton scattering, or inverse-Compton scattering that were already explained above.

The Hadronic Model for explaining the γ -rays emission implies hadronic acceleration. This hadronic acceleration would allow the interaction of high-energy hadrons, such as protons, with ambient matter in the AGN environment, such as ambient photons ($p\gamma$). The final state of these interactions would produce neutral pions, and subsequently γ -rays via $\pi^0 \rightarrow \gamma_{ray} + \gamma_{ray}$. One possible mechanism to initiate the

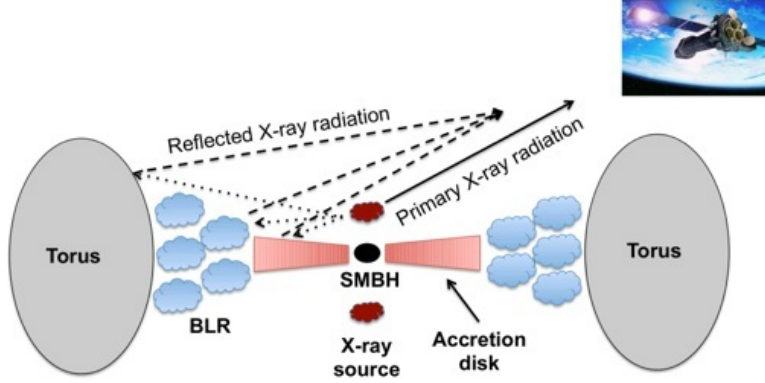
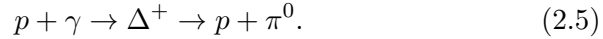


Figure 2.9: The different mechanisms that would give place to X -ray emission. Primary X -ray emission could be attributed to inverse Compton scattering in the AGN-jet. The secondary emission is associated to reflections of the primary emission. Credits: [80]

neutral pion production is through the Δ^+ resonance production [87]:



According to the branching ratios of the Δ^+ decay we also have the following decay mode $\Delta^+ \rightarrow n + \pi^+$ [87], which would be a possible mechanism to produce neutrinos in astrophysical environments via the decay of the charged pion [10, 14, 15, 16, 13, 17, 18, 19, 20, 21]. The efficiency of this engine to produce neutrinos is predicted to be rather low and with a maximum efficiency of about 20% [88]. This rather weak engine for the neutrino production in astrophysical environments is the reason why in this thesis a different kind of mechanism is investigated as a more efficient engine to produce neutrinos in AGN, as will be explained in the next Chapter 3.

The hadronic model for γ -ray emission would also lead to γ -ray production due to proton nucleus (pN) interactions in astrophysical environments. These interactions can produce many hadrons in the final state, containing neutral pions that will decay producing γ -ray photons [87]. This can occur if there are nuclei in the environment of an astrophysical object and the nuclear density is high enough. This mechanism for γ -ray production could be highly efficient due to the large number of neutral pions that can be produced. Nonetheless, the

observed γ -ray flux at Earth might be low since it will be attenuated by matter in the environment of the object or between the object and the observer. Furthermore, very energetic gamma rays may also suffer e^+e^- pair creation by interaction with the extra galactic background light (EBL).

Besides γ -ray production, these pN interactions would be highly efficient to produce neutrinos as well [34, 35, 36], which will be unlikely affected by the matter in the environment of astrophysical objects or in between the object and the observer. This mechanism will be explained in more detail in Chapter 3, and is the kind of neutrino engine that is aimed at in this thesis, which is investigated with data from the IceCube Neutrino Observatory.

2.3 Blazars

As mentioned before, the AGN zoo is quite large. AGN can be classified by color, spectroscopy, redshift, morphology and the orientation under which they are observed [22]. This last AGN characteristic defines a class of AGN, so-called, Blazars. A general definition for a Blazar is an AGN with its relativistic jet pointing towards us. Most of the AGN have a jet, which can point in different directions with respect to the line of sight of an observer. An overview of the AGN classification can be seen in fig. 2.2. Often they show lobe structures, which clearly indicates that the line of sight is not aligned to the jet.

Blazars can be classified in sub-classes, considering for example, their Frequency Spectral Index (FSI) in the radio band. The more common classes of Blazars are Flat Spectrum Radio Quasars (*FSRQ*) and *BL Lac*. Both classes of Blazars have similar features, for example, both present flat radio spectrum and high variability [89].

Fig. 2.10 shows a sub-sample of the The First LAT AGN Catalog (1LAC) [90], where it is seen that most of the BLLac objects (blue and green circles) have a weaker γ -ray emission between 0.1-10 GeV than FSRQs (red circles). This difference, observed mainly up to a luminosity $L_\nu \sim 10^{46} \text{erg s}^{-1}$, can be attributed to a radiatively inefficient to efficient accretion disc, so, the the accretion disc in FRSQ sources is more efficient than the one in BLLac [91]. This actually is one of the arguments that we used to split both populations when we proceed to select the Obscured Flat Spectrum Radio AGN population as will be explained in section 4.5.1.

A radiatively inefficient accretion disc could be explained by a lack of

material in that region, which will produce less photons via the processes taking place at the disc, as outlined in section 2.2. Those photons dominate the X -ray spectrum, nonetheless, they can reach the jet and produce γ -rays as well via inverse Compton processes. This lack of material can explain the absence of broad emission lines in BLLac objects [89].

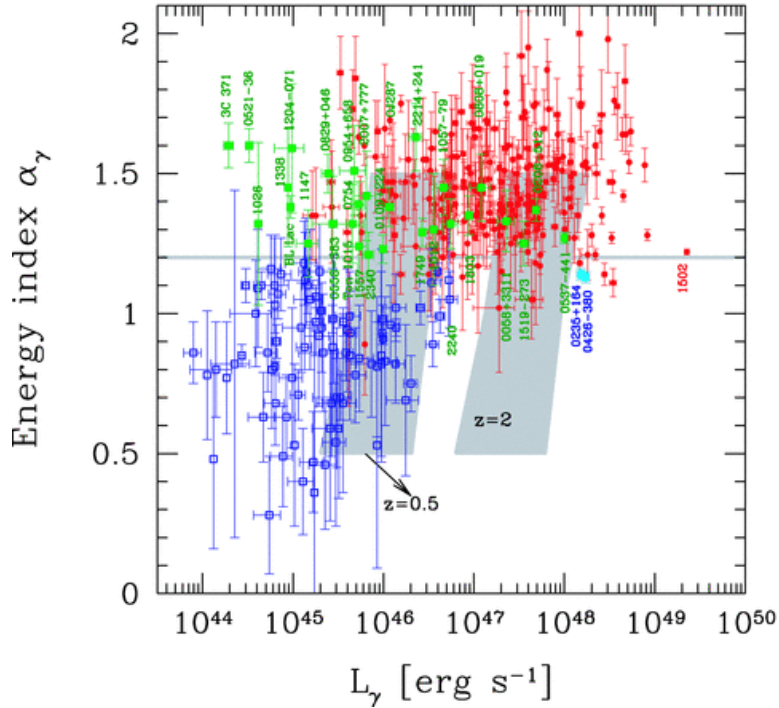


Figure 2.10: A sub-sample of The First Catalog of AGN detected by the Fermi Large Area Telescope (1LAC). The 1LAC full catalog was published in 2010 by the Fermi-LAT collaboration and is composed of 709 gamma-ray sources. This sub-sample shows a division between FSRQs (red circles) and BLLacs objects (blue and green circles) at $\sim 10^{46}$ erg s $^{-1}$. Furthermore, FSRQ objects dominate the region of the frequency spectral index above $\alpha = 1.2$. Credits: [91]

Whether or not the AGN jet is pointing towards us can be disentangled by analyzing the Synchrotron spectrum of the source. The shape of the Synchrotron radiation is characterized by the frequency ν vs flux F_ν as shown in fig. 2.11. In fig. 2.11, we show the Synchrotron spectrum from an electron distribution following an E^{-p} power-law. Before the cut-off frequency ν_1 , the emission is optically thick and follows a rising power law

[92]. The Synchrotron spectrum from an AGN, can now be understood as the emission originating from different regions, each one with a different density, which will result in a superposition of several spectra with different turnover frequencies. If the line of sight is along the jet, hence $\theta_{obs} \lesssim 1/\Gamma_{bulk}$, the turnover frequency varies inversely with the distance of these regions with respect to the central AGN core [93]. This gives rise to a characteristic value for the FSI α_R for the observed radio emission as indicated below. On the contrary, if the view is not aligned with the jet, the observed emission is dominated by the central core [93].

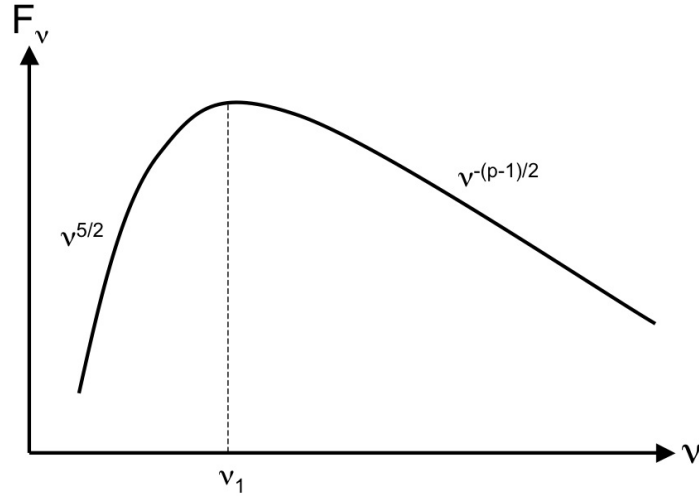


Figure 2.11: Synchrotron radiation spectrum. For long wavelengths $\nu < \nu_1$, for which the medium is optically thick, self-absorption effects dominate the spectrum, and can be described by a power law $\sim \nu^{5/2}$. Nevertheless, when the medium becomes optically thin, the spectrum is dominated by a power law $\sim \nu^{-(p-1)/2}$, which is related to the spectrum of the emitting particles $N(E) \propto E^{-p}$. Credits: [92].

The spectrum of a radio loud source can be represented by the following power law [22]:

$$F_\nu \propto \nu^{\alpha_R}, \quad (2.6)$$

where F_ν is the flux at a certain frequency ν , and α_R is the FSI.

The above equation can be re-written as:

$$\log F_\nu = \alpha_R \log \nu + \text{constant}. \quad (2.7)$$

- $\alpha_R > -0.5$: Represents a radio source with a flat spectrum, meaning that the radio jet is pointing towards the observer.
- $\alpha_R < -0.5$: Indicates a steep spectrum for a radio source, which implies that the direction of the radio jet is not along the line of sight.

As mentioned above, I referred to *radio jet* instead of just a jet, since the above power law is only applicable to the radio band. It is important to differentiate between a jet and a radio-jet in the AGN context. In general, an AGN-jet is referred to as a visible jet, which can emit over the whole electromagnetic spectrum.

However, it may happen that the observed radiation from an AGN is just the emission in the radio band of the electromagnetic spectrum, and that radiation at higher frequencies is absent. This last case will be discussed in the next section and is an important point in this thesis. Consequently, the sources that are aimed for to be analyzed as possible neutrino emitters, are not requested to have a visible jet, but they have to have a radio-jet.

2.4 AGN Obscuration

The research developed in this thesis aims to the search of high-energy neutrinos emitted from Obscured Flat Spectrum Radio AGN. Therefore, we will review the scenario of AGN obscuration, which has been introduced by several authors [22, 94, 48, 95, 96, 97, 98].

The AGN obscuration can be attributed to any kind of gas and/or dust in the AGN vicinity, blocking the line of sight to the observer, and absorbing the radiation via the photoelectric effect and compton scattering, as outlined below. This obscuration can be due to a misaligned disc [94], a tilted torus [96, 97] or simply due to a sort of clouds of dust as shown in fig. 2.1.

Unobscured and obscured AGN do not show a large difference in the radio emission [95]. This is due to the large wavelength that leaves radio emission relatively unaffected by the presence of material in our line of sight. This is one of the main features that is requested for the analyzed sources in Chapter 4. Hence, no attenuation on the radio emission is expected from Obscured Flat Spectrum Radio AGN.

The X -ray signature emitted by an AGN plays an important role in the search for Obscured Flat Spectrum Radio AGN. The surrounding dust in an obscured AGN is not able to stop the radio emission, due to its long wavelength. Nevertheless, this is not the case for short wavelengths as X -ray photons, which can interact with a column of matter in the AGN en-

environment, being absorbed due to the Photoelectric Effect [48]. The X -ray emission could be strongly absorbed at frequencies below $\sim 2.4 \cdot 10^{17}$ Hz (~ 3 keV) due to the excitation of various atoms, or losing energy by interacting with the medium via Compton scattering in an ionized medium, which takes place in a frequency range of $\sim 1.7 \cdot 10^{18} - 7.3 \cdot 10^{18}$ Hz [95]. The X -ray interaction with matter will be addressed in Chapter 4, where by considering the attenuation of the X -ray intensity, an estimation of the amount of dust in the environment of an AGN can be made.

An example of a possible Obscured Flat Spectrum Radio AGN is the Seyfert 2 galaxy NGC 1068, shown in fig. 2.12. The figure shows the center of the galaxy, with a dusty donut surrounding a source of light. Nevertheless, if we try to find a signature for the emission from the center of the galaxy, it will be convoluted due to the fact that the light of the whole galaxy is very strong. This strong emission by the host galaxy will overlap with the spectrum of the light emitted from the center, which will be reflected in the surrounding dust [48]. This overlapping is due to the fact that the host galaxy can emit in the same wavelength due to star formation regions.

The reflected radiation originates from the central engine of the NGC 1068 galaxy, emitted in the optical and X -ray bands. This initial radiation can be reprocessed in the dusty torus and finally is reradiated as infrared (mainly in the near and mid infrared) [99]. This emission actually helped to determine the presence of a dusty torus in NGC 1068, by comparing a region with purely stellar emission with respect to a region of emission from multiple components of the galaxy, including the AGN. Thus, it was possible to observe broad line emission from the region with emission from multiple components of the galaxy [100].

Nevertheless, NGC 1068 does not fall into the category of AGN that are aimed at in this thesis, because its radio jet does not point toward Earth, which is clear since this is classified as a Seyfert 2 galaxy according to [101].

2.4.1 Ionized material in obscured AGN

One question that is important in the context of obscured AGN studies is whether the obscuring material is ionized. The level of obscuration will actually play an important role in the estimation of the amount of protons that interact with the obscuring material in Obscured Flat Spectrum Radio AGN as will be explained in section 4.5.2. The ionization depends on several factors, such as the energy of the incident photons, the thickness of the obscuring material and the distance from the central engine (AGN core) to the position of the column of matter. All those parameters can be expressed

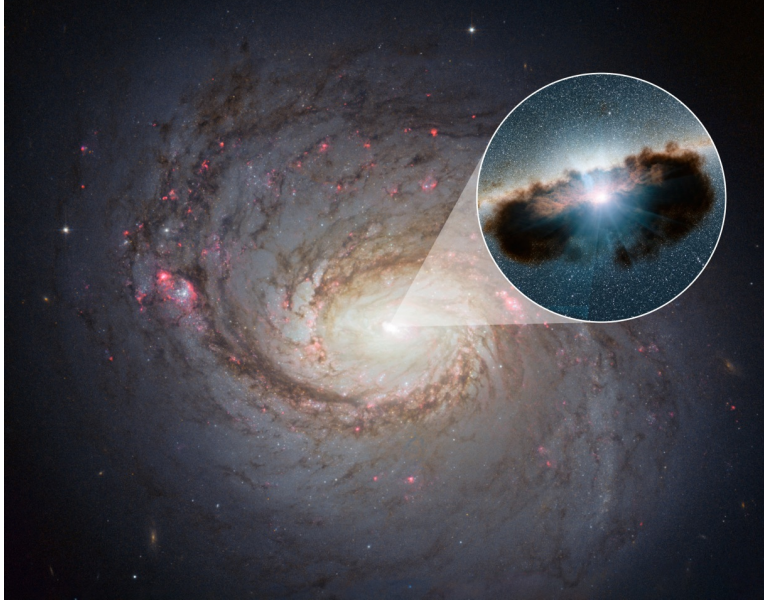


Figure 2.12: The Seyfert 2 galaxy NGC 1068. A clear dust torus surrounding the central engine is observed. Credits [102].

in terms of the Ionization Parameter [22]:

$$U_X = \int_{E_1}^{E_2} \frac{L_E/E}{4\pi r^2 c n_N} dE, \quad (2.8)$$

where E_1 and E_2 are the energy limits of the ionizing continuum for the obscuring material constituent, N , with nucleon number density n_N and c the speed of light. The parameter L_E indicates the monochromatic luminosity per unit of energy. If $U_X > 0.1$, the medium in the AGN environment is highly ionized, and above of 10^{-3} the medium is partially ionized [22]. The distance from the central engine to the column of matter that surrounds the AGN core, such that this matter has an ionized level U_X is given by:

$$r = \left(\frac{\log_e(E_2/E_1)L_E}{4\pi c n_N U_X^2} \right)^{1/2}. \quad (2.9)$$

The energy limits can be set according to the more abundant elements that we observe in the universe, which mainly go from Hydrogen to Iron, so $E_1 \approx 0.1$ keV, $E_2 \approx 10$ keV. Regarding the nucleon number density n_N can

be written in terms of thickness of the obscuring material d and the total column density X_{tot} (in g/cm^2):

$$n_N = \frac{X_{tot} N_A}{M d}, \quad (2.10)$$

with N_A the Avogadro's number and M the molar mass.

The column density X_{tot} can be obtained by considering the fraction of “light” that is absorbed at a determined frequency, and consequently at a specific interaction depth λ ². It follows that X_{tot} can be determined from the following expression [46, 87]:

$$I = I^0 \exp\left(\frac{-X_{tot}}{\lambda}\right). \quad (2.11)$$

The above relation gives the intensity I for a beam of particles with interaction depth λ , after passing through a column depth of matter X_{tot} , and with an initial intensity of the beam I^0 .

In our Obscured Flat Spectrum Radio AGN selection treated in Chapter 4, we restrict ourselves to study the AGN emission at a frequency of $3.02 \cdot 10^{17}$ [Hz], which corresponds to X -ray photons with an energy of 1.24 keV. This restriction is based on the data availability in the NASA/IPAC Extragalactic Dataset (NED) [52].

As illustrated in fig. 2.13, the interaction of a photon with an energy of 1.24 keV is dominated by photo-electric absorption, whereas attenuation by Compton scattering effect is small. To determine n_N as given in eq. 2.10 via eq. 2.11, we obtain from XCOM [104] the interaction depth λ for the two processes, photo-electric absorption and Compton scattering, considering a medium as in our atmosphere for reasons that will be explained in section 4.5.2. Those values correspond to $\lambda_X^{Compton} = 65 \text{ g cm}^{-2}$, and $\lambda_X^{PE} = 5 \cdot 10^{-4} \text{ g cm}^{-2}$ respectively.

From the above values for the interaction depth and eq. 2.11, we determine the column depth of obscuring material X_{tot} such that 90% of the X -rays is attenuated due to Compton scattering, which lead us to a value of $X_{tot,Comp} = 150 \text{ g cm}^{-2}$ for a fully ionized material $U_X > 0.1$. We proceed in the same way as for Compton scattering when the X -ray beam is attenuated by photo-electric absorption, which results in a value of $X_{tot,PE} = 1.2 \cdot 10^{-3} \text{ g cm}^{-2}$.

²The Interaction Depth can be written as $\lambda = \int \rho dr$, where ρ is the matter density and dr is the path that a particle passes through. Hence, the more matter of density ρ is in the path along which the particle travels, the more energy the particle loses.

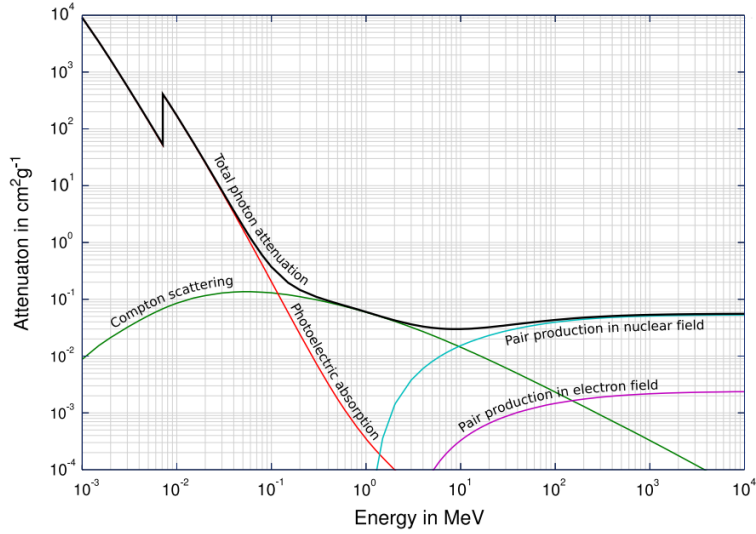


Figure 2.13: Mass attenuation coefficient of Iron. At 1.24 keV, the process that dominates the photon interaction is photo-electric absorption. Credits [103].

Combining the above values with eq. 2.10 and 2.9, we obtain the distance at which the obscuring material with thickness d would be positioned such that a beam of photons is attenuated by Compton scattering or photo-electric absorption, which is displayed in fig. 2.14.

Fig. 2.14 shows that an obscuring material close to the central engine of the AGN core would be fully ionized, and attenuate an intensity of photons at 1.24 keV mainly by Compton scattering, whereas at Mpc scale the attenuation would be lead by photo-electric absorption. As explained in this Chapter, the position of the dusty structures from the central Black Hole in an AGN typically ranges between 0.1 to 10 pc [48], and hence in the following we consider a fully ionized obscuring material.

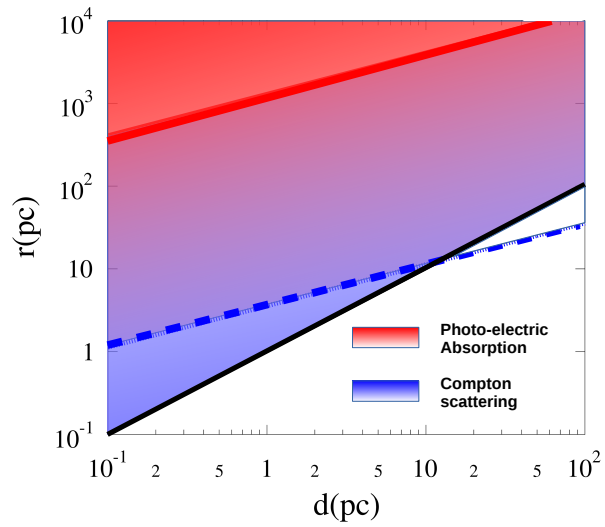


Figure 2.14: The distance r in parsec from the AGN core at which the obscuring material would be placed in order to be ionized for photons of 1.24 keV, this as a function of the thickness of the material d in parsec. The dashed blue line shows 90% X -ray attenuation by Compton scattering in case the medium is fully ionized. The same situation indicates the solid red line when the beam is attenuated by photo-electric absorption.

Chapter 3

Neutrino Production in AGN

This thesis is focused on neutrino observations from a specific class of AGN, Obscured Flat Spectrum AGN. Hence, I present a brief overview of the relevant neutrino properties. This will be followed by a description of the main processes involving neutrino production in an AGN.

3.1 Neutrino Overview

Neutrinos are fundamental particles in the Standard Model of particle physics, and their interactions are governed by the Weak Interaction. They are classified according to their flavors, where three neutrino flavors belong to the Standard Model: the electron neutrino (ν_e), the muon neutrino (ν_μ) and the tau neutrino (ν_τ). These three neutrinos are often called Active Neutrinos, since they interact with matter in nature, opposite to Sterile Neutrinos that have been proposed but not detected yet [105]. Furthermore, active neutrinos are almost massless, and they have no electric charge [106]. Along this thesis, I will refer to active neutrinos only.

The weak interaction is mediated by W and Z Vector Bosons, where an interaction headed by the W is called Charge Current (CC) interaction, while the Z boson directs the Neutral Current interaction (NC). Fundamental forces in nature have been assigned a coupling constant, and the weak interaction coupling constant is proportional to the Fermi constant G_F^2 . It follows that the probability¹ that a neutrino interacts with other particles is very low with respect to other kind of interactions in the Standard Model.

¹The interaction probability of a particle after moving a distance x in a medium with number density n_N is given by $P_{int}(x) = 1 - \exp(-x/n_N\sigma)$ [46]

E_ν [GeV]	σ_{CC} [cm ²]	σ_{NC} [cm ²]
10 ¹	0.777×10^{-37}	0.242×10^{-37}
10 ²	0.697×10^{-36}	0.217×10^{-36}
10 ³	0.625×10^{-35}	0.199×10^{-35}
10 ⁴	0.454×10^{-34}	0.155×10^{-34}
10 ⁵	0.196×10^{-33}	0.745×10^{-34}
10 ⁶	0.611×10^{-33}	0.252×10^{-33}
10 ⁷	0.176×10^{-32}	0.748×10^{-33}
10 ⁸	0.478×10^{-32}	0.207×10^{-32}
10 ⁹	0.123×10^{-31}	0.540×10^{-32}
10 ¹⁰	0.301×10^{-31}	0.134×10^{-31}
10 ¹¹	0.706×10^{-31}	0.316×10^{-31}
10 ¹²	0.159×10^{-30}	0.715×10^{-31}

Table 3.1: Charged and Neutral Current cross sections for neutrino-nucleon scattering above 10 GeV, which is dominated by Deep Inelastic Scattering [106, 107]. It is important to notice how the cross section grows with the energy of the neutrino, hence, high energy neutrinos have a relatively large probability to interact with a medium. The values are obtained from [107], which also are displayed in fig. 3.1.

To illustrate how small the neutrino interaction probability is, let us suppose a neutrino and a γ -ray passing through a medium with a nucleon number density $n_N = N/V$ in units of m⁻³. The average distance of a particle passing through this medium before interacting:

$$\lambda = 1/n_N\sigma, \quad (3.1)$$

which is known as the interaction depth or mean free path [87].

Let us now consider that the neutrino and the γ -ray have a similar energy of a few GeV and interact with a nucleon at rest, N . The neutrino-nucleon cross section is taken at 10 GeV from [107], which is shown in table 3.1. For the γ -ray-nucleon total cross section, this is taken from [108], and at few GeV has a value of $\sim 120\mu\text{b} \iff 120 \cdot 10^{-24} \cdot 10^{-6}\text{cm}^2$. To compare the probability that a neutrino interacts with matter, we shown the ratio between the neutrino and γ -ray mean free path in a medium n_N :

$$\frac{\lambda_\nu}{\lambda_{\gamma\text{-ray}}} \sim 10^{-9} \quad (3.2)$$

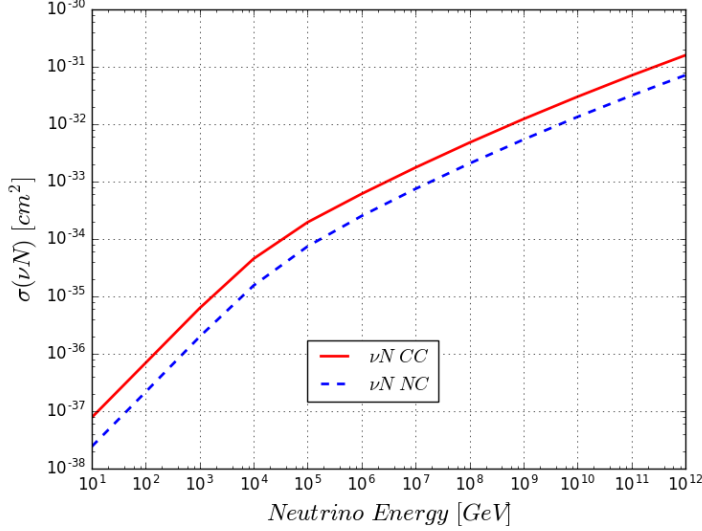


Figure 3.1: Charged and Neutral Current cross sections for neutrino-nucleon scattering above 10 GeV, as displayed in table 3.1.

The above ratio clearly shows how small the probability of interaction of the neutrinos is with respect to other fundamental interactions in the Standard Model. Moreover, this is the reason why extraterrestrial neutrinos can pass through the terrestrial atmosphere to be detected at ground, whereas the γ -rays are stopped.

High-energy neutrino interactions ($> 10\text{GeV}$) are mainly dominated by deep inelastic scattering [107]. Several neutrino processes can take place considering the energy range of the interaction, neutrino flavor (l) and the target. The main processes are listed below [106]:

$$\nu_l + l' \xrightarrow{Z} \nu_l + l', \quad (3.3)$$

$$\nu_l + l \xrightarrow{W^{\pm Z}} \nu_l + l, \quad (3.4)$$

$$\nu_l + N \xrightarrow{Z} \nu_l + N, \quad (3.5)$$

$$\nu_l + n \xrightarrow{W} p + l, \quad (3.6)$$

$$\nu_l + N \xrightarrow{Z} \nu_l + X, \quad (3.7)$$

$$\nu_l + N \xrightarrow{W} l + X. \quad (3.8)$$

In the above processes, l indicates a lepton, N is a target nucleon, n is a neutron, p a proton and X denotes a shower of hadrons that are created after a hard scattering.

Neutrinos can be created at Earth by natural processes, such as the beta decay taking place in some unstable atoms, so-called geo-neutrinos, and also by human induced mechanisms as made in power reactors and particle accelerators [109]. Neutrinos are also produced by the interaction of cosmic-rays with the terrestrial atmosphere, so called atmospheric neutrinos, which cover a broad energy range between MeV and TeV [110, 111]. Furthermore, these weakly interacting particles can be produced in the Sun, so-called, solar neutrinos, where the responsible process of this low energy neutrino (eV-MeV) production is the proton-proton fusion chain [106].

In order to investigate neutrino oscillation properties, several experiments around the world have been designed, for example, MINOS and NOvA at Fermilab in the U.S. [109], and as T2K in Japan [112]. Neutrino oscillations refer to the change of neutrino flavor state, which depends of certain conditions. Some of these conditions are the neutrino energy and the distance at which the neutrino is generated until this is detected [106].

So far, several neutrino properties remain unknown, such as the neutrino mass hierarchy, and whether neutrinos are Majorana or Dirac particles. To investigate these unknown properties, more experiments are being built, such as JUNO in Japan [113], and others are planned to be built in the near future, for example, the Deep Underground Neutrino Experiment (DUNE) at the U.S. [109] and the Agua Negra Deep Underground Site (ANDES) in Los Andes Mountain in between Argentina and Chile [114].

Extraterrestrial Neutrinos

The neutrino sources mentioned above are not all the sources that produce these particles. Extraterrestrial neutrinos have been observed from a Supernova burst, as the ones detected by the Super-Kamiokande collaboration [115]. These neutrinos have an energy of a few MeV, and they are thought to originate from Inverse Beta Decay ($e + p \rightarrow \nu_e + n$) that can take place in a Supernova explosion [106]. Due to the energy range these are considered low energy neutrinos, and consequently those are not the ones

process	$\sigma_{total}[10^{-46}cm^2] \approx$
$\nu_e + e$	$93 * 2mE_\nu/MeV^2$
$\bar{\nu}_e + e$	$39 * 2mE_\nu/MeV^2$
$\nu_{\tau,\mu} + e$	$15 * 2mE_\nu/MeV^2$
$\bar{\nu}_{\tau,\mu} + e$	$13 * 2mE_\nu/MeV^2$

Table 3.2: Cross section values for MeV neutrinos as given in [106].

target in this thesis. As shown in table 3.2, low energy neutrinos have a very small cross section. Thus, this quality makes it hard to detect them, implying that the volumes and densities of dedicated neutrino detectors have to be large enough to achieve a large probability of interaction. As mentioned before, one dedicated device to “hunt” Supernova neutrinos is The Super-Kamiokande detector. This device has a volume of ultra-pure water of ~ 50000 tons, such that when a neutrino (ν_e) reaches the detector it can produce an electron, which produces Cerenkov radiation which makes possible to identify the incoming neutrino [106].

Furthermore, extraterrestrial high-energy (TeV-PeV) neutrinos have been detected at Earth by the IceCube Collaboration [27, 28]. Due to the neutrino characteristics, astrophysical neutrinos are not affected by magnetic fields and unlikely absorbed by matter when they travel toward Earth. As such, these features make neutrinos very interesting particles to study the brightest objects in the universe, as AGN and GRBs.

The energy range of extraterrestrial neutrinos observed at the IceCube neutrino observatory is much higher than the energy of the observed Supernova neutrinos. As indicated in table 3.1, the neutrino cross section grows with energy, therefore, the probability of interaction of an astrophysical high-energy neutrino that propagates in a medium is larger than low-energy neutrinos emitted from Supernova explosions [115]. However, despite the high energy that astrophysical neutrinos can reach, it is hard to detect them, which implies that large detectors have been built to observe these high-energy cosmic neutrinos. Examples of those devices are the ANTARES [25] and IceCube detectors [26]. Part of this thesis work is based on neutrino observations in the IceCube detector, hence, a description of the IceCube detector is given in Chapter 5.

Astrophysical neutrinos would play an important role as messengers in astrophysical phenomena. The engine to produce neutrinos in an astrophysical source is believed to be due to the interaction of accelerated hadrons

(Cosmic Rays) with ambient matter [10, 14, 15, 16, 13, 17, 18, 19, 20, 21, 35].

Those hadrons would be ejected of the environment from astrophysical objects, such as GRBs and AGN. Subsequently, they can interact with ambient matter in the AGN environment and produce neutrinos. If an astrophysical neutrino is detected at Earth, its direction could be tracked back enabling to identify its progenitor in the sky. Since neutrinos and cosmic-rays are expected to be correlated, an identification of a neutrino source will provide indications about cosmic-ray emission from that source, hence, hadronic acceleration at that source. Consequently, neutrinos are good messengers to study the kind of processes that take place in astrophysical environments as in AGN or GRBs.

GRBs and AGN are thought to be the main candidates for emitting cosmic rays, and therefore also sources of astrophysical neutrinos [10, 14, 15, 16, 13, 17, 18, 19, 20, 21]. Nevertheless, IceCube searches for neutrino emission from GRB, indicate an absence of neutrinos associated with this kind of sources [29, 30]. The GRB exclusion (for prompt neutrino emission) as main candidate to be neutrino sources, strengthens the idea of AGN as neutrino emitters. Therefore, in the next section, the different processes to create neutrinos in AGN are reviewed. We focus mainly on the neutrino engine in Obscured Flat Spectrum radio AGN.

3.2 Neutrino Production in AGN

One of the mechanisms for producing neutrinos in AGN is supposed to be via Δ^+ production [18, 21]. The Δ^+ production is lead by the following process:

$$p + \gamma \rightarrow \Delta^+. \quad (3.9)$$

However, the Δ^+ production depends on the energy of the target photons (E_γ) as well as the accelerated proton. Therefore, the minimum proton energy to produce a Δ^+ can be obtained through the invariance of the total four momentum squared:

$$2(E_p E_\gamma - \vec{p}_p \cdot \vec{p}_\gamma) = m_{\Delta^+}^2 - m_p^2 \quad (3.10)$$

Let us suppose now a target photon of 100 eV that could originate from a process described in the previous Chapter (for example, the soft X -ray emission AGN component), which is hit by an accelerated proton that is moving perpendicular to the photon ($\vec{p}_p \cdot \vec{p}_\gamma = 0$). Hence, the minimum

proton energy to produce a Δ^+ in the above equation is $E_p \sim 3.2 \cdot 10^6$ GeV. This kind of accelerated proton will be observed as a cosmic-ray if this reaches the Earth.

As shown in fig. 3.2, a proton energy of $E_p \sim 3.2 \cdot 10^6$ GeV fits well in the energy range of the high-energy cosmic-rays observed by cosmic-ray observatories at Earth [8]. Consequently, if in an AGN a proton can be accelerated up to an energy of order of 10^6 GeV and interacts with an ambient photon of an energy of ~ 100 eV, this can produce a Δ^+ resonance.

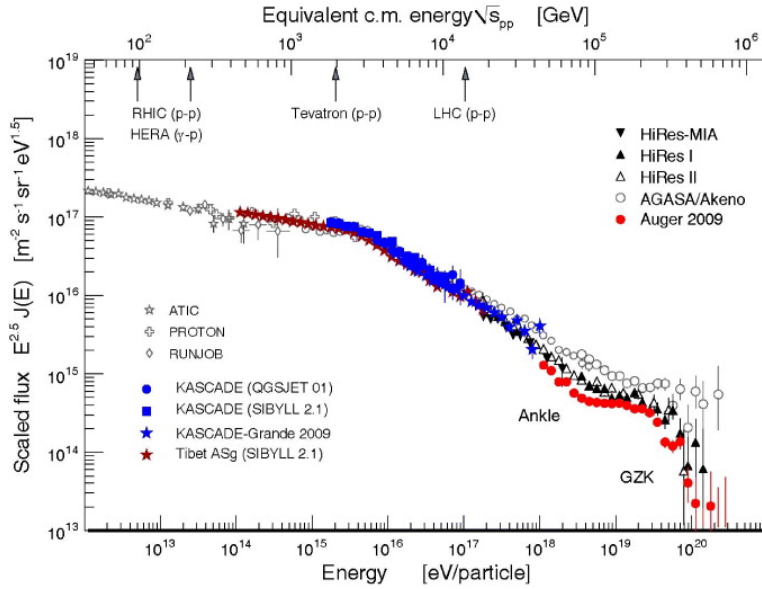


Figure 3.2: The cosmic-ray spectrum from different cosmic-ray observatories as given in [8].

After the Δ^+ production, the neutrino production follows from the counterpart of the process that produces γ -rays described in eq. 2.5, hence:

$$\Delta^+ \rightarrow n + \pi^+, \quad (3.11)$$

followed by

$$\pi^+ \rightarrow \nu_\mu + \mu^+ \rightarrow \nu_\mu + e^+ + \nu_e + \bar{\nu}_\mu. \quad (3.12)$$

Therefore, three neutrinos would be expected from the $p + \gamma \rightarrow \Delta^+$ process, $(\nu_\mu, \nu_e, \bar{\nu}_\mu)$. I will refer to the process in eq. 3.11 as the *Standard Neutrino Production in an AGN*. Furthermore, if the neutron (n) in eq. 3.11 is able to escape from the AGN environment and decay, this will produce one

more (anti) neutrino through $n \rightarrow p + e + \bar{\nu}_e$. Notice that the $\Delta^+ \rightarrow n + \pi^+$ state that arises from the $p + \gamma$ interaction, is not the only channel for neutrino production, multiple meson production can also take place. Such channels could produce a larger amount of neutrinos than the ones yield by $\Delta^+ \rightarrow n + \pi^+$ [116].

However, the standard neutrino production process in an AGN is expected to have a low efficiency, not more than 20% of the accelerated protons will produce neutrinos [88]. There are many factors that can influence that rather low efficiency, such as the density of the target photons, and the strength of the magnetic field in the AGN environment. The intensity of the magnetic field affects charged particles as π^+ and μ^+ produced in eq. 3.11. Due to the fact that these particles are very energetic, they live longer and lose energy by synchrotron radiation before decaying. Moreover, they could be deflected by the same magnetic field and the produced neutrinos will never reach Earth since they carry the 3-momentum of their progenitors.

The standard neutrino production in AGN has a γ -ray counterpart as given in eq. 2.5. Consequently, it might be possible to establish a correlation between γ -ray observations and neutrino expectation. Considering those arguments, it can be argued that “The brighter an AGN is, the higher its expected neutrino flux is”. Nevertheless, as outlined below, these kind of objects have been analyzed by the IceCube Collaboration and no strong evidence for neutrino emission has been found. As a result, upper limits on the neutrino flux from these AGN have been set [31, 32].

The main feature of the AGN analyzed by IceCube is that they are very bright, with emission at high-energies in the electromagnetic spectrum [31]. In this search, no substantial evidence for high-energy neutrino emission was obtained. By contrast, the analysis described in [32], is based on a Blazar population emitting in a broad range of the electromagnetic spectrum. By analyzing either flaring states or by looking for coincidences with γ -ray as detected by Fermi LAT. Nevertheless, no evidence for high-energy neutrino emission was found.

Due to the fact that there are no strong indications of neutrino emission from bright blazars, motivated one of the goals in this thesis “Search for a specific class of AGN that could emit a high neutrino flux”.

In the next sub section, we will illustrate how to estimate the amount of energy of the proton that is carried out by a neutrino following the $p\gamma$ interaction. We illustrate this process because it represents a consensus between several authors for explaining the neutrino production from AGN [21, 18].

3.2.1 Neutrino energy in $p\gamma$ interaction.

The consensus to explain the proton acceleration in astrophysical environments aims to Fermi acceleration [117]. The proton energy spectrum at first order diffuse shock acceleration can be written like [21]:

$$\frac{dN_p}{dE} \propto E^{-2} \quad (3.13)$$

In the scenario of the $p\gamma \rightarrow \Delta^+ \rightarrow n + \pi^+$ process, the power law for the neutrino flux can be obtained through the above equation and considering that the energy of the produced neutrino is directly related of the proton energy.

From the invariance of the total 4-momentum square we have

$$m_{\Delta^+}^2 = (p_{\pi^+} + p_n)^2, \quad (3.14)$$

where the m_{Δ^+} is the mass of the resonance, and p_{π^+} and p_n is the 4-momentum of the charged pion and neutron respectively. The equation above yields,

$$E_{\pi^+}E_n - \vec{p}_{\pi^+} \cdot \vec{p}_n = \frac{m_{\Delta^+}^2 - m_{\pi^+}^2 - m_n^2}{2}. \quad (3.15)$$

In the center of mass of the resonance the 3-momentum of the pion and the neutrino are back to back, but with the same magnitude of the 3-momentum, therefore, the dot product above produces,

$$E_{\pi^+}E_n + |\vec{p}_{\pi^+}| \cdot |\vec{p}_n| = \frac{m_{\Delta^+}^2 - m_{\pi^+}^2 - m_n^2}{2}. \quad (3.16)$$

The total energy of a relativistic particle can be written in terms of its 3-momentum p and mass m through: $E^2 = p^2 + m^2$. Hence, the eq. 3.16 becomes,

$$E_{\pi^+} = \frac{m_{\Delta^+}^2 + m_{\pi^+}^2 - m_n^2}{2m_{\Delta^+}}. \quad (3.17)$$

From the equation above, we obtain that 20% of the energy of the Δ^+ resonance is carried by the charged pion. Boosting everything to the observers frame immediately shows that this fraction also relates to the original proton energy.

A similar procedure as the one outlined above can be performed to obtain the percentage of the neutrino energy obtained from the decay of the charged

pion, $\pi^+ \rightarrow \nu_\mu + \mu^+$. The neutrino energy can be written in terms of the mass of the pion m_{π^+} and the mass of the muon m_{μ^+} ,

$$E_{\nu_\mu} = \frac{m_{\pi^+}^2 - m_{\mu^+}^2}{2m_{\pi^+}}. \quad (3.18)$$

The equation above shows that 20% of the energy of the charged pion is given to the neutrino. Consequently, according to this illustration, the energy of the neutrino would correspond to about 4% of the energy of the accelerated proton in the stage of $p\gamma$ interaction.

It follows that for each $p\gamma$ interaction, the produced primary neutrino in $\pi^+ \rightarrow \nu_\mu + \mu^+$ would follow the proton power law, hence,

$$\frac{dN_\nu}{dE} \propto E^{-2}, \quad (3.19)$$

A precise treatment of neutrino emission from AGN in the scenario of $p\gamma$, would also need to take into account the secondary neutrinos produced by the muon decay, and neutrinos produced from the neutron decay initiated by Δ^+ . However, the latest neutrinos would have a lower energy than the former. Furthermore, effects like energy losses of charged particles, as muons and charged pions, as a consequence of the presence of magnetic fields should be considered. These effects are out of the scope of this illustration.

3.2.2 Neutrino Production in Obscured AGN

A good example of an obscured AGN is the Seyfert 2 galaxy NGC 1068 shown in fig. 2.12. Thus, objects with this kind of feature and combined with a radio jet pointing toward us would yield a high neutrino flux to be observed at Earth, if hadronic acceleration takes place in the AGN environment. If an accelerated hadron “hits” a dusty structure, as the one observed in NGC 1068, that would be followed by meson production via the processes eq. 3.7 and eq. 3.8, which subsequently will produce neutrinos.

The physical principle in the above approach is that the proton-nucleon cross section is much larger than the $p\gamma$ cross section, which can be seen in fig. 3.3. The difference between both cross sections can be explained due to the fact that the proton-nucleon cross section is directed by the strong interaction, whereas $p\gamma$ by the electromagnetic interaction [45]. I have referred to proton-nucleon interaction, nonetheless, this can be a proton-nucleus interaction as well. Since nucleons will be involved in the interaction anyhow, I will continue referring to *proton-nucleon interaction* (pN). Furthermore, an

accelerated proton is a generic way of referring to any accelerated hadron, therefore, an accelerated hadron can be any kind of particle in this class.

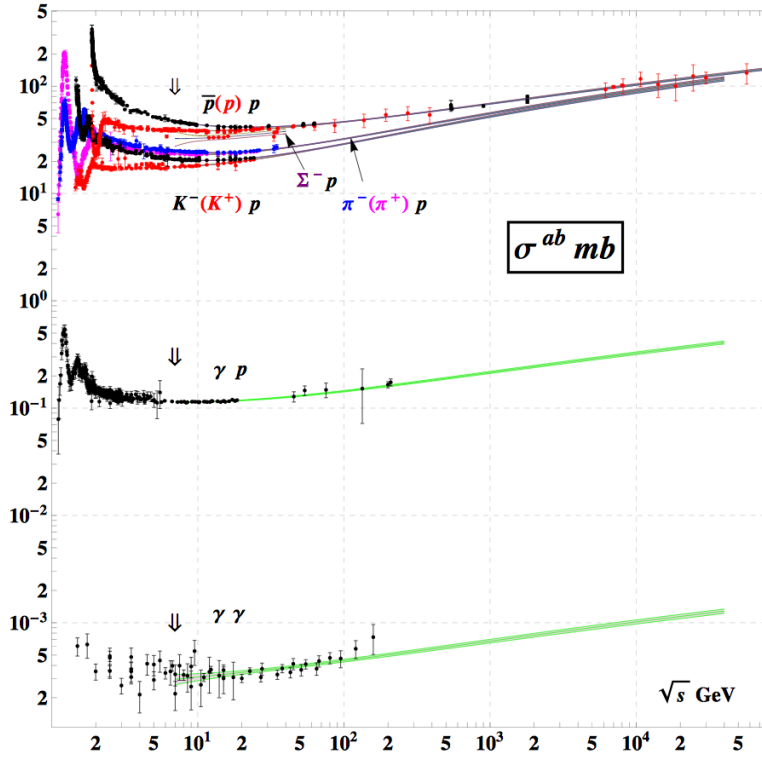


Figure 3.3: Total cross section σ^{ab} in mb for different processes as a function of center of mass energy \sqrt{s} in GeV. The $p + N$ cross section is more than 2 orders of magnitude larger than the $p + \gamma$ one [87].

An important consideration to identify an AGN as an obscured object, is the column matter density that is obscuring the AGN. If this column of matter is not sufficiently dense, the probability that pN interactions occur would not be large enough. Therefore, the engine to produce neutrinos would not be sufficiently efficient. The effect of the matter density in combination with the cross section can be exposed by analyzing the survival probability of finding a particle after “traveling” a distance x in a medium of density ρ [46]:

$$P(x) = \exp(-x/\lambda), \quad (3.20)$$

where λ is the mean free path, as in eq. 3.1. If the mean free path λ is small,

the survival probability of finding a particle after a distance x in a medium of density ρ is small. Hence, a particle beam dump would take place if the cross section and medium density fulfill proper conditions. This criterion can be applied to a proton that interacts with a column of dust in an AGN environment. In Chapter 4, as a part of the procedure to select obscured flat spectrum radio AGN, a method to calculate the column matter density in an AGN is outlined, and has been part of the results accomplished in [34, 35].

To illustrate how large the neutrino flux via pN interaction is, compared with the one produced by the $p\gamma$ channel, we use the PYTHIA 6.4 event generator [118]. We produce 10^4 protons considering the features that are expected if hadronic acceleration takes place in AGN, in which the typical proton spectrum follows the power law $d\Phi/dE \sim E^{-2}$ [15, 21, 8].

In this simulation, the generated protons have an energy between 10^6 and 10^{11} GeV. This is chosen based upon the energy range of the cosmic-rays observed at Earth, as indicated in fig. 3.2, where the cosmic-rays are expected to have an extragalactic origination [8]. If they are emitted by AGN, cosmic-rays observed at Earth would unlikely be emitted by Obscured Flat Spectrum Radio AGN, because of the beam dump effect explained above, but, they might originate from AGN that are not obscured instead, where they have been accelerated by similar mechanisms. It follows that in this scenario the cosmic rays and neutrinos are not directly linked.

The expected decoupling between cosmic-rays and astrophysical neutrinos has been investigated in [36]. Based on multimessenger arguments, the authors claim a tension between the γ -rays observed by the Fermi Space Telescope and the extraterrestrial high-energy neutrinos detected by the IceCube Collaboration. It follows that the authors suggest that the sources that produce the extraterrestrial high-energy neutrinos are hidden in the γ -ray emission in the domain of GeV-TeV. Hence, these kind of sources are so-called “Hidden Cosmic-Ray Accelerators as an Origin of TeV-PeV Cosmic Neutrinos”

As outlined before, 20% of the accelerated protons is expected to interact with ambient photons in the more optimistic scenario [88]. Therefore, in our PYTHIA, 2000 protons will be forced to interact with mono-energetic photons of 1 keV that can originate in an AGN. The 80% of protons that are left, will interact with nucleons (protons) that play the role of the obscuring material in the AGN environment. Consequently, a proton beam dump is forced to occur for the remaining 80% of the originally generated proton flux.

In fig. 3.4 we show the meson production for $p\gamma$ and pN interactions,

that subsequently produce neutrinos both directly and indirectly. I refer to a direct way in the case that mesons decay and immediately create neutrinos, like for instance charged kaons and pions. In contrast, an indirect way refers to mesons that do not decay immediately in neutrinos, like for instance rho mesons, that first produce pions ($\rho^0 \rightarrow \pi^+ + \pi^-$). In fig. 3.4 we see that the largest contribution comes from pN interactions (solid lines). It is important to notice that the charged pion production (π^+ in blue and π^- in red) gives the largest contribution to the set of generated mesons. Nevertheless, other mesons make a non-negligible contribution to the neutrino production.

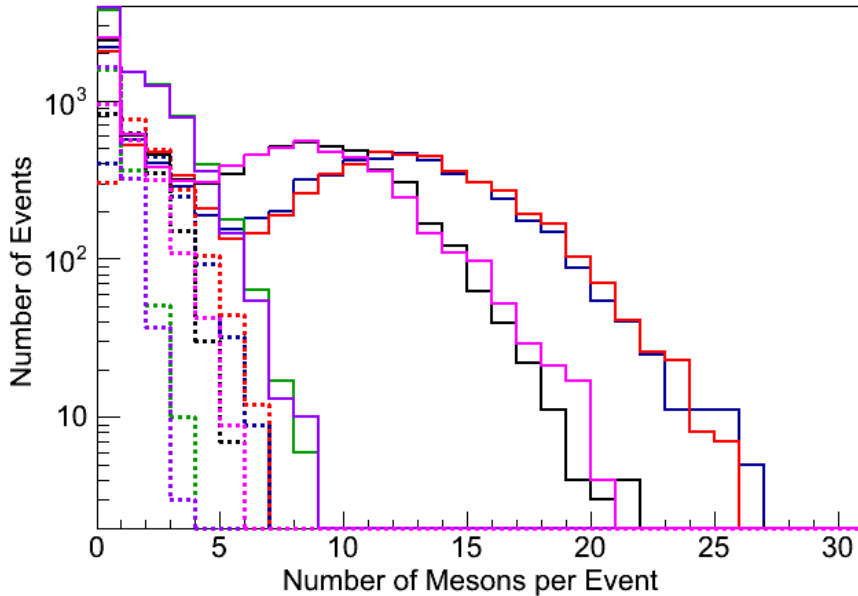


Figure 3.4: Set of mesons generated with PYTHIA 6.4 due to pN (solid lines) and $p\gamma$ (dashed lines) interactions. The simulated sample is obtained by 10000 proton events with an energy spectrum of E^{-2} between 10^6 and 10^{11} GeV. For $p\gamma$ interactions the target photon has an energy of 1keV. Regarding the pN interactions, the target N is at rest. The different colors represent different mesons, π^+ -blue, π^- -red, K^+ -green, K^- -purple, ρ^+ -black and ρ^0 -magenta.

After their production the mesons decay rapidly due to their short life time and will produce neutrinos following their branching ratios [87]. This neutrino population is fully dominated by muon and electron (anti-) neutrino-

process	ν_μ	$\bar{\nu}_\mu$	ν_e	$\bar{\nu}_e$	ν_τ	$\bar{\nu}_\tau$
pN	524065	524065	270309	265552	13	13
$p\gamma$	24887	24887	13038	12386	0	0

Table 3.3: Number of produced neutrinos via pN and $p\gamma$ interactions in our PYTHIA 6.4 simulation. The energy range of the protons corresponds to 10^6 and 10^{11} GeV, and the energy of the ambient photon is 1 keV.

nos. The tau neutrino production is extremely unlikely, because of the large mass of the tau lepton. As indicated in table 3.2.2, indeed a very small number of tau neutrinos is produced in this PYTHIA simulation.

The neutrino spectrum arising from the decay of the produced particles, it is presented in fig. 3.5 for both channels, pN (blue) and $p\gamma$ (red). Clearly, the pN interaction produces a larger neutrino flux than the $p\gamma$ channel. Note that in the neutrino flux produced in $p\gamma$ interactions, low energy neutrinos could be produced by low energy protons, which would interact “elastically” with photons and would produce lighter hadrons. These hadrons could be ρ mesons, which decay in pions and those pions subsequently produce neutrinos. Consequently, these latter neutrinos would not have the same kinematic as illustrated in section 3.2.1 for the primary neutrinos, hence they would produce a different power law than E^{-2} as illustrated in fig. 3.5.

It should be noted that in this simulation, secondary nucleons are not allowed to decay (in case of neutrons), and neither to interact with other particles that constitute the obscuring material. The forbidden decay model is set since we expect that those secondary nucleons would interact with the mater that blocks our line of sight before they decay.

The interaction of the secondary nucleons (or secondary hadrons) is not included in this current simulation. Nevertheless, this is expected to lead to additional meson production via nucleon-nucleon interaction, and as such, this process would contribute even more to the neutrino flux via the decay additional mesons. Secondary nucleons may be produced by the $p\gamma$ interaction, or could be part of the hadrons produced in a pN scattering. Consequently, the presented result in fig. 3.5, is a conservative illustration of the increase of the neutrino production in an obscured AGN, if we ignore energy loss effects. The energy loss effects affect charged particles, as protons and pions, when they move along the magnetic field in the AGN environment. As explained above, for very high-energy particles the energy loss is enhanced due to the fact that these particles live longer and they emit longer Synchrotron radiation. However, detailed calculations to model

a more realistic case go beyond of the scope of this thesis, but will be subject of follow up studies addressing the phenomenological aspects of the involved physical processes.

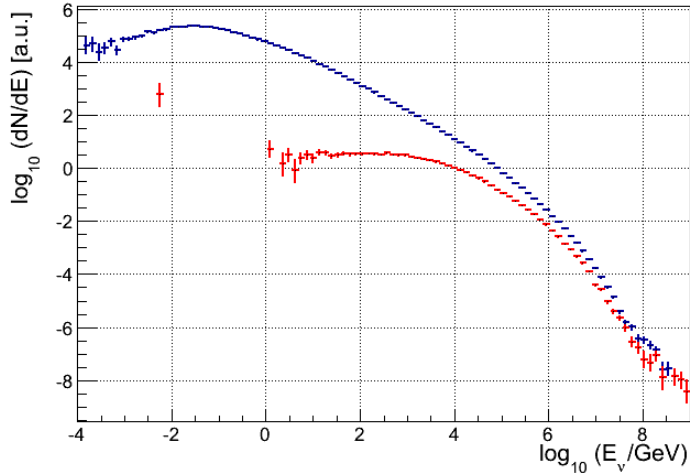


Figure 3.5: The Neutrino spectrum obtained from pN (blue) and $p\gamma$ (red) interactions generated with PYTHIA 6.4. The simulated sample is obtained from 10000 protons with an energy spectrum of E^{-2} between 10^6 and 10^{11} GeV. For $p\gamma$ interactions the target photon has an energy of 1 keV. Regarding the pN interactions, the target N is at rest.

Considering that the PYTHIA simulation used to study the neutrino production in Obscured AGN is not a full simulation of all the possible processes, we may say that the high-energy neutrino spectrum (dN_ν/dE) observed in fig. 3.5 follows more or less the predictions, as shown in [36]. Therefore, the IceCube event selection performed to investigate the Obscured Flat Spectrum Radio AGN, will consider the power law $dN_\nu/dE \propto E^{-2}$ for the possible neutrino emission from that AGN population.

As exposed above, a large low energy neutrino production is expected in Obscured Flat Spectrum Radio AGN, nonetheless, they might not reach Earth. This fact is due to the “boosted angle”, as given by $\theta_{boost} \sim 1/\gamma$, which determines the opening angle of the relativistic jet of particles. For the most energetic particles, the produced neutrinos are expected to be closely aligned with the jet direction, whereas at lower energies the distribution may get more diffuse. As will be outlined lateron, our analysis needs a good directional reconstruction for the muons induced by the generated

astrophysical neutrinos that are expected to interact close or in the IceCube detector. A good angular resolution, requires neutrino energies of at least several TeV (see fig. 7.7), which implies primary proton energies beyond 100 TeV. Consequently, the neutrinos of interest for our studies are expected to be closely aligned with the relativistic jet.

Chapter 4

Obscured Flat Spectrum Radio AGN.

So far, the investigations of AGN as possible astrophysical sources of high-energy neutrinos have shown no significant evidence to indicate that these objects indeed emit those weakly interacting particles [31, 32, 119]. It is important to stress that the AGN zoo is quite extended, hence, one can not state that the whole AGN class does not emit high-energy neutrinos, since the investigations mentioned above have been performed only on sub classes of AGN. Therefore, in this thesis it was decided to investigate a specific class of AGN, so-called, Obscured Flat Spectrum Radio AGN [34, 35], which have not been considered in previous searches.

The idea to investigate Obscured Flat Spectrum Radio AGN was born from the concept of AGN obscuration [94, 48], outlined in Chapter 2. They are characterized by a radio-jet pointing toward us in combination with low flux observed at the highest frequencies of the electromagnetic spectra, in the X -ray and γ -ray bands. Within this model, the highest frequencies are expected to be attenuated due to the surrounding dust or gas blocking the jet. However, the low flux at highest frequencies might also be due to the effect of intergalactic material which is in the line of sight between the source and the observer. Consequently, under those arguments, it was decided to limit the AGN sample to sources at low redshifts.

The selection of Obscured Flat Spectrum Radio AGN was started at the Vrije Universiteit Brussel. During that research, the selection was only based on a single catalog, with the title: “Radio galaxies of the local universe All-sky catalog, luminosity functions, and clustering” [120], hence, we will refer to this as *The Radio catalog*. The selection in that study, was different

from the one in the current thesis, where the differences will be pointed out in this Chapter. Nevertheless, at that time, three objects were found as potential Obscured Flat Spectrum Radio AGN (at that time called Dust Obscured Blazars) candidates, which also pass all the selection criteria in this thesis.

In this Chapter, a description of the two investigated catalogs is given, followed by the selection criterion to constrain the AGN sample to low redshift sources. Afterwards, the selection by Frequency Spectral Index is explained, which indicates whether the jet is pointing towards us or not, and hence, the selected objects will be called sources with a *flat radio spectrum*. Finally, on the limited volume sample with flat radio spectrum a last selection is applied, which consists of on requesting low X -ray fluxes detected at Earth, indicating the presence of dust or gas in the AGN environment, as described in Chapter 2. Consequently after this last filter, the final population of Obscured Flat Spectrum Radio AGN is obtained for further investigation with IceCube data.

All the data in this analysis is obtained from the NASA/IPAC Extragalactic DataSet (NED) ¹ [52].

4.1 The Catalogs

The list of astronomical catalogs of AGN is quite large, nevertheless, this analysis is limited to two catalogs, selected according to the final goals of my studies.

The first considered catalog is the Radio Catalog mentioned above [120], which contains 575 radio-emitting galaxies, covering 88% of the sky. The 575 sources in this catalog have been split into four different categories, mainly by considering morphology and near-infrared emission with respect to the host galaxy. Those categories are: Starforming Galaxies (52), Jets and Lobes (407), Point Sources (97), and Unknown Morphology (19). The sources in the Radio Catalog were selected to contain a volume-limited sample of radio sources which might be possible emitters the UHECRs detected at Earth. This makes the Radio Catalog [120] a very interesting survey to consider in the current analysis.

For covering the radio-band of the electromagnetic spectrum, the study developed in the Radio Catalog consists of data from two radio telescopes, the Very Large Area telescope (VLA) [54] and the Molonglo Observatory

¹The retrieval of data from NED was handled by a Python script using the Beautiful-Soup library, which allows to read html format

Synthesis Telescope (MOST) [55], which already were described in Chapter 2.2.

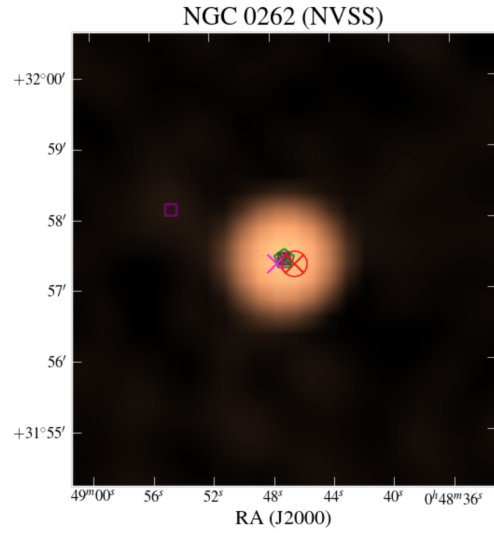
It is important to notice that both telescopes, VLA and MOST, have similar sensitivity and resolution, such that there is no bias when analyzing sources in different hemispheres. Furthermore, most of the radio-data in NED [52], from where the data for this part of this thesis is obtained, comes from NVSS and SUMSS as mentioned before.

The selected sources from the Radio Catalog used in this thesis, are extracted from the Starforming Galaxies and radio Point Source categories. These categories show a circular radio morphology, which indicates that in case a jet structure is present it has to be aligned with our line of sight. Concerning Jets and Lobes, and Unknown Morphology categories, they were not included in this analysis due to their non-circular morphology. Nevertheless, as a consistency check sources in those categories were checked by the algorithm, explained in section 4.3, which indicates whether or not the object has a jet pointing towards us, and indeed none of the latter objects were passing this selection. An example of a galaxy with a circular morphology is shown in fig.4.1(a), whereas in fig.4.1(b) we observe one of the objects in the jets and lobes category, which has a clear non-circular morphology indicating a non-Blazar type AGN.

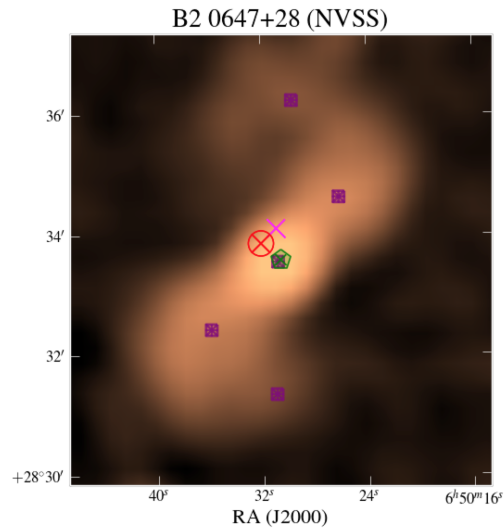
In the study described in [121], only the Point Source category was analyzed due to their clear circular morphology. Nevertheless, afterwards it was decided to include the Starforming category since they might contain an AGN with a jet pointing towards us as well. This idea is strengthened by the fact that objects in this category might result from the merging process of two galaxies, with a Black Hole in its center with a possible radio-jet pointing towards us. Nonetheless, they would present a region of starforming and clouds of dust/gas due to the merging process. Several sources in this Starforming category passed the selection explained in section 4.3, which strengthens the idea of analyzing this category.

The sources in this Radio Catalog are located inside the close universe defined by a redshift $z < 0.1$. The redshift is an important parameter which is used in the first selection to define the Obscured Flat Spectrum Radio AGN population, which will be explained in the next section. Furthermore, a preselection on the radio flux larger than 231 mJy at 1.4GHz or 289 mJy at 843 MHz was made.

The second catalog considered is: *The Second Catalog of Active Galactic Nuclei Detected by the Fermi Large Area Telescope (2LAC)* [81], hence, this will be referred to as 2LAC. This catalog is built by 1017 γ -ray sources, and was published after two years of operation of the Fermi telescope [33]. The



(a) AGN Radio source with a circular morphology. This falls within the Point Source category.



(b) Radio source with a non circular morphology, from the Jets and Lobes category. The lobe structure indicates that the jet is not pointing towards us. These objects are not included in our analysis.

Figure 4.1: Two objects from different categories in the catalog of radio-emitting galaxies [120].

clean sample² (886 objects) of this 2LAC catalog is divided in the following categories: BL Lacertae objects (BL Lac) (395), Flat-Spectrum Radio Quasars (FSRQ) (310), Unidentified Sources (157), Other AGN (22) and Starburst Galaxies (2). The 2LAC sample includes objects with a galactic latitude $|b| > 10^\circ$, and within a redshift of $z = 3.1$.

The clean sample of 2LAC means that the objects are associated with a single source and are not affected by analysis issues. The 2LAC catalog includes a large fraction BLLac and FSRQs in its whole sample, which was the reason of including this catalog in the analysis presented in this thesis, since these objects are well known for having a jet pointing toward Earth. The 2LAC sample classification is shown in fig. 4.2.

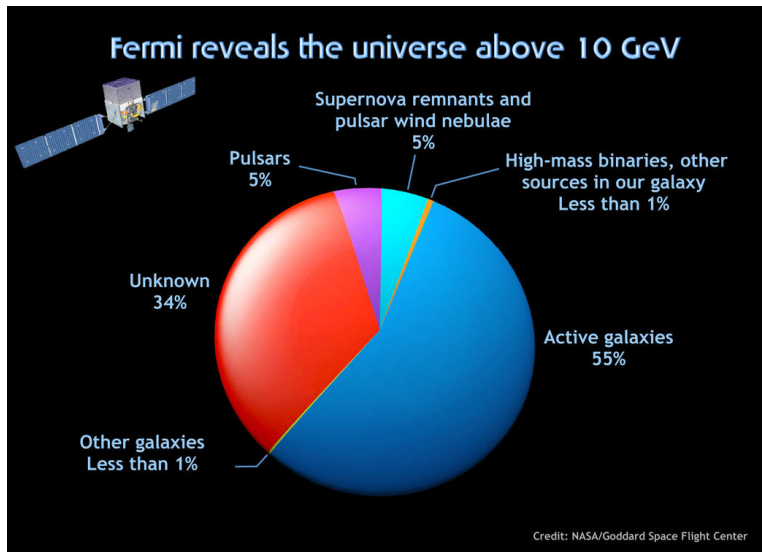


Figure 4.2: 2LAC sample classification. Credit: <http://fermi.gsfc.nasa.gov>

It can happen that the same object falls in both catalogs, in this situation, the data of duplicated objects are merged. Moreover, different astronomical catalogs could have the same object but with different names. Therefore, an algorithm was used to check for objects with the same right ascension and declination in both catalogs. Subsequently, objects matching those two entries in both catalogs were merged as well. After these cross

²A clean sample is defined by objects that do not present analysis issues, have a large test statistic (less compatible with background), and the signal can be associated to a single AGN.

checks a list of 735 unique sources is obtained.

4.2 A Limited Volume Sample of Galaxies

As outlined before, Obscured Flat Spectrum Radio AGN are expected to have a low flux at highest frequencies in the electromagnetic spectrum. Nevertheless, the low flux at those frequency bands, could also be due to the extinction by the intergalactic medium, which might attenuate the intensity measured at Earth. This attenuation clearly is proportional to the distance to the source, and is hard to correct for because of the lack of precise knowledge about the composition and density of the intergalactic medium.

In order to avoid the flux extinction due to intergalactic medium effects, a source selection based on redshift is made. This selection starts from the fact that, if one looks further away, one should observe more and more sources in the sky. Nevertheless, the flux of the sources drops as the distance to the source squared (R^2). At some point, the observed flux falls below threshold and one starts to loose sources. This statement can be exposed by considering the number of sources N in a sphere of radius R , and with a source density number n :

$$N = \frac{4n}{3}\pi R^3. \quad (4.1)$$

The flux F_ν at certain frequency ν is given by:

$$F_\nu = \frac{L_\nu}{4\pi R^2}, \quad (4.2)$$

where L_ν is the luminosity at a certain frequency ν . Combining the above two equations one obtains that the number of sources N with a flux $F > F_0$ scales like $\sim F^{-3/2}$ for a generic luminosity L_ν . It should be noted here that this argument also holds for sources with a generic energy spectrum like for instance the E^{-2} spectrum that was mentioned before.

The number of sources as function of a certain threshold flux F_0 is what is checked as a first selection to obtain a non biased Obscured Flat Spectrum Radio AGN population. Fig. 4.3 shows the distribution of the number of sources with a flux F larger than F_0 . Indeed, one can see that between $-5.5 \leq \log(F_0/Jy) \leq -4.6$ this distribution scales like $\sim F^{-3/2}$, which infers that for values below $\log(F/Jy) < -5.5$ one starts to loose sources. This cumulative plot was constructed using the 2LAC sample only. This is because the sample in the Radio Catalog is already located within the close universe.

The redshift distribution of the sources falling in the range $-5.5 \leq \log(F_0/Jy) \leq -4.6$ is shown in fig. 4.4. In order to be conservative with the value of the redshift threshold, the statistical median of this distribution is used. After selecting objects with a redshift smaller than the statistical median equal to $z = 0.17$, the initial sample of 735 sources is reduced to 209 objects within a limited volume.

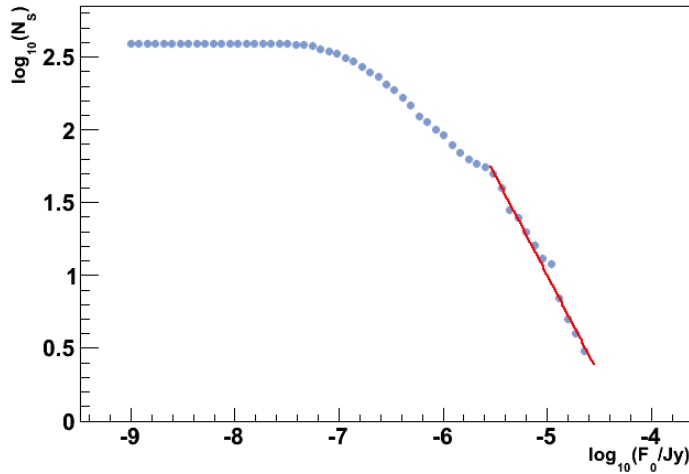


Figure 4.3: Cumulative plot for the (logarithm 10) number of sources N_s with a flux F larger than F_0

4.3 Flat Spectrum Radio AGN

As already mentioned, a Blazar is an AGN with a jet pointing towards the observer, which can be regarded as its main feature. As explained in Chapter 3, this is an important feature in our high-energy neutrino searches. A jet in our line of sight indicates that in case of hadronic acceleration, the neutrino emission will be boosted towards Earth. Consequently, in our study of AGN as possible neutrino emitters, we request the existence of a jet pointing towards us.

In the jet of a Blazar, emissions at multiple wavelengths have been observed [81]. Nevertheless, the high-energy emission in Obscured Flat Spectrum Radio AGN is expected to be suppressed by the effect of dusty structures around the AGN, which actually cause the AGN obscuration. There-

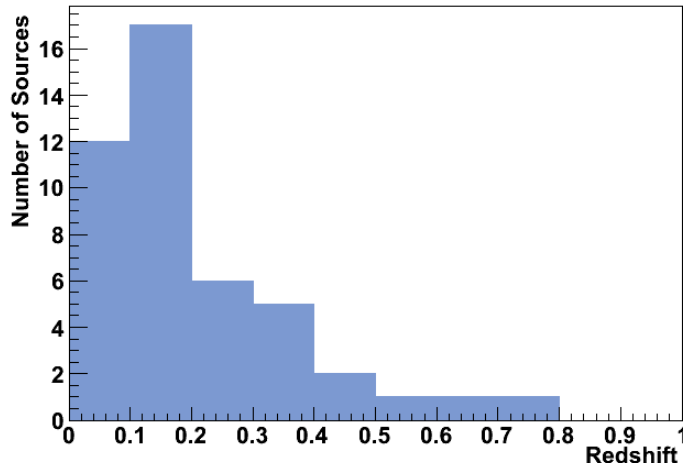


Figure 4.4: Redshift distribution for the objects falling in the range $-5.5 \leq \log(F_0/Jy) \leq -4.6$

fore, Obscured Flat Spectrum Radio AGN are not requested to have a visible jet, instead, they are just requested to have a radio-jet.

As explained in section 2.3, a Blazar has a Flat Radio Spectrum, therefore, the kind of objects that are targeted in this part of the analysis are Active Galactic Nuclei with a flat spectrum in radio, which will be referred as Flat Spectrum Radio AGN.

One can determine whether the possible radio-jet of an AGN points towards the Earth, by considering the Frequency Spectral Index (FSI) α_R of the power law $F_\nu \propto \nu^{\alpha_R}$ as described in section 2.3.

Starting from the limited volume sample obtained in the above section, which corresponds to 209 objects, one can fit the NED data for each individual object according to the power law given in eq. 2.7. The algorithm which handles this fit procedure³ works for any range of frequencies in the electromagnetic spectrum. The considered range in this analysis, lies within the radio band 0.843-5.0 GHz.

Since in a linear fit, at least three data points are needed, sources with a lack of data are excluded. The limited volume sample consisting of 209 sources is reduced to 176 objects with sufficient data to perform the spectral fit.

³The slope of the fit is calculated by using the Minuit library (TLinearFitter) from ROOT [122]

Sometimes, several flux measurements are associated to a single frequency in NED, therefore, a special treatment was applied for performing a data fit as described above. In the previous analysis presented in [121], if several data fluxes were associated to a single frequency, the flux average was calculated for such frequency. Moreover, at that time, it was noted that several flux measurements in NED had no available data for their uncertainty, in that case, 20% of the flux value was associated as an uncertainty.

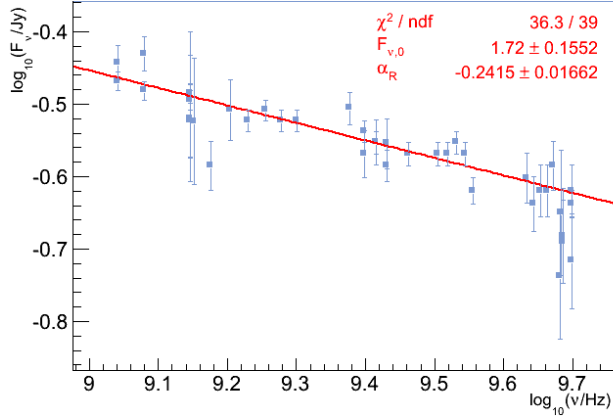
However, the above fitting procedure was changed due to the fact that some entries at a certain frequency could be very scattered, for which the average would not be a precise representation of the set of points. Since data measurements might be taken in a broad time range, those scattered points could be the result of flaring periods of the object. In order to improve the spectral fitting procedure for scattered entries, the standard deviation was calculated for the whole set of flux measurements at a certain frequency. Consequently, the flux uncertainty associated to a single frequency had two contributions to the uncertainty, the one given by the measurement errors and another one given by this standard deviation.

The above algorithm worked well, but it was noticed that it had a serious drawback. To illustrate this situation, consider a source with a set of flux measurements at a certain frequency, containing a very high single point with an extremely small error bar, and the remaining points with significantly lower values and larger error bars. What might happen is that the high point with small error bar would pull up the fit, subsequently, producing a not representative slope (FSI) of the set of points of a given source. To cope with this, a new iterative algorithm to calculate the FSI was developed.

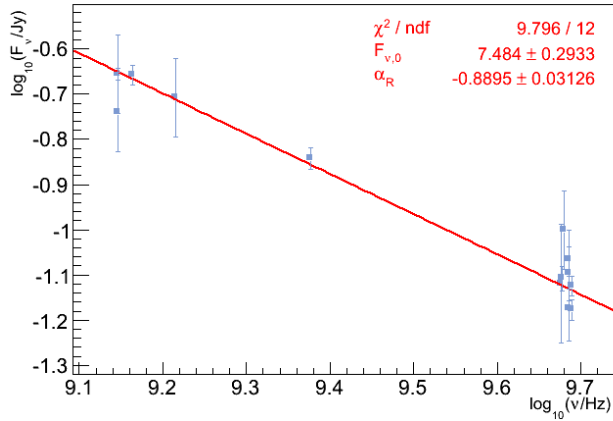
This procedure invokes a *cleaning algorithm* which checks the stability of the set of data points in the radio range 0.843-5.0 GHz. This stability is checked by taking into account the deviation of each data point with respect to the fit, meaning that, if the point is 4σ away from the fit, the point is excluded from the set of data, and the fit is re-calculated. Once the fit is re-calculated, the same procedure is executed in an iterative way. This continues until all the data points are within 4σ respect to the fit, after which, the slope of the fit is calculated.

As described in section 2.3, sources with an FSI $\alpha_R > -0.5$, which is represented by the slope of the fit described above, indicates that their radio-jet is pointing to the observer, and are classified by us as interesting objects referred to as Flat Spectrum radio AGN . Nevertheless, in order to be conservative, the selection of sources here requests a FSI within one sigma of the threshold value α_R of -0.5, that means, an object is requested to fulfil $\alpha_R + \sigma_{\alpha_R} > -0.5$. In fig. 4.5, two examples are shown to illustrate

the performance of the fit, where one source falls into the Flat Spectrum radio AGN category, and the other one is rejected based on its too steeply falling radio spectrum.



(a) ARP 220. This is an example of a source passing the Flat Spectrum radio AGN selection.



(b) NGC 7674. This source shows a steep radio spectrum which is exposed by the slope value α_R . Consequently, this object does not fall into the definition of a Flat Spectrum radio AGN .

Figure 4.5: Two objects from different categories in the catalog of radio-emitting galaxies [120]. The fit in the radio range $\nu = 0.843\text{-}5$ GHz is shown.

The FSI distribution as calculated above, for the whole set of sources in

a limited volume, is shown in fig. 4.6. In this distribution, 98 sources fulfill the Flat Spectrum radio AGN condition, which requests an FSI $\alpha_R + \sigma_{\alpha_R} > -0.5$.

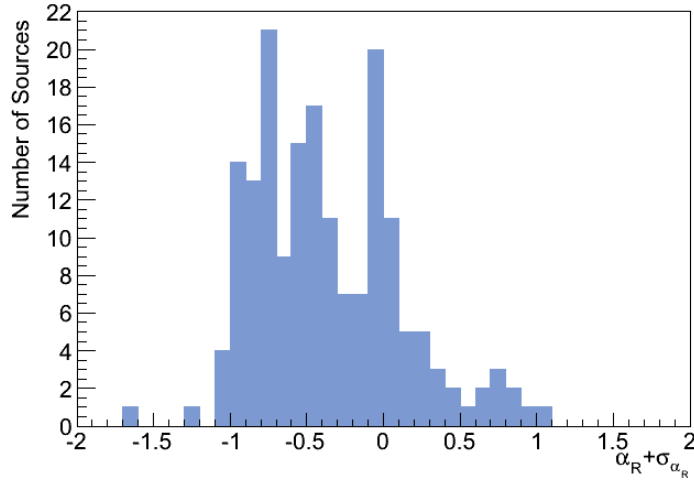


Figure 4.6: The FSI distribution calculated by the cleaning algorithm. The number of sources that fulfill the Flat Spectrum radio AGN condition is 98

4.4 Limited Volume Flat Spectrum Radio AGN

A sample of 98 sources of the class of Flat Spectrum radio AGN in a limited volume has been obtained. On that sample, the criterion to select Obscured Flat Spectrum Radio AGN will be applied. As previously explained, one of the features that Obscured Flat Spectrum radio AGN should fulfill, is that radiation fluxes at highest frequencies in the electromagnetic spectrum are attenuated or completely absorbed by the surrounding dust. Meanwhile radiation at low frequencies, as in the radio band, could pass through the dusty medium without being affected. These effects indicate the AGN Obscuration phenomenon described in Chapter 2.4. Consequently, common frequency windows in the sample of 98 sources for the low (radio) and highest (X -ray to γ -ray) frequencies should be available.

Searching for the more abundant frequencies in radio as well as the highest frequencies, such as the X -ray or γ -ray emission, it turned out that frequencies of $1.4 \cdot 10^9$ (radio) and $3.02 \cdot 10^{17}$ (X -ray) [Hz] are the ones

with more abundant measurements in NED. Although they are the more repeated frequencies, some of the remaining objects did not contain flux measurements at these frequencies.

In the case of a lack of data at the radio frequency of $1.4 \cdot 10^9$ Hz, which happens mainly for objects in the southern hemisphere with a declination below -30° where the data is provided by SUMSS, the flux is obtained by using the fit algorithm described in the previous section 4.3, since the fit provides a function F_ν , the fit algorithm can obtain a proxy-flux at $\nu = 1.4 \cdot 10^9$ Hz. In fig. 4.7, the performance of this proxy-flux is displayed for the objects that have a given flux in NED at $\nu = 1.4 \cdot 10^9$ Hz, where it is observed that the proxy-flux can reproduce the real data rather well.

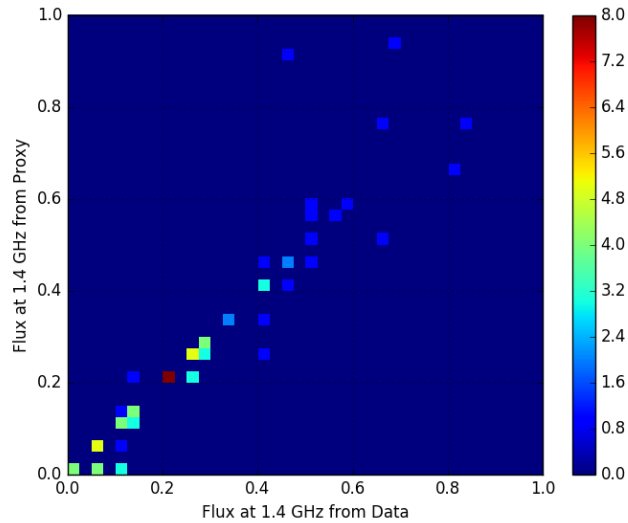


Figure 4.7: The performance of a proxy-flux based on the spectral fit is displayed for the objects that have a given flux in NED at $\nu = 1.4 \cdot 10^9$ Hz

On the other hand, for a lack of data at $3.02 \cdot 10^{17}$ [Hz], the situation is different, since there is not a well known power law which can describe the X-ray behavior in this frequency band. Because of this, it is not possible to obtain a value for the flux through a proxy-flux as made for the radio flux. Therefore, sources with a lack of data at $3.02 \cdot 10^{17}$ [Hz] are excluded. Consequently, due to a lack of data, 36 sources were excluded from the previous sample of 98 sources within a limited volume and with a flat spectrum radio spectrum, reducing the sample to 62 sources.

Appendix A shows a table with the 62 Flat Spectrum radio AGN within a limited volume, with data flux at $1.4 \cdot 10^9$ and $3.02 \cdot 10^{17}$ [Hz]. The position of the source in the sky, redshift, FSI and the fluxes at $1.4 \cdot 10^9$ [Hz] (radio) and at $3.02 \cdot 10^{17}$ [Hz] (X-ray) are given.

4.5 Obscured Flat Spectrum Radio AGN Selection

Starting from the sample of the 62 objects within a limited volume, with flat radio spectrum and with available data (or calculated by the Proxy-Flux in at the radio frequency) at $1.4 \cdot 10^9$ and $3.02 \cdot 10^{17}$ [Hz], we will now construct our catalog of Obscured Flat Spectrum Radio AGN. In this sample of 62 sources, 49 objects are located in the Northern sky and 13 in the Southern Hemisphere.

As already mentioned, an Obscured Flat Spectrum Radio AGN can be identified by the fact that it is emitting weakly at frequencies ν in the X-ray and γ -ray bands of the electromagnetic spectrum, in particular, $\nu = 3.02 \cdot 10^{17}$ [Hz], which is the chosen frequency for this analysis as pointed out in section 4.4.

One can only determine whether a source has low emission at a certain frequency ν , when one compares it with other sources emitting at the same frequency. However, one could bias the comparison, because the engine of a source is not efficient to produce energy.

As explained in section 2.2, the X-ray radiation from AGN could be emitted from different components of the AGN. Thus, the comparison of sources must be made between objects of the same category that have similar spectrum/morphology characteristics. In our sample we distinguish three source categories, 14 Flat Spectrum Radio Quasars (FSRQs), 45 BL Lactertae (BLLac) objects and 3 Ultra Luminous Infrared Galaxies (ULIRGs). The sample is split in FSRQs and BLLacs considering the Fermi classification given in [81].

The spectra of objects in the FSRQ category exposed in [52], show two bumps, one in the radio band and the another one in the X-ray part of the electromagnetic spectrum, which is not the case for BLLac objects. Therefore, this fact strengthens the idea of splitting our AGN population between FRSQs and BLLacs. The ULIRG distinction was observed by analyzing the spectra of each object in our sample of 62 sources selected up to now, and indeed few objects show a big bump in the Infrared band, therefore, objects with this feature were classified as ULIRG.

The ULIRG object class, and especially ARP 220, is still under detailed investigation [123, 124, 125], where indications have been found that an AGN is present in, at least some of these objects [124]. Even though it is not determined whether or not there is an AGN located inside ARP 220 and NGC 3690, we decided to keep them in our selection based on the fact that strong (flat spectrum) radio emission has been observed which is most likely due to synchrotron emission. Hence particle acceleration takes place at these sources. This in combination with the very strong dust component, makes them very interesting candidates for high-energy neutrino production through the proton-matter interaction channel.

In the FSRQ sample composed of 14 sources, we exclude from our analysis the galaxy 3C273 due to its extremely high X -ray and radio emission, which implies that this object has a very powerful engine compared with the rest of our sample in this category. Moreover, the high X -ray emission in this object is attributed to be emitted from the jet instead of arising from the accretion disc [126].

In the ULIRG sample composed of 3 objects, the NGC 3628 galaxy was excluded. Since the measurements given in NED are unsuitable for our analysis. The two X -ray flux measurements for NGC 3628 are: $(9.93 \pm 6.62) \cdot 10^{-10}$ and $(3.68 \pm 3.11) \cdot 10^{-8}$ [Jy] registered by Chandra and XMM telescopes respectively. The large uncertainties make these measurements compatible with background, which would imply that the spacial telescopes did not have the capability to detect a clear signal at $3.02 \cdot 10^{17}$ [Hz], or indeed this object has a very low X -ray emission. Nevertheless, this latter fact in addition to sharp telescopic views as shown in fig. 4.8 make it worth to investigate this object as a possible neutrino source powered by proton-matter interaction, and consequently will be studied using IceCube data as explained in the next Chapters.

Another fact that may be considered to study the galaxy NGC 3628, is based on the bump in the infrared band observed in fig. 4.9. The infrared emission can be expected due to the warm dust that is heated by a central engine of the galaxy. As will be explained afterwards, in our model we identify objects that have a strong X -ray emission, hence there is no matter in our line of sight or is not dense enough, and subsequently they are unobscured. So, a sub-band of the infrared spectra of NGC 3628 was investigated and compared with several unobscured objects, as presented in fig. 4.10, where the blue-triangles correspond to NGC 3628 data, and the rest correspond to objects that do not fall into our category of Obscured Flat Spectrum Radio AGN. As displayed, the green points (data of the galaxy NGC 5506, that shows a high X -ray luminosity according to our model)



Figure 4.8: Picture of the NGC 3628 galaxy, also known as The Hamburger Galaxy. According to our model, the radio spectrum indicates that there is a radio jet pointing towards us. Credits: [52]

show mostly a higher luminosity than the ones for NGC 3628. Therefore, we may not directly state that there is a correlation between X -ray and infrared emission, and further investigation should be done. Therefore, we can not say that: High-Infrared implies Obscured-FSRQ.

So, after excluding 2 objects (3C273 and NGC 3628) from our sample of 62 objects, this is reduced to 60 sources. In table 4.5 the number of sources per each category is presented.

In order to avoid a comparison between galaxies with a weak engine with objects that indeed have a low luminosity due to an obscuring matter, we normalize the X -ray luminosity at $3.02 \cdot 10^{17} [\text{Hz}]$ by the radio emission at $1.4 \cdot 10^9 [\text{Hz}]$. For FSRQs, there are studies that show a correlation between those two bands [127, 128], and the correlation is exposed by the relation, $L_R = L_X^\beta$. Here, we have used L_R and L_X for the radio and X -ray luminosity respectively, and the value of β ranges in $\beta = 0.6 - 0.7$ [127, 128].

Fig. 4.11(a) shows the correlation between L_X and L_R at $3.02 \cdot 10^{17} [\text{Hz}]$ and $1.4 \cdot 10^9 [\text{Hz}]$ respectively for objects in the FSRQ and ULIRG categories.

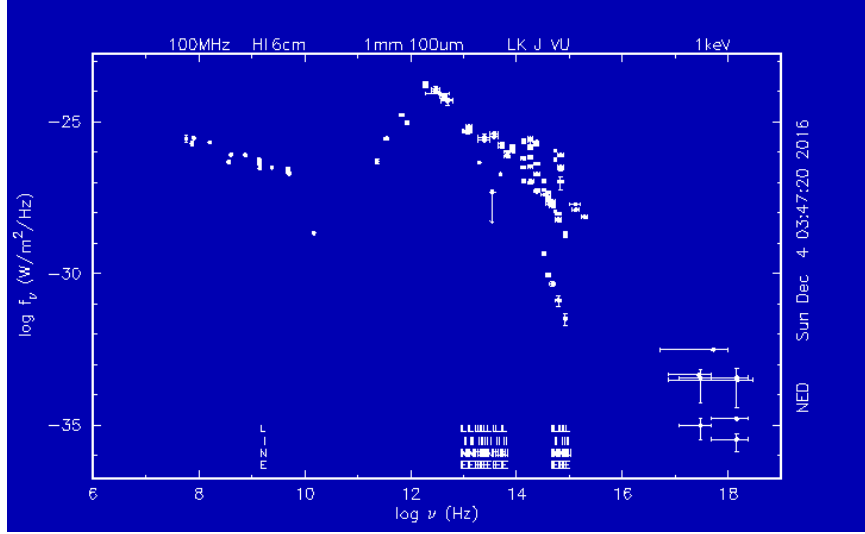


Figure 4.9: Spectra of the ULIRG NGC 3628 galaxy as presented in [52].

Class	$N_{initial}$	Excluded	N_{final}
FSRQ	14	3C273	13
ULIRG	3	NGC3628	2
BLLac	45	—	45

Table 4.1: The final number of objects (N_{final}) that will be analyzed in the next section, to investigate whether they can be classified as Obscured Flat Spectrum Radio AGN.

The fit gives a value of the slope equal to $\beta = 0.73 \pm 0.04$, which reproduces the value of β found in [127, 128]. Hence, for these two categories of objects a normalized intensity is given by $I_{F-U} = L_X^{0.73}/L_R$ which will be used to compare the X -ray intensity of objects in the FSRQ and ULIRG classes. We use the sub-index $F-U$ to denote FSRQ-ULIRG.

On the other hand, we applied the same procedure for objects in the BLLac category to investigate a possible correlation between radio and X -ray luminosities. As shown in fig. 4.11(b), no correlation is observed.

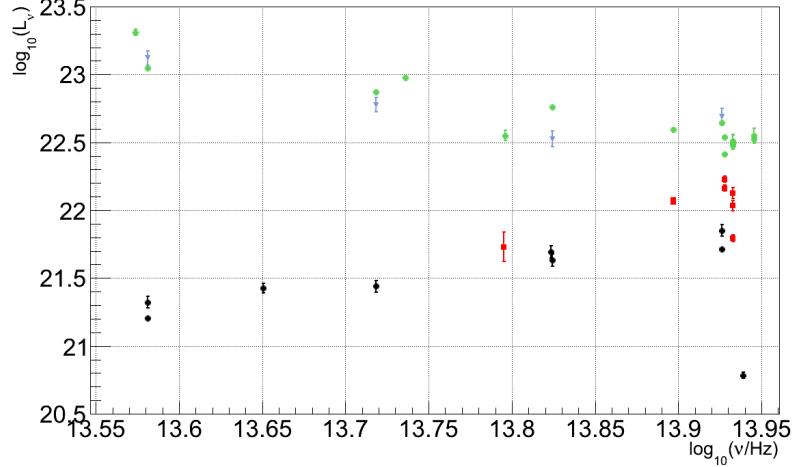


Figure 4.10: Luminosity in the Mid InfraRed band for several objects in the FSRQ category (one color per object). The NGC 3628 spectrum is exposed through the blue triangles (the hamburguer galaxy as displayed in fig. 4.8), which shows a bump in the InfraRed band as shown in fig. 4.9. The rest of the spectra correspond to objects that do not fall into our category of obscured AGN due to their strong X -ray emission. If one compares the infrared emission of the galaxy NGC 3628 with the object NGC 5506 (green points), both have high infrared emission. Nevertheless, only NGC 3628 is expected to be obscured.

4.5.1 Obscured Flat Spectrum Radio AGN Population

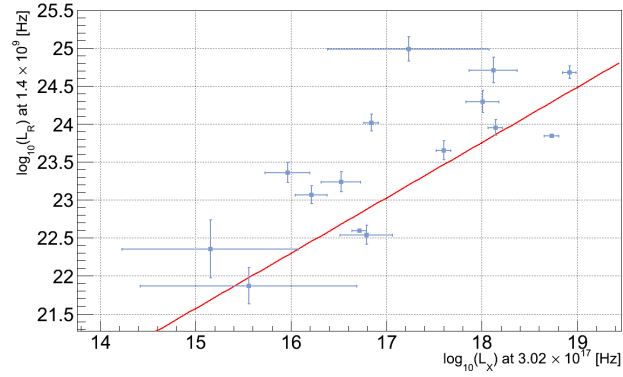
So far we have split our sample of 60 objects (62 but 2 excluded) in two categories for determining what objects have low X -ray intensity at $3.02 \cdot 10^{17}$ [Hz], which is an indication for considering an AGN as obscured. These categories are FSRQs-ULIRGs, and BLLacs. The criterium to determine whether a source in the current sample has low X -ray luminosity, consists of grouping each category in quartiles of the intensity value given by:

$$I_{F-U} = L_X^{0.73} / L_R \quad (4.3)$$

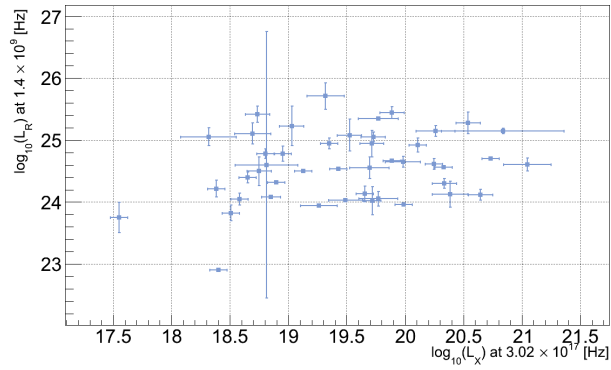
for the category composed of FSRQs-ULIRGs, and

$$I_B = L_X \quad (4.4)$$

for sources in the BLLac sample.

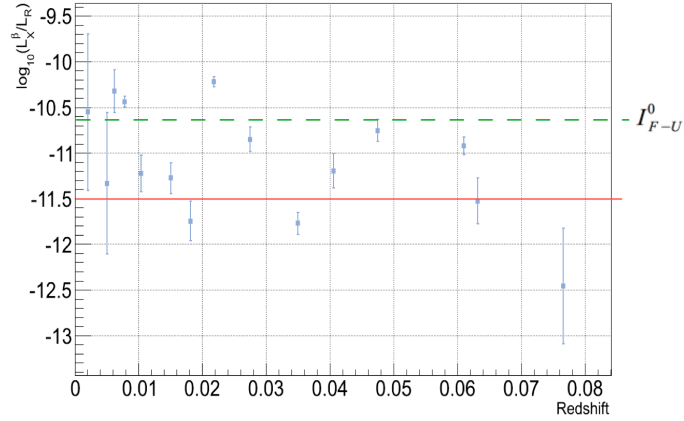


(a) Correlation between the radio and X -ray luminosities for objects in the FSRQ and ULIRG categories. The value of the slope is $\beta = 0.73 \pm 0.04$

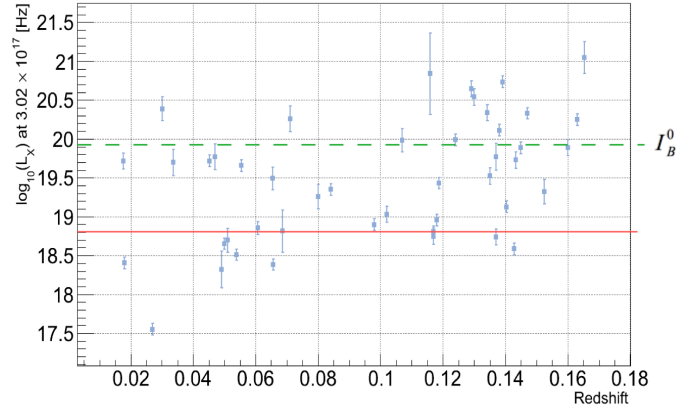


(b) Radio vs X -ray luminosity for BLLac objects. No correlation is observed.

Figure 4.11: The correlation between X -ray and radio measurements for our 62 objects split in to categories, FSRQ-ULIRG and BLLac.



(a) The X -ray intensity normalized by the radio luminosity as a function of redshift for objects in the FSRQ-ULIRG category. The red line indicates the quartile with lowest X -ray intensity, whereas the green line defines the quartile with strongest X -ray intensity.



(b) The X -ray intensity as a function of redshift for objects in the BLLac category. The red line indicates the quartile with lowest X -ray intensity, whereas the green line defines the quartile with strongest X -ray intensity.

Figure 4.12: Representation of the quartiles of X -ray luminosities at $3.02 \cdot 10^{17}$ [Hz].

Class	N	I^0
FSRQ-ULIRG	15	$2.3 \cdot 10^{-11}$
BLLac	45	$9.7 \cdot 10^{19}$ [W/Hz]

Table 4.2: The intensity I^0 for each class with N objects. This value of the intensity is a cut-off that indicates what sources, with an intensity larger than this value, are unobscured. The intensity for the FSRQ-ULIRG class is a power of the X -ray luminosity normalized by the radio luminosity as given in eq. 4.3, whereas the cut-off intensity for the BLLac category is just the X -ray luminosity at $3.02 \cdot 10^{17}$ [Hz] (eq. 4.4).

The distributions of the intensities versus redshift for sources in both categories are shown in figs. 4.12(a) and 4.12(b). As indicated above, we compare the luminosities of the remaining objects to each other in order to distinguish the ones that have the weakest observed intensities. Consequently, in our model, the lower (or first) quartile defines the objects that have the lowest X -ray intensity at $3.02 \cdot 10^{17}$ [Hz], which could be explained by a column of matter located in our line of sight causing the AGN obscuration. The value of the intensity that defines the top quartile (or third) and sets the sub-sample of objects with strongest X -ray luminosity, is assumed to be due to non-obscured sources and as such is used to define I^0 as indicated in eq. 2.11. This intensity will be used to estimate the amount of matter in our line of sight, and can consequently be used to determine the amount of protons that interacts with that column of matter. The values for the reference intensities for the two categories FSRQ-ULIRG and BLLac are exposed in table 4.2.

Table 4.3 shows the Obscured Flat Spectrum Radio AGN population that we obtained according to the lower (or first) quartile of the X -ray intensity as described above. The sky map in Equatorial coordinates according to the J2000 frame [52] for the Obscured Flat Spectrum Radio AGN population is shown in fig. 4.13. The FSRQ objects are indicated with red points, the ULIRG ARP220 in blue and BLLac objects in olive.

4.5.2 Estimation of the fraction of protons interacting with the obscuring material in Obscured Flat Spectrum Radio AGN

Followed by the determination of the Obscured Flat Spectrum Radio AGN population, we are interested in estimating the amount of protons that will

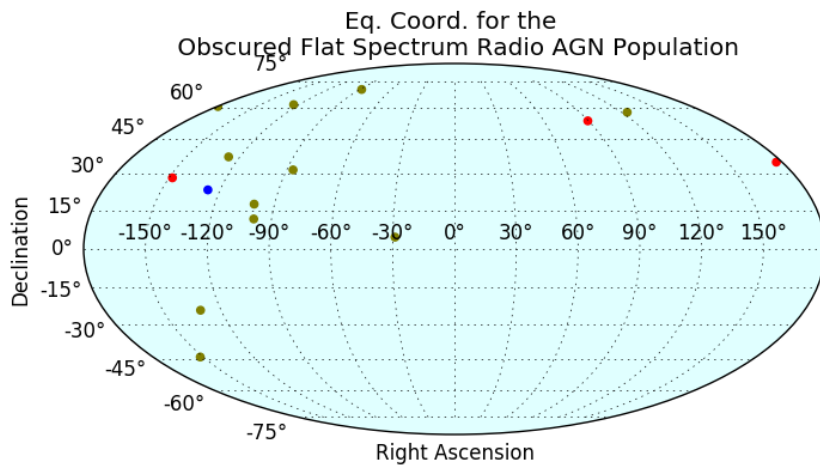


Figure 4.13: Our Obscured Flat Spectrum Radio AGN population. The FSRQs in red, the ARP220 ULIRG in blue and BLLac objects in Olives.

Object name	RA	Dec
Class: FSRQ		
2MASXJ05581173+5328180	89.5	53.5
CGCG186-048	176.8	35.0
MRK0668	211.8	28.5
Class: ULIRG		
ARP220	233.7	23.5
Class: BLLac		
3C371	271.7	69.8
B21811+31	273.4	31.7
SBS0812+578	124.1	57.7
GB6J1542+6129	235.7	61.5
RGBJ1534+372	233.7	37.3
SBS1200+608	180.8	60.5
PKS1349-439	208.2	-44.2
4C+04.77	331.1	4.7
1H1720+117	261.3	11.9
APLibrae	229.4	-24.4
PKS1717+177	259.8	17.8

Table 4.3: table

Object names classified as Obscured Flat Spectrum Radio AGN , and their Righ Ascension (RA) and Declination (Dec) in Equatorial coordinates.

interact with the obscuring material. This fraction would give us an indication of the amount of (additional) neutrinos produced in Obscured Flat Spectrum Radio AGN. As mentioned before, the protons that would be generated in the AGN environment and accelerated in the AGN-jet, become cosmic-rays if they are able to escape from the source environment. These cosmic-rays cover a large energy range as presented in fig. 3.2.

The amount of protons that are expected to be absorbed in the obscuring material can be obtained through [46, 87]:

$$I = I^0 \exp\left(\frac{-X_{matter}}{\lambda_{proton}}\right). \quad (4.5)$$

This relation gives the intensity I of a beam of particles, hence protons that are accelerated in the jet, after passing through a column depth of matter X_{matter} , and with an initial beam intensity of I^0 .

The above equation is also expressed in terms of the interaction depth λ_{proton} that, as shown in eq. 3.1, depends of the proton energy through the cross section. As shown in fig. 3.2, high energy protons could be emitted from astrophysical objects, as AGN. Hence a value for the proton matter cross section, as would be expected in Obscured Flat Spectrum Radio AGN, should be taken at the proper energy. The maximum energy reached by particle accelerators at Earth is limited to $\sim 10^{17}$ eV in the laboratory frame of the particle ($\sim 10^{13}$ eV in the center of mass). Nevertheless, The Pierre Auger cosmic-ray observatory has reported an interaction depth of $\lambda_{p-air} = 56\text{gcm}^{-2}$ for a mean proton energy of $E = 10^{18.24}$ eV that interacts with the terrestrial atmosphere [129]. Therefore, to approach a realistic astrophysical situation, we will use this value for the interaction depth to estimate the fraction of protons that interacts with the obscuring material as expected in Obscured Flat Spectrum Radio AGN.

The Pierre Auger interaction depth measurement is for proton-air interaction ⁴, hence, the target material of the proton for that measurement is a mixture of mainly Nitrogen ($\sim 80\%$) and Oxygen ($\sim 20\%$). The AGN dust composition is not well known, but some studies based on infrared observations indicate that the composition could contain Carbon and Silicon [22]. Therefore, the Pierre Auger interaction depth for proton-air has to be extrapolated considering the AGN dust composition. As mentioned, Carbon and Silicon would be part of the AGN dust, nonetheless, we also make an

⁴Since the Pierre Auger interaction depth measurement was obtained from a proton interaction with air, the calculation performed in section 2.4.1 for the X-ray interaction depth at 1.24 keV is also made for air.

extrapolation considering other elements that are abundant in the universe, as Hydrogen, Nitrogen, Oxygen and Iron.

Due to the cross section dependency of the interaction depth, as shown in eq. 3.1, the extrapolation of the Pierre Auger measurement to proton-H, C, N, O, Si and Fe can be obtained using the following relation:

$$\sigma \propto A^{2/3}, \quad (4.6)$$

and the amount of particles per unit mass that scales like:

$$\rho_N \propto A^{-1}, \quad (4.7)$$

where A is the mass number (number of nucleons) of a target obscuring material.

From eq. 4.6 and eq. 4.7, we can write the interaction depth of the a proton, λ_{p-N} , in terms of the of the mass number A :

$$\lambda_{p-N} \propto (\text{gcm}^{-2})A^{1/3} \quad (4.8)$$

So, to calculate the fraction I/I^0 in eq. 4.5, the problem is reduced to obtain X_{matter} .

In our model published in [35], we present a method to estimate X_{matter} based on the X -ray attenuation in the obscuring material of an AGN. This method considers I^0 as given by the last quartile of the X -ray intensity as explained before, and presented in table 4.2. Thus, X_{matter} can be obtained via:

$$I = I^0 \exp\left(\frac{-X_{matter}}{\lambda_{X-ray}}\right), \quad (4.9)$$

where I can be obtained per individual object.

In the scenario of a mixed composition for the AGN obscuring material, as H, C, N, O, Si and Fe, the interaction depth λ_{X-ray} in the above equation has to be calculated for such elements. As performed in section 2.4.1 for an air composition, this can be obtained from XCOM [104], and as explained before, we consider photons interacting via Compton scattering with the obscuring material. The X -ray interaction depths for all those elements are shown in table 4.4, as well as λ_X/λ_{p-N} , which will be used in the next eq. 4.10.

From eq. 4.5 and eq. 4.9, the fraction of protons that is expected to interact with the obscuring material in Obscured Flat Spectrum Radio

Dust composition	λ_{p-N} (g cm ⁻²)	λ_X (g cm ⁻²)	λ_{p-N}/λ_X
H(A=1)	23	14	1.6
C(A=12)	53	55	1.0
N(A=14)	56	62	0.9
O(A=16)	59	80	0.7
Si(A=28)	71	55	1.3
Fe(A=56)	89	84	1.1

Table 4.4: Proton and X -ray interaction depth λ_{p-N} , λ_X for different materials as expected in Obscured AGN. The ratio between the proton interaction depth and the X -ray attenuation depth is also displayed.

AGN can be written as:

$$\frac{I_p^{int}}{I_p^0} = 1 - \left(\frac{I_X^{obs}}{I_X^0} \right)^{\lambda_X/\lambda_{p-N}}. \quad (4.10)$$

From eq. 4.10 we can estimate the amount of protons that would interact with the obscuring material. Those fractions are presented in table 4.5 for the Obscured Flat Spectrum Radio AGN population found in section 4.5.1, for the different compositions of the obscuring material.

Object name (NED ID)	H	C	N	O	Si	Fe
Class: FSRQ						
2MASXJ05581173+5328180	0.79	0.93	0.94	0.97	0.87	0.91
CGCG186-048	0.71	0.88	0.90	0.94	0.79	0.85
MRK0668	0.92	0.99	0.99	1.00	0.96	0.98
Class: ULIRG						
ARP220	0.79	0.93	0.94	0.97	0.86	0.91
Class: BLLac						
3C371	0.84	0.95	0.96	0.98	0.90	0.94
B21811+31	0.81	0.94	0.95	0.98	0.88	0.92
SBS0812+578	0.87	0.97	0.98	0.99	0.93	0.96
GB6J1542+6129	0.82	0.95	0.96	0.98	0.89	0.93
RGBJ1534+372	0.86	0.97	0.97	0.99	0.92	0.95
SBS1200+608	0.89	0.98	0.98	0.99	0.94	0.97
PKS1349-439	0.85	0.96	0.97	0.98	0.91	0.95
4C+04.77	0.97	1.00	1.00	1.00	0.99	1.00
1H1720+117	0.89	0.98	0.98	0.99	0.94	0.97
APLibrae	0.90	0.98	0.99	0.99	0.95	0.97
PKS1717+177	0.83	0.95	0.96	0.98	0.89	0.93

Table 4.5: The fraction of protons which is expected to interact with the obscuring material for each Obscured Flat Spectrum radio AGN.

Chapter 5

The IceCube Neutrino Observatory

So far, I have discussed obscured flat spectrum radio AGN as possible sources of high-energy neutrinos. A sample of this sub class of AGN has been selected as explained in the previous Chapter to be analyzed using IceCube data and resources. As such, it is instructive to give an overview of the IceCube detector before going to the analysis details.

The IceCube detector overview presented here aims to explain the performance of the IceCube detector, the experimental setup, and how data processing at the South Pole is performed. I also expose here how events are simulated, and explain the main angular reconstructions as used for this analysis.

5.1 The IceCube Detector

5.1.1 Detector Location and Geometry

The IceCube deep ice detector is located near the geographical South Pole at $S89^{\circ}59'24''-W63^{\circ}27'11''$ at depths between 1450-2450 meters, with an instrumented volume of one cubic kilometer [26]. The right handed coordinate system of the detector is such that the y axis is in alignment with the Prime Meridian, and points towards the city of Greenwich in UK, whereas the z coordinate is normal to the surface of the Earth pointing upwards.

Several studies based on Monte Carlo simulations were performed before constructing the IceCube detector. These studies considered different topologies for the detector geometry, trying to optimize the effective

area, angular resolution and background rejection in order to achieve the best sensitivity for Point Source and Diffuse analyses [130]. Currently, the IceCube detector is composed of 86 Strings and 5160 Digital Optical Modules (DOMs) attached to these strings. These DOMs are placed between 1450 and 2450 meters under the ice surface, where it should be noted that, between $z = -2107$ m and $z = -1850$ m there is a reduced sensitivity because of the presence of a dust layer. Fig. 5.1 shows the detector geometry in its $x - y$ plane that has the shape of a hexagon. The vertical spacing between DOMs is on average ~ 17 meters, except for the DeepCore infill array for which the vertical spacing is on average ~ 7 meters. The horizontal spacing corresponds to ~ 125 meters, except for the DeepCore strings which are about 70 meters apart.

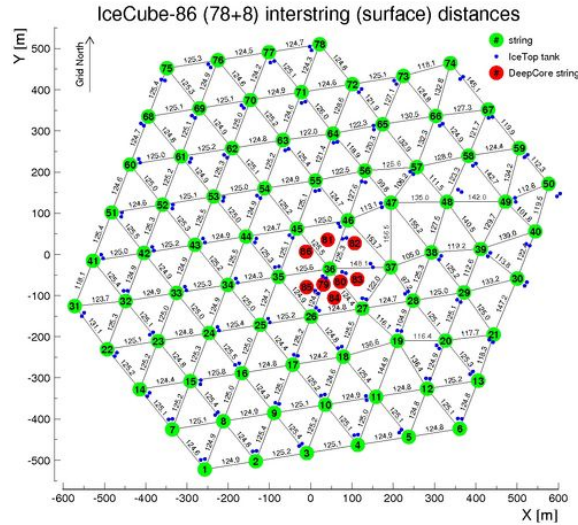


Figure 5.1: The String configuration for the whole IceCube detector in the x - y plane. The spacing between strings in the Deep Core array (red marks) varies between ~ 40 to ~ 72 meters, whereas for the rest of the detector the spacing is ~ 125 meters. Credits: internal IceCube graphics.

This detector has been built in seven phases, as shown in table 5.1.1. Its construction started in 2005 and was completed in 2010.

The DeepCore configuration, which differs from the rest of the volume concerning the spacing of the strings and the separation of the optical modules, allows to perform studies on low energy neutrinos such as neutrino oscillations [131]. A smaller spacing between DOMs allows to reconstruct

Season	N Installed Strings	Total N Strings
2004-2005	1	1
2005-2006	8	9
2006-2007	13	22
2007-2008	18	40
2008-2009	19	59
2009-2010	20	79
2010-2011	7	86

Table 5.1: The seven phases of the IceCube detector deployment. The number of installed strings per season and the total number of strings after the installation are shown [133]. Data collection to be used in the first analyses started using 22 strings [134].

shorter tracks, as the ones produced by low energy muons induced by neutrinos of few GeV, and hence is more sensitive to low energy events. Fig. 5.2 shows an artistic view of the full IceCube detector, where the IceTop configuration also is indicated. This component of the detector aims to cosmic-ray detection and to study their properties, as composition and spectrum [132].

5.1.2 The Various Signals in the Detector

The IceCube detector is located in ice, which has several advantages with respect to other media like for instance seawater and freshwater. For example, seawater has background emitted from the decay of Potassium 40, which is also recorded by the DOMs, whereas, in lakes of freshwater, a neutrino observatory can hardly be installed due to the needed large volume of these devices. Nevertheless, the detector installation in ice has the disadvantage that once the deployment has been performed, the instrumentation can not be recovered [135].

When a charged particle moves faster than the speed of light in a certain medium it produces what is called ‘‘Cerenkov Radiation’’. This actually is what takes place in the IceCube detector with muons. These muons are produced by charged current neutrino interactions, or induced by cosmic-rays that interact with the terrestrial atmosphere as illustrated in fig. 5.3.

Fig. 5.4 illustrates the Cerenkov radiation produced by a particle moving at a speed of $v = c\beta$ in a medium of index of refraction n . It follows that the angle between the direction of the particle and the produced wave front

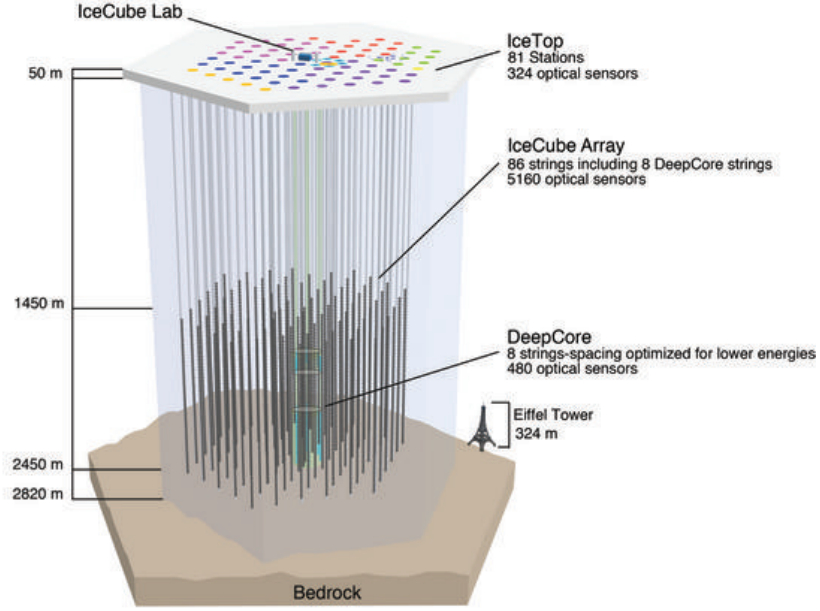


Figure 5.2: The IceCube detector configuration after its completion and including the Deep Core array configuration. Credits: internal IceCube graphics.

can be written as:

$$\cos \theta = \frac{1}{n\beta} \quad (5.1)$$

This angle, the so called Cerenkov Angle θ_c , has a value of $\theta_c \sim 42$ deg in ice. This is due to the index of refraction, which in ice equals $n = 1.31$ [87], and for the particle energies that we consider we have $\beta \approx 1$.

The produced “light” is converted into an electric charge and consequently to a deposited energy in the detector. As such, IceCube has an energy threshold of ~ 100 GeV [135]. Nevertheless, a particle in the detector of 100 GeV will not provide a good angular resolution. Due to the large spacing between DOMs, only few of these devices will be “fired” preventing to perform a good track reconstruction. This actually can be exposed through an extension of the Bethe-Bloch formula that describes the energy loss (also known as stopping power) of particles, as muons, when they travel through

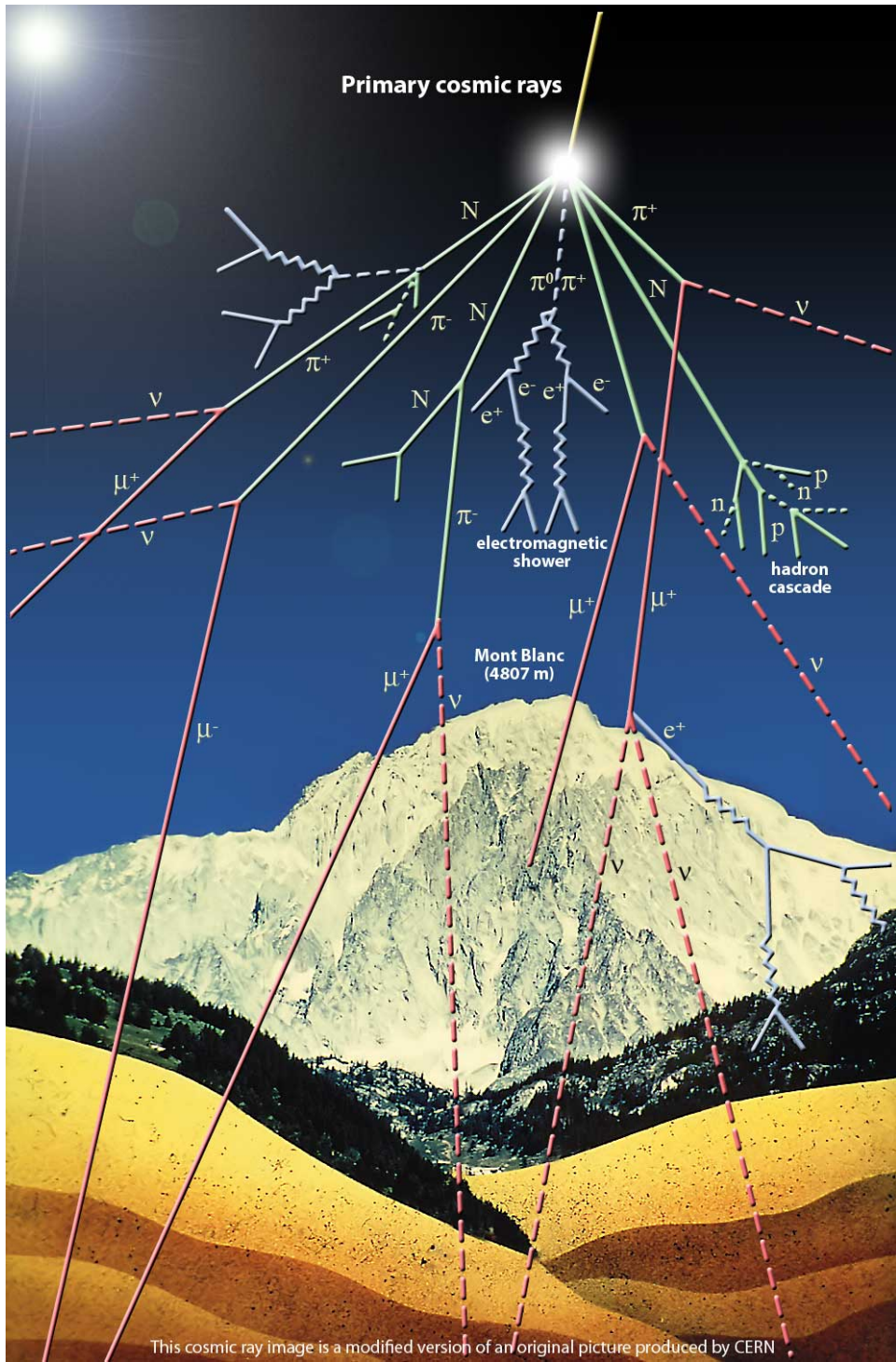


Figure 5.3: Particle shower induced by a cosmic-ray interaction with the atmosphere. Credits: [136].

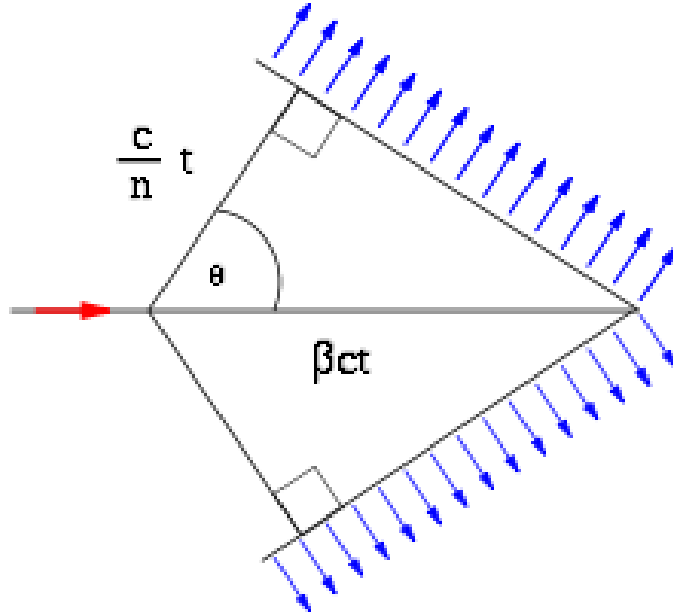


Figure 5.4: Illustration of the Cerenkov radiation produced by a particle that moves at speed v , in a medium of index of refraction n .

a medium along a depth X [87]:

$$-\frac{dE}{dX} = a + bE, \quad (5.2)$$

where E is the energy of the particle, and a is the ionization energy loss constant, and b the stochastic energy loss constant that includes bremsstrahlung, pair production and photo-nuclear scattering [137]. Those values correspond to $a = 0.260 \text{ GeV m}^{-1}$ and $b = 0.000357 \text{ m}^{-1}$ [138]. A simple analysis of the above equation tells us that a muon of a 100 GeV will lose all its energy in around 380 meters in ice. Therefore, if the muon gets into the IceCube detector in a horizontal way, this will not “fire” more than 3 DOMs, and consequently the reconstruction will not have a good accuracy.

When the “light” produced by a charged particle moving in the IceCube detector hits the photocathode in the DOM, it produces photoelectrons (PEs)¹ that are read out by a Photo-Multiplier Tube (PMT) as an analogue signal, the so called “waveform”. Subsequently, if this signal exceeds a discriminator threshold (0.25 PEs) [133], it is digitized by an Analog Tran-

¹Note that a typical PE has an amplitude of 0.7-0.8 [mV] [133].

sient Waveform Digitizer (ATWD) and/or Fast Analog to Digital Converter (FADC)². After this procedure, the information is stored and becomes the basis for pulse extraction and track reconstruction algorithms as outlined below:

- InIceRawData: Raw Digital data for events in the InIce detector. This information will be converted to InIce Pulses afterwards.
- IceTopRawData: Raw Digital data for events in IceTop. This information will be converted to IceTop Pulses afterwards.
- JEBCEventInfo: Information concerning the recording status of an event, for example if an error was found in the data acquisition.
- I3EventHeader: This contains the run id, the event id and the time of the event.
- I3DAQData: Raw binary buffer of data that is the IceCube DAQ data.
- QFilterMask: Information about the 24 filters.
- DrivingTime: Time corresponding to this event.

Once the signal is registered by the DOMs, pulses are created when the charge registered by a DOM exceeds a threshold value, which is defined as 25% of the charge generated by a single photo electron [133].

An IceCube event is defined when at least four pairs of neighboring DOMs are fired within a time window of 5 μ s. If this so called Simple Multiplicity Trigger (SMT8) condition to create an event is fulfilled, the times of the first (t_{init}) and last (t_{last}) trigger pulse are extended to read out the whole event in a time window of: $[t_{init}-10\mu\text{s}, t_{last}+22\mu\text{s}]$ [139]. Those values are valid for events in ice, which are the ones used in this thesis. Other event formation algorithms are applied for events in IceTop.

Following the event formation, track reconstruction algorithms are performed. The basic ideas of a track reconstruction are based on the time information of the hits, e.g. earliest and latest pulses would define the direction of the incoming particle.

A first track reconstruction algorithm (first guess) is called “LineFit”, which is the fastest algorithm that is used in IceCube. Nonetheless, it is the

²ATWD considers a time window of 422 [ns], which is divided in 128 bins, which implies that the time binwidth corresponds to 3.3 [ns]. On the other hand, FADC covers an interval of 6400 [ns], which is split in 256 bins, so each bin has a width of 25 [ns] [133].

least precise. This reconstruction ignores the Cerenkov geometry and the optical properties of the ice. Given the position r_i of a DOM that has been “illuminated”, at time t_i , the direction of a track can be obtained through [140]:

$$\vec{r} = \langle r_i \rangle - V \langle t_i \rangle, \quad (5.3)$$

where V represents the velocity of the particle and is given by:

$$V = \frac{\langle r_i \times t_i \rangle - \langle t_i \rangle \times \langle r_i \rangle}{\langle t_i^2 \rangle - \langle t_i \rangle^2}, \quad (5.4)$$

To illustrate a track passing through the IceCube detector, we show in fig. 5.5 a real muon event induced by a muon neutrino. This event produced 130000 photo electrons, with a reconstructed zenith angle of 101 degrees (up-going track), and with a muon reconstructed energy (deposited in the detector) of 2.3 PeV [141]. This is the most energetic neutrino event observed so far.

The IceCube detector has a trigger rate of ~ 3000 events per second, which are almost purely dominated by atmospheric muons, and muons generated in the detector due to atmospheric neutrinos [139]. These particles are induced by cosmic-ray interactions with the terrestrial atmosphere, which produce mesons that decay in muons and neutrinos via the processes described in Chapter 3. However, only atmospheric muons with an energy above 300 GeV can reach the instrumented IceCube volume, since low energy muons lose their energy in the ice before they reach the detector [139, 143]. An artistic view of the produced shower of particles induced by a cosmic-ray is presented in fig. 5.3.

However, this rate of ~ 3000 Hz changes according to the seasons of the year (seasonal variation). During summer the terrestrial atmosphere is warmer, which implies that it is less dense compared to winter periods. This effect contributes in the following way to the higher atmospheric muon flux observed in summer with respect to the winter season; Pions and kaons created in the high atmosphere have less chance to lose energy and interact with this diluted summer atmosphere, hence, the probability to decay in muons and neutrinos is larger than in winter [143, 144].

Fig. 5.6 shows the relative down-going muon rate variation (blue curve), $\Delta R_\mu / \langle R_\mu \rangle$, collected between April-2008 and July-2011 at the IceCube detector [144, 143]. The same quantity for the neutrino variation is shown by the black points with errors bars. They show a clear correlation with the relative effective temperature variation (black curve) $\Delta R_T / \langle R_T \rangle$.

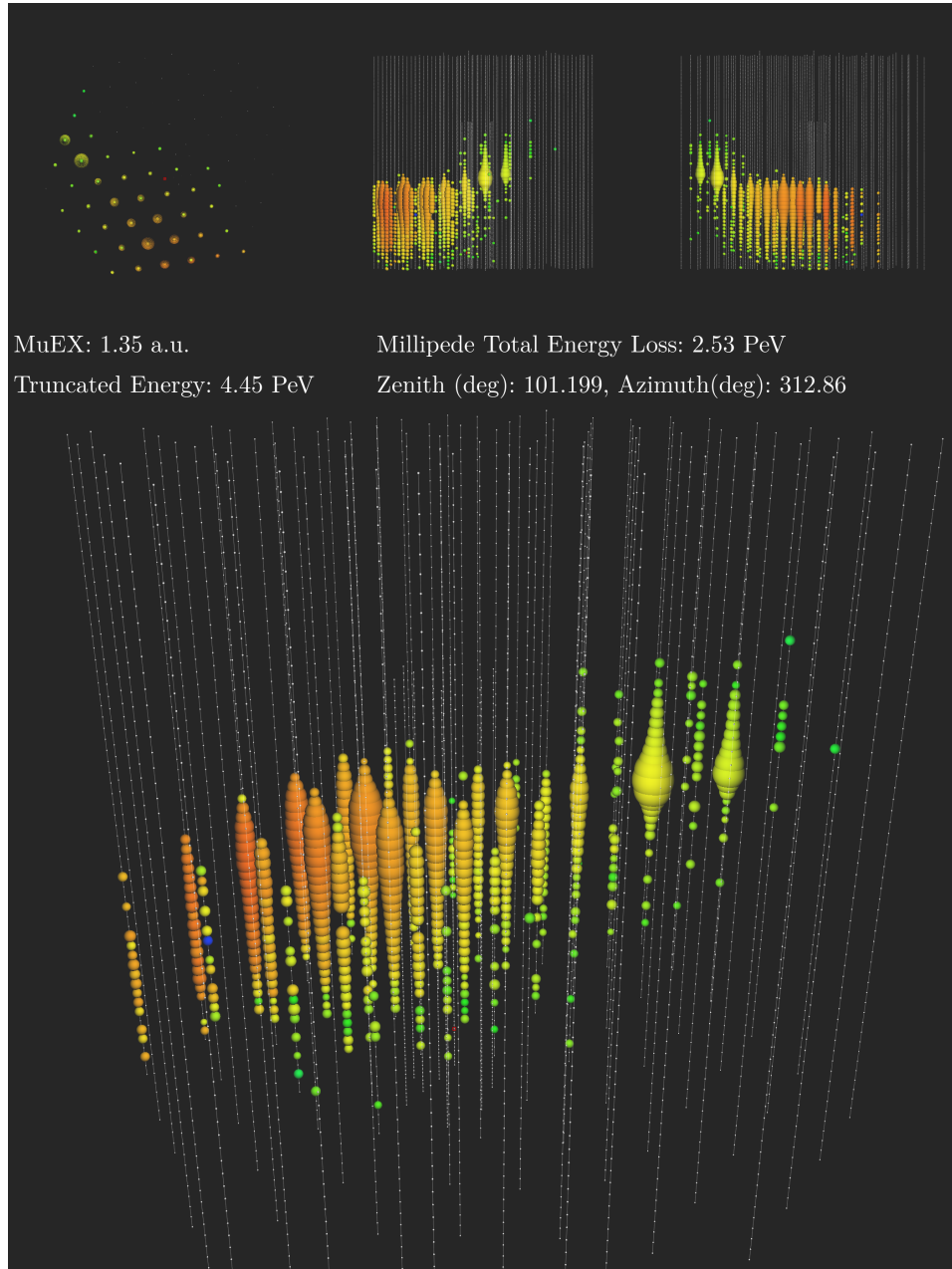


Figure 5.5: The most energetic neutrino event (ν_μ) observed so far. This data was registered in June of 2014. Credits: [142]

5.1.3 Triggering Filtering and Transfer System

After the data collection at the South Pole, so-called *Online Data*, the data is transferred to the University of Madison Wisconsin, United States, via Tracking and Data Relay Satellites (TDRS), which are administrated by NASA [145]. The satellite bandwidth for data transfers from the South Pole to Madison amounts about 105 GBytes per day [133].

An amount of data corresponding to 3000 Hz is not possible to transfer to Madison via satellites, therefore, a data reduction is made before to transfer it. The data reduction, that is based on 24 filters, is a first event selection ran at the South Pole. To illustrate the performance of these filters, we outline below the MuonFilter, IOnlineL2Filter and the EHEFilter, which are the ones used in this IceCube analysis to investigate Obscured Flat Spectrum Radio AGN.

- MuonFilter: This is based on the *PoleMuonLlhFit* track algorithm reconstruction (PMLLh), the number of fired DOMs (NCh) and the total charge of the event (QTot).

The PoleMuonLlhFit track reconstruction takes into account the separation in time and distance of the pulses with respect to a seed track hypothesis. This reconstruction algorithm considers the difference between the observed pulse time and the one that is expected, which is known as *time residual*. Since this algorithm considers the “probability” that a track creates an observed pulse $\vec{x}_i = (x_i, y_i, z_i, t_i)$, this kind of reconstruction receives the name of *Likelihood reconstruction*. The Likelihood formula \mathcal{L} can be written as [146],

$$\log \mathcal{L} = \log \prod_i p(\vec{x}_i|\vec{a}), \quad (5.5)$$

where \vec{a} corresponds to the track parameters (θ, ϕ, x, y, z) . Hence, the “most likely probability” that a track creates pulses with parameters \vec{x}_i is obtained by minimizing the function $-\log \mathcal{L}$.

The MuonFilter considers two regions in the detector via the following selection:

- Upgoing region: This region is defined by a zenith angle larger than 78.5° as reconstructed by the PoleMuonLlhFit reconstruction. In this region the track reconstruction features has to fulfill the condition $\log \mathcal{L}/(NDoms - 3) \leq 8.7$, where NDoms is the number fired DOMs.

- Downgoing region: This is the geometrical counterpart of the upgoing region as described above. In addition we also request a minimum charge of the event, in order to reject rejects low energy atmospheric muons.
- IOnlineL2Filter: This filter uses the events passed from the MuonFilter, and applies a more precise reconstruction, so called MPEFit (described below). The MPEFit reconstruction has to fulfill the same criterion as the PoleMuonLlhFit in the MuonFilter as outlined above. This reconstruction, that is more precise as the PoleMuonLlhFit, is processed only on the events passing the MuonFilter, since it is a CPU intensive task. This filter is also used for Follow-up neutrino events and fast response analyses ³, as Optical and Gamma-ray follow up via partner observatories [133].
- EHEFilter: Selects events with a total number of photo-electrons (Q_{Tot}) larger than 1000 [133]. This charge selection criterion allows to eliminate low energy atmospheric muons, which produce a small amount of charge in the detector.

As mentioned before, events tagged by the various online filters are sent to Madison via satellite. Nevertheless, all triggered recorded data is saved on disks at the South Pole base, and subsequently transported to the North at the start of the Austral summer season.

The number of filters can change according to different “running” seasons that start in May, and is decided by the collaboration through the Trigger Filter Transmission (TFT) Board. This committee is in charge of Data Acquisition (DAQ) software tasks, trigger setting and satellite transmission. However, the filters used in the current analysis and outlined above are always present.

After data arrival at the University of Madison, the rate of experimental data is $\sim 750[\text{Hz}]$, which varies according to the seasons of the year as previously described. These data are processed offline using various sophisticated Likelihood reconstructions. The obtained level of data reduction is called “Level2”, and is the starting point for the IceCube Event Selection that will be described in the next Chapter.

³A follow-up and fast response analysis refers to information that is sent by IceCube to partner observatories, as gammas-ray and optical telescopes, when a high-energy neutrino event is registered in the IceCube detector, and it has characteristics of being an astrophysical neutrino.

To illustrate the amount of data that is available at Level2, and consequently the one that is the starting point for several analyses, fig. 5.7 shows the InIce rate at Level2 for a single run. This rate is calculated selecting InIce events and requesting LineFit track reconstruction to be in the frame⁴ and with physical values for its angular variables⁵. This run corresponds to data collected in October of 2012, with a life time of 7.7 hours, which is the typical life time for a run in the IceCube neutrino observatory. In that figure, a zenith angle $< 90^\circ$ indicates the rate for down-going events, hence, events coming from the Southern Sky according to the LineFit reconstruction. This clearly indicates that the rate of data for events coming from the Northern hemisphere is lower than in the Southern sky. This reduction for the Northern hemisphere is due to the natural shielding of the Earth against atmospheric muons induced by cosmic-rays. Fig. 5.7 exposes two bumps at 0 and 180 degrees, which mostly correspond to misreconstructed tracks. A small inclination of a track with respect to the normal to the surface, will mimic a vertical track instead of a track of a few degrees of inclination. These two bumps are not present in more sophisticated reconstruction algorithms.

5.2 Event Simulation in the IceCube Experiment.

In this section we illustrate how the event simulation works in IceCube. This can be outlined through the following steps:

1. Generation of particles with random directions, and energies in a certain range. Among the generated particles are neutrinos that are created by the IceCube neutrino event generator, so-called NuGen [147], which is used to simulate our neutrino signal. On the other hand, the muon background is simulated using CORSIKA (COsmic Ray SIMulations for KAscade) [148], which creates primary cosmic-rays showers that subsequently produce atmospheric muons. These neutrinos and cosmic-rays are called *Primary Particles*. Note that the neutrino is generated at the detector, whereas a cosmic-ray is generated in the

⁴A frame in the IceCube software refers to the information produced by an event, as pulses, reconstruction, event time, etc.

⁵When a reconstruction algorithm is not able to reconstruct the direction of a track in the detector, caused for example when the number of pulses in the event do not fulfill the condition to perform the track reconstruction, the observables of the reconstruction are set as non physical values.

atmosphere and the induced muons (atmospheric muons) are the ones that eventually reach the IceCube detector.

2. Following the generation of a primary particle, its daughter particles are propagated through the detector. In the case of a primary muon neutrino, this can produce a muon (in case of a charged current interaction) and a hadronic shower, which afterwards produce “Cerenkov-photons”. The same kind of photons are produced by atmospheric muons entering in the detector. All these particles are put in a container⁶, which is called I3MCTree, (MC indicates Monte Carlo).
3. Once the I3MCTree is created, we want to obtain the response of the PMTs when the Cerenkov-Photons hit them. This response is given via the generation of MC photo-electrons, which are stored in a container that is called, I3MCPESeriesMap. This object contains the information of each fired DOM, such as the charge and time of the photo-electrons that are ejected from the photocathode. This task is lead by one of the following projects: photonic-service (I3PhotonicsHitMaker), elsim or ppc.
4. Once the I3MCPESeriesMap is created, additional MC noise photo-electrons are generated in order to mimic the detector noise. This is performed through the Vuvuzela project, which returns an I3MCPESeriesMap including simulated noise.
5. The next step in the simulation chain is to create MC pulses, which is performed by the PMTResponseSimulator module⁷ part of the DOM-Launcher project. Here, I3MCPESeriesMap is the input information and the output is a container that has the MC pulses associated to each fired DOM, called I3MCPulseSeriesMap.
6. At this point, we have all the information related to the pure “True Monte Carlo”. However, in order to mimic real data, this MC information has to be converted into reconstructed information, which I refer to as: “Reco Monte Carlo”. We first create DOMLaunches,

⁶A container is an object in programing languages that stores other objects.

⁷A module in the IceCube Software, so-called IceTray, refers to a component (basically a programing code) of the software that allows to make certain operations that are fundamental to accomplish physics analyses. Examples of these operations are, direction reconstruction, simulation of particles, generate data files, etc. IceTray modules are written mainly in C++ and Python programing languages. These modules are placed inside of projects, whereas IceTray is composed of about 100 projects.

as the ones that are collected in real experimental data. This is performed by the DOMLauncher project, where the input information is an I3MCPulseSeriesMap, and the output is an I3DOMLaunchSeriesMap. This process of conversion mimics the DOM electronics to produce waveform characteristics. Furthermore, this also checks if the signal is local coincident, which means, it checks whether the signal was registered by the neighboring DOMs in a certain time window. This coincidence between pulses in neighboring DOMs defines what is known as Hard Local Coincident pulses.

7. After having obtained the container with DOMLaunches, these objects have to be calibrated for known characteristics of the electronics, for instance a Voltage Calibration. This is performed by the I3WaveCalibrator module, part of the WaveCalibrator project. The container that has the information of the calibrated DOMLaunches is called: InIceRawData.
8. Finally, we proceed to create an I3RecoPulseSeriesMap, which will contain the extracted pulses based on the calibrated DOMLaunches information stored in InIceRawData. The I3RecoPulseSeriesMap object is created via the module I3Wavedeform, part of the wavedeform project. This is the starting point for running track reconstruction algorithms as is performed for real experimental data.

More information about the simulation projects mentioned above can be found in the IceCube Software webpage [149]

5.3 Other Directional Reconstructions at Level2

After obtaining the data from the South Pole in the University of Madison in U.S. (as described in section 5.1.3) and running more sophisticated algorithms of reconstruction, as explained hereafter, the level of the data reduction is called “Level2”. At this level, the rate of data is ~ 600 [Hz].

Below, I outline other track reconstruction algorithms that are processed at Level2 data and used on the IceCube event selection that is presented in the next Chapter.

- SPEFit2, the acronym means Single Photo-Electron. This is a reconstruction based on the maximum Likelihood method as the one outlined in the previous section. The fact that this name refers to a single

photo electron, indicates that the pulses used for this reconstruction are assumed to originate from a single photon hitting a certain PMT [133].

- MPEFit also consists of a track reconstruction based on maximum Likelihood. Nonetheless, this differs from the SPEFit2 reconstruction since it uses multiple photoelectrons that hit the PMT in a certain time window [133].

The angular resolution at Level2 as given by LineFit, SPEFit2 and MPEFit is presented in fig. 5.8. The effectiveness of these directional track reconstructions is investigated in the event selection described in next Chapter. The angular resolution is calculated by the following dot product,

$$\psi = \arccos(\vec{r}_{primary} \cdot \vec{r}_{reco}), \quad (5.6)$$

where $\vec{r}_{primary}$ is the unit direction of the simulated primary particle and \vec{r}_{reco} is the reconstructed unit direction.

Furthermore, the performance of the angular reconstruction for MPEFit, lead by charged and neutral current neutrino interactions is shown in fig. 5.9. This figure shows that the less precise angular reconstruction is obtained when the neutrino interacts by NC, that as explained above, is due to the absence of a muon in the final state. On the other hand, the blue line shows the median angular resolution for the track reconstruction when the NuMu neutrino interaction is lead by charged current, which indeed shows a large improvement with respect to the one obtained with an NC interaction. At highest neutrino energy the angular resolution is expected to improve due to the fact that the muon in the final stage will have more energy and consequently travel a longer distance in the detector. In the last two situations, the simulated neutrino events include muon background in order to accomplish a realistic situation as is expected to occur in real data. This realistic situation aims to reproduce events that can not be split by the IceCube algorithms, due to for example, neutrino and muon background events occur very close in time. The reconstruction based on NuMu-CC simulated events without background also is displayed in fig. 5.9. The reconstruction performance of the latter and the NuMu-CC with background do not present a large difference. This small discrepancy in the median angular resolution indicates that most of the time the splitting algorithms are able to split properly the events.

5.4 High Performance Track Directional Reconstructions

5.4.1 SplineReco Directional Reconstruction

The SplineReco directional (or angular) track reconstruction is the most precise directional track reconstruction in the IceCube software. This reconstruction will be used in this analysis to point tracks back in the sky to correlate them with objects in the Obscured Flat Spectrum Radio AGN population. This reconstruction algorithm is based on *PhotoSpline tables* (or just photon tables). The ice where the IceCube detector is buried has non-homogeneous properties. Certain ice properties, as the purity and density of the ice can change in different parts of the instrumented volume. It turns out that Cerenkov-photons emitted from a certain source (track) in different regions of the detector might not be recorded in a proper way by a PMT. What might occur is that a strong emission could be read out as weak one. This can be solved by using photon tables that play a role of “light-calibrator” [133]. So, the SplineReco is a Likelihood reconstruction that uses photon tables to calibrate the light of the observed photons.

The SplineReco algorithm has several configurations. The *default* configuration is the one that allows to run SplineReco as just described, hence, using Likelihood functions and calibrating the light of the observed Cerenkov-photons via photon tables. On the other hand, the *recommended* configuration uses an energy estimator of the event, which can be obtained by several energy reconstruction algorithms in the IceCube software, which are based on the recorded amount of light. This energy estimator gives a weight to the observed Cerenkov-photons, therefore, this weight enhances the performance of the Likelihood when this tries to find the “probability” that a track creates a pulse.

As explained above, recommended and default are two different configurations for SplineReco, and the performance of those settings is exposed in fig. 5.10 through their median angular resolution. In the legend box of this figure, the attached names to the word “Spline” indicate the seed track used as a first guess for SplineReco. So, SplineMpe means that the seed passed to SplineReco is the MPEFit reconstruction. On the other hand, the name SplineMpeSpe indicates that the first guess reconstructions are MPEFit and SPEFit2. The name that follows to those strings is SRTInIce, which indicates the name of the pulses used for this reconstruction, which is SRTInIce-Pulses. The name of the last strings indicate the names of the reconstruction that provides the energy estimator of the event. The combination between

MPEFit as directional seed for Spline-Reco and MPEFitMuEX as an energy estimator is the one that provides the best angular reconstruction.

Note that in this IceCube analysis for investigating Obscured Flat Spectrum Radio AGN, the directional reconstruction for tracks, as observed in the IceCube detector, is given by SplineReco with energy estimator, which I will refer as “*SplineEnEst*”.

5.4.2 Paraboloid, a Directional Uncertainty Estimator

The error estimation of the track direction can be calculated via the Paraboloid project available in the IceCube software [151]. This is obtained by investigating the variables that are included in the Likelihood that determines the track reconstruction. The Likelihood function \mathcal{L} that would lead to the determination of the error on the reconstruction depends of the following variables: $(\vec{r}, \theta, \phi, \mathbf{P})$. Here, $\vec{r} = (x, y, z)$ is any point along the track, θ, ϕ indicate the direction of the track, and \mathbf{P} is an observed pattern of pulses. The uncertainty on the direction is basically determined by the errors on calculating θ, ϕ , where such errors will yield an error on \vec{r} .

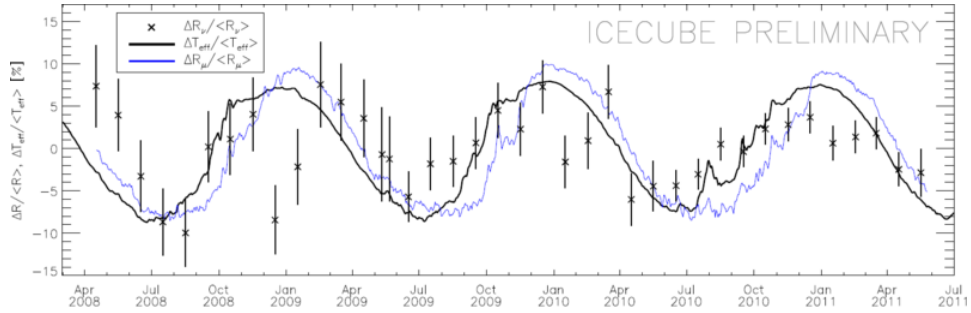


Figure 5.6: Relative muon and neutrino rate variation along different periods collected at the IceCube detector. They show a clear correlation with the relative effective temperature variation. Credits: [143].

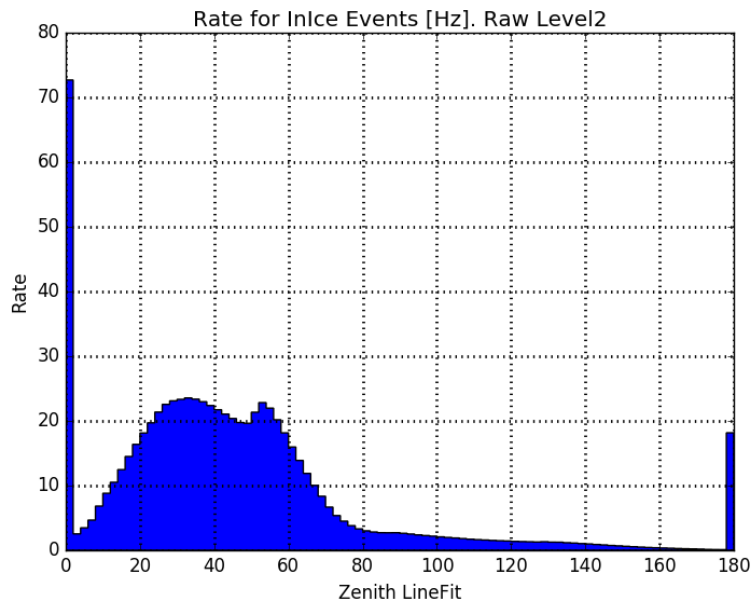


Figure 5.7: LineFit zenith reconstruction (in degrees) at different rates [Hz]. This plot shows the InIce rate of experimental data at Level2, with an integrated rate equal to 746 [Hz]. This data corresponds to a single run, with the Id number: 120630, and the data was collected the 3rd of October of 2012.

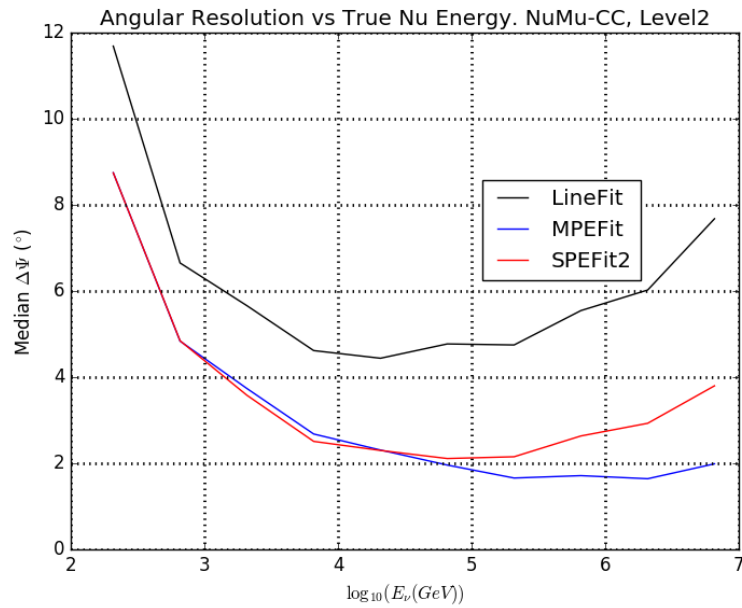


Figure 5.8: MPEFit, SPEFit2 and LineFit median angular resolutions for the NuMu-CC channel. These reconstructions are available at Level2 IceCube data 2012. This has been plotted using the NuGen Simulation data set 11069, and a preselection based on the Detector Filter Criterion was applied first. This official IceCube simulation data was generated in an energy range of $10^2 - 10^7$ [GeV] [150].

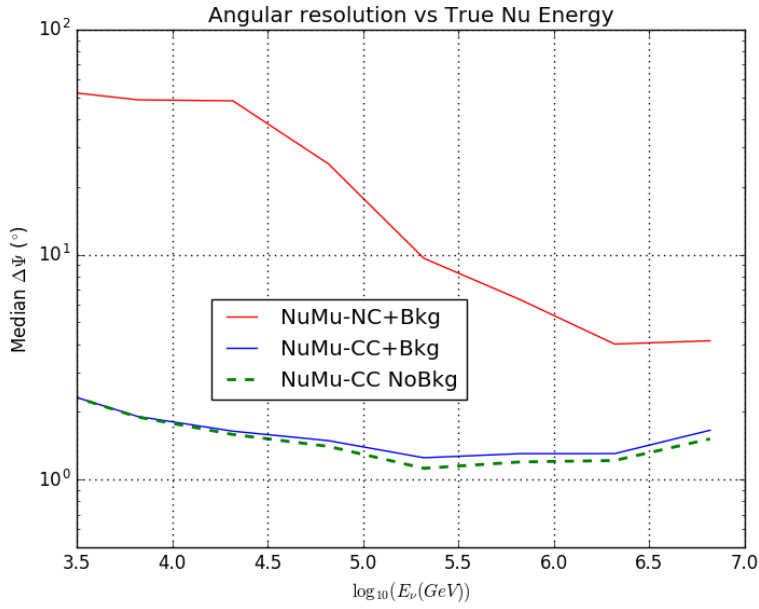


Figure 5.9: Angular Resolution for NuMu interactions in the IceCube detector. Both neutrino interaction channels are shown, Neutral Current (NC) and Charged Current (CC), those neutrino events include simulated atmospheric muon background. This clearly shows that the angular track reconstruction as given by MPEFit, does not provide a good angular resolutions for NuMu-NC interactions. Furthermore, the median angular resolution for a sample of NuMu-CC without Background is shown, this sample is slightly better at mid energy range than the one with Background.

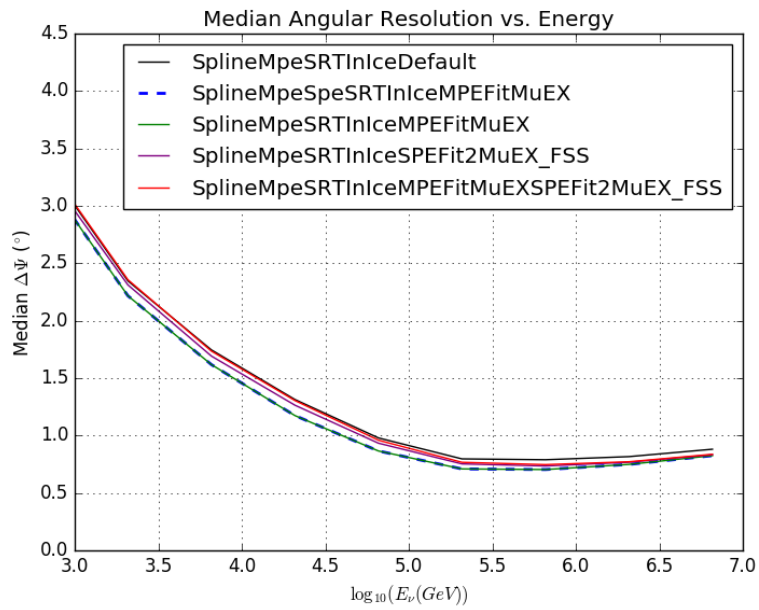


Figure 5.10: SplineReco algorithm reconstruction for different configurations. The so-called “recommended” configuration with a MPEFit as a directional reconstruction guess, and MPEFitMuEX as energy estimator, provides the best median angular resolution.

Chapter 6

Statistical Concepts

The main complication in neutrino astronomy to observe a neutrino emitted from an astrophysical object, is the large rate of background with respect to the expected neutrino signal, as indicated in table 6. The presented rates in this table imply that for each thousand atmospheric neutrinos detected in the IceCube observatory, only a single astrophysical neutrino is observed. Due to this large background, several procedures are applied in order to reduce the background as will be explained in Chapter 7. After these procedures, we reach a level of data cleaning where we can not distinguish atmospheric neutrinos from astrophysical neutrinos. Therefore, we have to apply statistical criteria in order to discriminate signal from background.

In this chapter I outline several statistical concepts that are related to the analysis, such as the Likelihood function, Test Statistic, Discovery Potential and Sensitivity.

EventType	Rate [Hz]	Direction
Atmospheric μ	$\sim 10^3$	from above
Atmospheric ν	$\sim 10^{-3}$	“isotropical”
Astrophysical ν	$\sim 10^{-6}$	“isotropical”

Table 6.1: This table shows the rate of 3 type of events observed in the IceCube neutrino observatory. The direction of those events with respect to the IceCube detector also indicated. Notice that “isotropical” here refers to tracks entering to the IceCube detector from all directions in the sky, nonetheless, they are not equally distributed due to the shielding given by Earth. Credits: [152].

6.1 The Likelihood function

The Likelihood function \mathcal{L} for Point Source analyses in IceCube is [153],

$$\mathcal{L}(\vec{x}_s, n_s, \gamma) = \prod_i^N \left(\frac{n_s}{N} \mathcal{S}_i + \left(1 - \frac{n_s}{N}\right) \mathcal{B}_i \right), \quad (6.1)$$

where this formula shows a dependency of the source position \vec{x}_s , the number of signal events n_s in a certain solid angle Ω around the source and the expected spectral index γ for astrophysical neutrinos. I will refer to the latter as γ_ν .

The *source probability density* \mathcal{S}_i is given by a product between the spatial density function \mathcal{N} , and a probability of observing a reconstructed muon energy E_i at a neutrino source spectral index γ_ν . So, the source probability density can be written as:

$$\mathcal{S}_i(\vec{x}_i, \vec{x}_s, E_i, \gamma_\nu) = \mathcal{N}(\vec{x}_i, \vec{x}_s) \cdot \int_{E_\nu} P(E_i|E_\nu) P(E_\nu|\gamma_\nu) dE_\nu. \quad (6.2)$$

Where the spacial density function \mathcal{N} is given by:

$$\mathcal{N}(\vec{x}_i, \vec{x}_s) = \frac{1}{2\pi\sigma_i^2} \exp\left(-\frac{|\vec{x}_i - \vec{x}_s|^2}{2\sigma_i^2}\right), \quad (6.3)$$

On the other hand, the background probability density \mathcal{B}_i is given by the following expression,

$$\mathcal{B}_i = \frac{P(E_i|\phi_{atm})}{\Omega}, \quad (6.4)$$

where ϕ_{atm} indicates the atmospheric flux.

As explained in [153], the Likelihood formula 6.1 can be independent of the neutrino spectral index γ_ν . This “detachment” on γ_ν will consequently result in a Likelihood dependency only on the number of signal events n_s to discriminate astrophysical neutrinos from atmospheric neutrinos. Another option for coping with the γ_ν dependency (or independency) in the Likelihood formula, it is to set γ_ν according to certain model predictions. The latter approach would fit well in case the predictions by several authors about the neutrino flux in astrophysical sources [15, 18, 19, 20, 21], would actually be observed at the IceCube observatory, nonetheless, this is not what has been observed by IceCube. The latter is actually supported by the

broken power law observed for the high-energy neutrinos detected by the IceCube Collaboration [154].

This possible broken power law for the high-energy neutrinos observed by IceCube is shown in fig. 6.1. We can see in this figure that low energy neutrinos (deposited energy in the detector) can be fit a by a power law $d\Phi_\nu/dE \sim E^{-2.58}$. Whereas the high-energy neutrino spectrum, with a deposited energy larger than 10^3 TeV, seems to follow a harder¹ spectrum described by $d\Phi_\nu/dE \sim E^{-2}$.

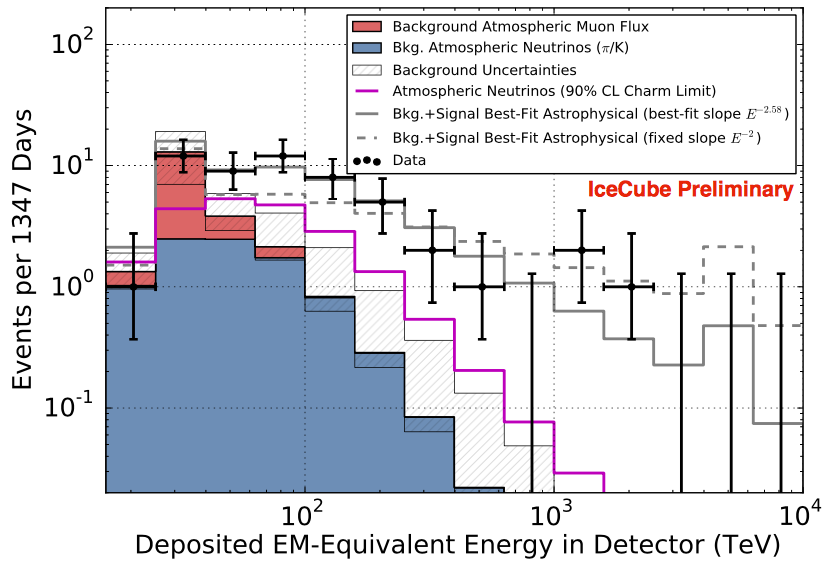


Figure 6.1: Neutrino power law for the high-energy astrophysical neutrinos observed by IceCube. This shows that there is not a unique power law for describing the astrophysical neutrino flux. Credits: [154].

Furthermore, another argument for not fixing a neutrino spectral index γ_ν in the Likelihood formula is the one illustrated in fig. 3.5. As explained in Chapter 3, and illustrated in fig. 3.5, the energy range that we would expect from Obscured Flat Spectrum Radio AGN is broad. Moreover, despite the fact that the result presented in fig. 3.5 is just a motivation and a full simulation is needed, this illustrates that a non-power law spectrum for neutrino emission might be expected. This is in line with the previous

¹Harder neutrino spectrum refers to neutrino energy distribution that contains more high-energy neutrinos.

discussion concerning the neutrino spectral indices based on the already observed astrophysical neutrinos reported by the IceCube Collaboration [154].

In view of the previously exposed, in the Likelihood formula in eq. 6.1 we will use the dependency on γ_ν . Nonetheless, we do not fix it, hence by maximizing $\mathcal{L}(n_s, \gamma_\nu)$ we determine the best matching value for γ_ν . Consequently the free parameters, n_s and γ_ν can be obtained via,

$$\begin{aligned}\frac{\partial \log \mathcal{L}}{\partial n_s} &= 0 \\ \frac{\partial \log \mathcal{L}}{\partial \gamma_\nu} &= 0.\end{aligned}$$

This will allow us to discriminate the expected astrophysical neutrino signal from the atmospheric neutrino background based on two free parameters, γ_ν and the number of signal events n_s .

Note that we investigate the objects in the Obscured Flat Spectrum Radio AGN population individually, so the Likelihood 6.1 is calculated for each source individually, opposite to what is known as a “stacking analysis”. A stacking analysis is an useful technique when a set of sources of the same class is investigated, and they individually emit a flux that is below the discovery potential. If the fluxes of such a set of objects are summed up, the detection probability is larger. Nevertheless, the 14 sources in the Obscured Flat Spectrum Radio AGN sample belong 3 different categories of AGN, FSRQ, BLLac and ULIRG. These 3 categories have different features in the electromagnetic emission, for example as explained before, objects in the FSRQ category show *x-ray* from the accretion disc and the jet, whereas BLLacs typically show emission from the jet. Furthermore, objects in the ULIRG sample show a strong emission in the InfraRed band. Under these observations, we may think that the internal engine is different for these 3 categories, and consequently we might expect different neutrino spectra. Moreover, in our model [35], we expect a different amount of matter for each AGN that blocks the AGN emission which implies different amounts of protons interacting in each AGN (see table 4.5). Consequently, each source is expected to have a different neutrino flux, and we decided to investigate them individually.

In addition to the physical reasons to study the Obscured Flat Spectrum Radio AGN individually, there is a technical issue that supports this approach. This is based on the fact that the detector sensitivity is zenith dependent [119], which implies that the signal from certain regions in the sky might be stronger than others. This zenith dependence of the sensitivity will be described in the next Chapter.

The quantities in the Likelihood formula given in eq. 6.1, and consequently in the probability density function \mathcal{S}_i and \mathcal{B}_i , are the following,

- $|\vec{x}_i - \vec{x}_s|$ is the space angle difference between a reconstructed track \vec{x}_i and the source positions \vec{x}_s . In our case, \vec{x}_i will be given by the SplineEnEst as described in Chapter 5.4.1, and \vec{x}_s by the position of a source in the Obscured Flat Spectrum Radio AGN sample.
- σ_i^2 is the uncertainty on the reconstructed track direction. In this analysis, which is computed by Paraboloid that was introduced in Chapter 5.4.2.
- Ω is the solid angle around the source. For the background determination this covers the full right ascension, nonetheless, the declination band is centered at the source position \vec{x}_s . In this analysis, we consider a declination band of 5° , which is based on the fact that the angular resolution as calculated by SplineEnEst corresponds to $\sim 1^\circ$ at low energies below of 1 TeV. This declination band of 5° is a rather conservative value that keeps tracks within $\sim 5\sigma$.

6.2 Test Statistic

Based on the Likelihood definition, the Test Statistic \mathcal{TS} is obtained by minimizing the function $-\log(\mathcal{L})$ with respect to the parameters n_s and γ_ν [153]. This will provide the most probable value for n_s and γ_ν . Hence, the test statistic is calculated through,

$$\mathcal{TS} = 2 \cdot \text{sign}(n_s) \log \left[\frac{\mathcal{L}(\vec{x}_s, n_s, \gamma_\nu)}{\mathcal{L}(\vec{x}_s, 0)} \right] \quad (6.5)$$

where the Likelihood evaluated at $n_s = 0$ reflects the pure background PDF value. Therefore, \mathcal{TS} grows when the number of events from a source location increase with respect to the number of background events.

6.3 Discovery Potential

To explain the concept of discovery potential, let us consider the “cartoon” displayed in fig. 6.2. Suppose that we perform N times a pseudo-experiment and we calculate these N times a test statistic \mathcal{TS} , such that we obtain a background distribution for \mathcal{TS} as the one represented by the black line in fig. 6.2. It follows that the discovery potential is defined as the threshold

value for a signal strength, such that in 50% of the trials we obtain a test statistic larger than the 5σ threshold value of the background distribution, which according to the cartoon, is a test statistic $\lambda = 40$. Above this 5σ \mathcal{TS} threshold the probability that our results are due to background amounts to $2.87 \cdot 10^{-7}$.

The mathematical expression for the discovery potential flux can be written as [155],

$$\Phi^{5\sigma, 50\%} = \frac{N_{SignalEvents}}{LifeTime \cdot \Omega} \quad (6.6)$$

where $N_{SignalEvents}$ is the number of injected signal events to construct the blue curve in fig. 6.2.

6.4 The Sensitivity

The Sensitivity is the signal strength such that in 90% of the trials of our pseudo-experiments we obtain a test statistic above the median of the background distribution. As didactically illustrated in fig. 6.2, the median of the test statistic distribution is around $\lambda = 5$.

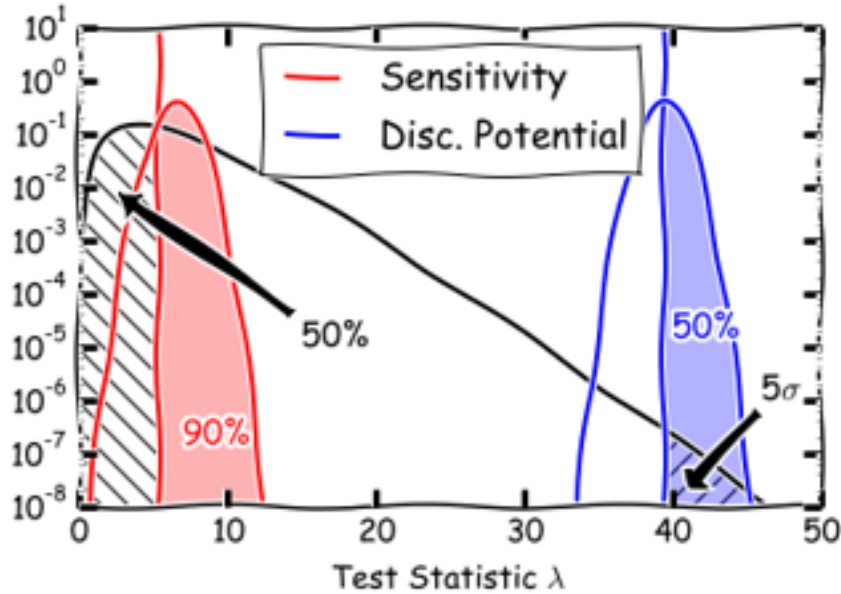


Figure 6.2: Cartoon that illustrates the idea of Test Statistic, discovery potential and Sensitivity. Credits: IceCube documentation.

The mathematical expression for the sensitivity-flux can be written as eq. 6.6, nonetheless, the number of events $N_{SignalEvents}$ used here, corresponds to the ones injected to construct the red curve in fig. 6.2.

Chapter 7

IceCube Event Selection for the Obscured Flat Spectrum Radio AGN Population

The Obscured Flat Spectrum Radio AGN population as described in Chapter 4, is investigated using data and resources from the IceCube neutrino observatory at the South Pole [26]. In this Chapter the event selection for investigating these astrophysical objects will be explained.

Note that despite the fact that there are two Obscured Flat Spectrum Radio AGN in the Southern hemisphere, we will only study the ones in the Northern Sky. This is due to the fact that the IceCube sensitivity is low for studying objects in the Southern Sky [119]. This can be understood considering that the IceCube detector is just shielded by 1.5 km of ice on top of it. Therefore, atmospheric muons coming from the Southern atmosphere, with an energy above of ~ 300 GeV are able to reach the detector. This implies that we have to impose stringent cuts in order to reduce the muon background, which obviously reduces significantly the signal detection efficiency.

The sample of Obscured Flat Spectrum Radio AGN that we study with the neutrino observatory is shown in the sky map in fig. 7.1. This sky map in equatorial coordinates also includes the galaxy NGC 3628, the hamburger galaxy. The reasons for including it were exposed in section 4.5.

At “Level2”, IceCube data is fully dominated by atmospheric muons induced by cosmic-ray interactions with the terrestrial atmosphere. A final neutrino sample in IceCube is defined such that the simulated atmospheric neutrino rate follows our experimental data, that is a rate of few milli Hertz

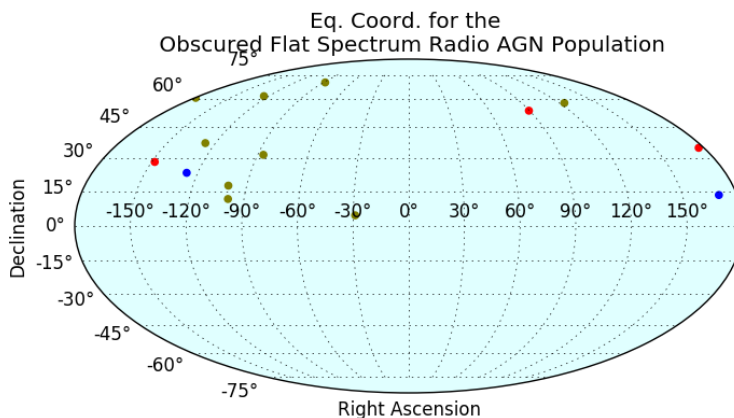


Figure 7.1: The Obscured Flat Spectrum Radio AGN population to be studied with the IceCube neutrino observatory.

(mHz).

The Obscured Flat Spectrum Radio AGN analysis at IceCube falls into the category of Point Source analyses in the IceCube Collaboration, and the Point Source working group of the collaboration has a predefined event selection to accomplish this kind of analyses. This event selection defines the *standard Point Source sample*.

The main goal of an event selection is to separate signal from background. The signal from background discrimination is based on the fact that a muon neutrino induces a single muon, while very often atmospheric muons do not reach the IceCube alone, instead they show up in groups that are known as “muon-bundles”. The average number of muons in a bundle can be written as $\langle N_\mu \rangle = k \cdot E_{primary}$ [139], where $E_{primary}$ is the energy of the cosmic-ray that has induced the muon-bundle. The proportionality constant k depends on certain experimental factors, as for example the altitude of the detector.

Muons bundles have generally low energy, whereas single muons induced by neutrinos are more energetic, so the latter travel longer distances in the detector. Moreover, since the bundle is spatially wider than a single muon,

the photons produced from them are detected in a broader time window than a single muon [146]

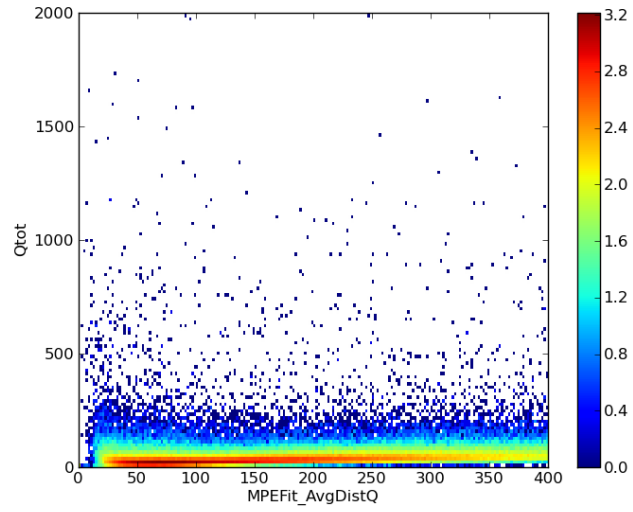
In order to reach the best discovery potential for this analysis at the IceCube neutrino observatory, several existing data sets were investigated to accomplish this goal. Initially, I developed an alternative event selection, which showed an improvement on the discovery potential with respect to the standard Point Source sample. It turned out that the improvement was caused by using a more precise directional reconstruction algorithm. However, the standard Point Source sample keeps more simulated signal events than my alternative event selection. Thus, by combining approaches from the alternative event selection and from the Point Source event selection, an improvement in the discovery potential was achieved with respect to the one obtained with the existing standard Point Source sample.

Below I will outline the event selection in the standard Point Source sample, which is followed by the explanation of how I developed the alternative event selection. Afterwards, I will explain the combined approach to obtain the final event selection for this analysis, so called *PSRepro* (Reprocessed Point Source Sample). In order to perform a consistency check, the PSRepro sample was also compared with the standard event sample used for diffuse flux studies, as outlined in Appendix C.

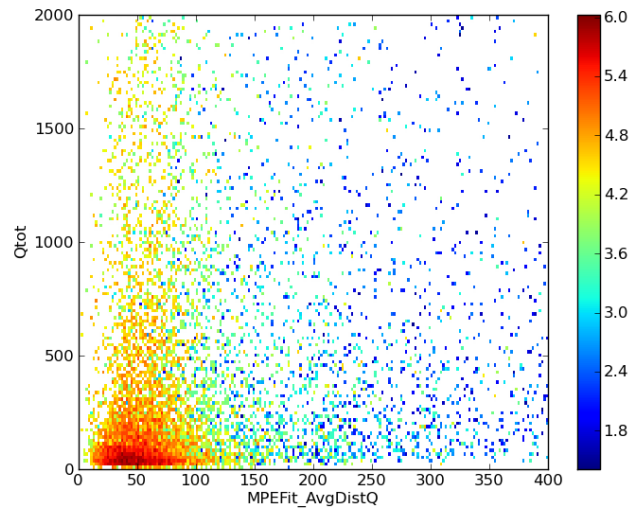
7.1 The Point Source Event Selection

The standard Point Source event selection considers some direct cuts on the data at Level2 in order to reduce the amount of data and allow to run a more precise reconstruction that consumes more computing time. These direct cuts consist of [156]:

1. A first direct cut to reduce the amount of data is based on the detector filters called MuonFilter, and EHEFilter that have been introduced in Chapter 5. This first cut filters out events that are not selected by at least one of those filters.
2. The second cut is based on the variables AvgDomDistQTotDom (described below in section 7.1.1), and the total charge (QTot) of the event. Events that fulfill the condition $\text{AvgDomDistQTotDom} < 90$ or $\text{QTot} > 100$ are kept. The distributions for experimental background and simulated signal are shown in fig. 7.2.
3. A third direct cut is defined by a variable called “RLogL”, that is related with the Likelihood of the reconstructed track and the number



(a) Experimental Background.



(b) Simulated Neutrino Signal.

Figure 7.2: AvgDomDistQTotDom vs Total Charge of in the event. Credits: [156].

of DOMs (N_{doms}) that are fired when a muon passes through the detector, as explained in Chapter 5,

$$RLogL = \frac{\log \mathcal{L}}{N_{doms} - 5} \quad (7.1)$$

A cut on RLogL is set at $MPEFit-RLogL < 8.3$ [156] in the Point Source sample, so all the events that have a RLogL larger than this value are rejected. The MPEFit reconstruction has been outlined before. In fig. 7.3 the dependency of RLogL as a function of the True neutrino energy interacting by Charge Current (CC) in the detector is shown¹. Here it is seen that the cut on RLogL leads to a reduction of low-energy signal events.

The direct cuts on the IceCube data, as outlined above, reduce the experimental data to ~ 2 Hz. Subsequently, a more precise directional track reconstruction is processed, which is SplineReco introduced in Chapter 5.4.1. This level of data processing is called “Level3”.

7.1.1 Point Source BDT Variables

At this stage, the standard Point Source sample is at Level3 and includes a more precise angular reconstruction, SplineReco with the default configuration. Note that at this level of ~ 2 Hz, the IceCube data is fully dominated by atmospheric muons induced by cosmic-rays interacting with the atmosphere.

As mentioned before, we want to obtain the atmospheric neutrino level, which is in order to fully eliminate the atmospheric muon background. At this atmospheric neutrino level, there is however no clue whether there are neutrinos in the IceCube data emitted from an astrophysical object. The atmospheric neutrino rate can be determined from simulation, for which we use a model referred to as “Honda-2006”².

¹Fig. 7.3 has been plotted using the NuGen simulation data set 11069 (2012), which contains NuMu neutrinos plus atmospheric muon background. This simulation was weighted in order to obtain a neutrino flux $\frac{d\Phi}{dE} \propto E^{-2}$. A first filter has been made at Level2 for plotting, that is, the FilterMask has to be present in the frame, and events have to pass the MuonFilter, EHEFilter or OnlineL2Filter condition. Furthermore, some frames do not have MPEFit or its angular variables do not have a physical value since the reconstruction algorithm fails due to the event did not fulfill the requirements to perform the reconstruction. Those events were filtered out as well.

²Honda-2006 model uses a modified DPMJET-III model, in combination with the models FLUKA’97 and Fritiof 7.02 to calculate the atmospheric neutrino flux [157].

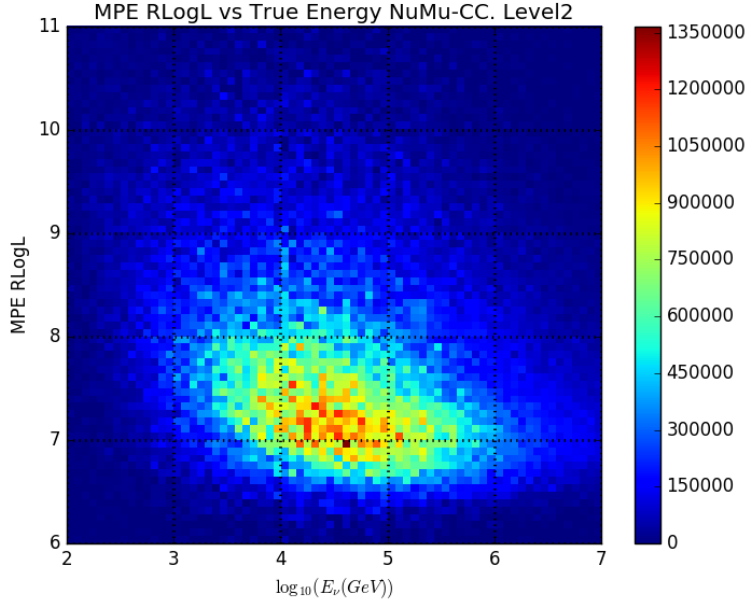


Figure 7.3: RLogL variables as defined by MPEFit track reconstruction algorithm. This shows the correlation with the NuMu-CC True energy.

Subsequently, from the standard Point Source sample at Level3, we have to obtain the atmospheric neutrino level, to ensure that our sample is purely composed of neutrinos. This can be accomplished through Machine Learning Techniques [158], so called BDT (Boosted Decision Tree classifiers) in IceCube [159].

The BDT allows to separate the neutrino signal from atmospheric muon background through reconstructed variables that show specific signatures for both type of events. The signal corresponds to simulated muon neutrinos with an energy spectrum of E^{-2} , whereas for background experimental data is used.

The IceCube variables used in the BDT performance for the standard Point Source event selection, hence “BDT variables”, are explained below [160]. The distributions that represent these BDT variables are shown in Appendix B.

- NDirPulses: This reflects the number of direct pulses associated to a reconstructed track. A direct pulse is a pulses generated by a photon that hits a PMT without making scattering along its trajectory. The

requirement to consider a pulse as direct is such that the difference between the arrival time of a photon and the expected time is near to zero. This difference in time is called *residual time* [161]. This quantity is calculated by the DirectHits module that is in the CommonVariable project part of the IceCube software [162].

- AvgDomDistQTotDom: This variable reflects a weighted average distance of the reconstructed track to the fired DOMs and is defined by the following expression:

$$\frac{\sum_{doms} Distance(dom_i \rightarrow Track) \cdot QTotDom_i}{\sum_{doms} QTotDom_i}, \quad (7.2)$$

where $QTotDom_i$ is the total charge in the i -th DOM, and $Distance(dom_i \rightarrow Track)$ is the closest distance approach from the i -th DOM to the track. This quantity is calculated by the TrackCharacteristic module that is part of the CommonVariable project.

- Center of Charge z-position: this is defined by

$$\frac{\sum_{doms} QTotDom_i \cdot ZPosition_i}{\sum_{doms} QTotDom_i}, \quad (7.3)$$

where $QTotDom_i$ has been described above and $ZPosition_i$ is the z-position of such i -th DOM.

- Cosine of the zenith angle as reconstructed by SplineMPE: The cosine of the SplineReco without energy estimator (default configuration), as explained in Section 5.4.1.
- DirTrackLength: Length of the track considering only direct pulses (the used time window is $[-15\text{ns}, +125\text{ns}]$). This is handled by the DirectHits module which is part of the CommonVariable project.
- EmptyHitsTrackLength: This is defined as the maximal length along a track that has no associated pulses within a certain cylinder centered on the track. This quantity is calculated by the TrackCharacteristics module which is part of the CommonVariable project.
- Logarithm of the directional uncertainty as given by Paraboloid. Paraboloid is explained below in Section 5.4.2.
- RLogL-SplineReco: As mentioned before, SplineReco is a reconstruction based on a maximum Likelihood method. The negative of the

log-Likelihood of the fit, so called $\log \mathcal{L}$, in combination with the number of fired DOMs (N_{doms}), can be used to discriminate signal from background. The RLogL expression is shown in eq. 7.1

- TrackHitsSeparationLength: Separation between the first and last quartile of pulses according to their recording time.

The performance of the standard Point Source event selection is reflected in section 7.3 where a comparison is made with the alternative event selection outlined hereafter.

7.2 An Alternative Event Selection

As mentioned before, I worked on developing an alternative event selection to investigate whether we could achieve an improvement on the sensitivity for this analysis with respect to the standard Point Source sample. Arguments that motivated to work on a different event selection with respect to the already existing standard Point Source event selection are exposed below.

The MPEFit-RLogL cut in the standard Point Source sample is applied in order to reduce the data, and subsequently to run a more sophisticated reconstruction. Fig. 7.3 shows that a fraction of low energy neutrinos do not pass this cut. This is the first motivation to investigate an alternative event selection, hence “we aim to keep additional low energy neutrinos since this might be an important contribution on the expected neutrino flux from Obscured Flat Spectrum Radio AGN”, as previously explained and illustrated in fig. 3.5. A second motivation is based on the fact that in the standard Point Source procedure the neutrino signal used to train the BDT to discriminate neutrinos from atmospheric muon background, consists of a sample that is formed by NC and CC neutrino interactions at the IceCube detector. Nevertheless, one of the questions that could arise is, “why not pass to the BDT a pure CC neutrino sample as neutrino signal?”, which through the BDT performance will allow us to filter out NC events that do not provide precise an angular resolution as shown in fig. 5.9. Furthermore, a final event selection will be applied in order to obtain the best discovery potential per source in the Obscured Flat Spectrum Radio AGN population. Those sources have different positions in the sky, and the performance of the track reconstruction algorithms is zenith depend as will be shown below.

In this alternative event selection I also apply direct cuts in order to reduce the amount of data and to run a more precise angular reconstruction,

nonetheless, they are not expected to remove low energy neutrino events. These direct cuts are the following:

1. Detector Filter Criterion: Based on 3 detector filters: MuonFilter, EHEFilter and IOnlineL2Filter.

As explained before, data acquisition at South Pole requests that at least 1 out of the 24 filters has to pass the condition that indicates an event is not background. The Detector Filter Criterion requests that 1 out of 3 filters, MuonFilter, EHEFilter or IOnlineL2Filter passes the condition.

2. Up-Going Tracks Criterion: Based on 3 different reconstruction algorithms available at Level2, LineFit, MPEFit and SPEFit2 that were introduced in Chapter 5.

We have discussed three track reconstruction algorithms available in IceCube data at Level2 (LineFit, MPEFit and SPEFit2), and the question that arises is, which track reconstruction algorithm would be used to decide whether a track is Up-Going. The answer can be obtained using Monte Carlo information for reconstructed tracks induced by muon-neutrinos interacting in the IceCube detector. Hence, we may use the one that provides the best angular resolution. The median angular resolution for LineFit, MPEFit and SPEFit2 is displayed in fig. 5.8. This figure clearly shows that they have different performance and the best median angular resolution is the one obtained by MPEFit.

The Up-Going Tracks Criterion is based on 3 reconstructed track algorithms MPEFit, SPEFit2 and LineFit. We request that 2 out of 3 of these tracks have to be Up-Going. As shown in fig. 5.8, MPEFit is the one that has the best median angular resolution, nonetheless, as indicated, those are median values.

Events that do not pass the Detector Filter Criterion are rejected. Subsequently, after checking that all 3 reconstructions are in the frame and indeed have physical values, we apply the Up-Going Tracks Criterion. With those criteria we achieve to reduce the data in order to run a more precise angular reconstruction algorithm, just by imposing directional reconstruction. The final numbers after each direct cut applied so far are shown in table 7.1, and the rate of experimental data after each direct cut is shown in fig. 7.4.

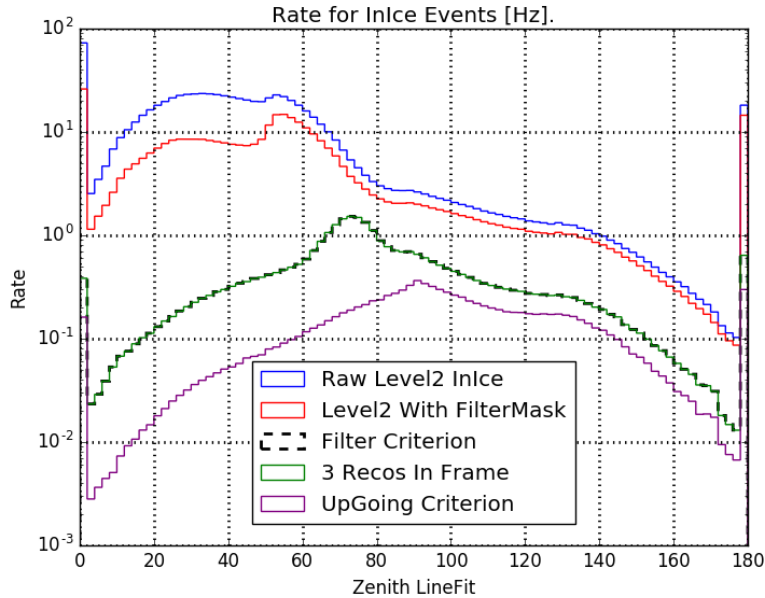


Figure 7.4: Total Rate (blue line) of experimental data, and the rate after each direct cut. Note that the Raw Level2 line reflects the amount of data obtained before any selection. The only request here is that the LineFit reconstruction has to be present in the frame.

Data Type	MaskExists	Filters	RecosExist	Up-Going
Exp (rate)	368.34	33.42	33.39	10.97
SimSignal (%)	95.0	95.0	86.0	80.0

Table 7.1: Rate (Hz) of amount of experimental data kept after each direct cut. The remaining percentage of simulated-signal after each direct cut is exposed as well. The experimental data correspond to a single run with the Id number: 120630, and the data was collected the 3rd of October of 2012. The total rate of the experimental IceCube data InIce at Level2 is 746 [Hz]. The simulated data corresponds to a 2012 dataset with the Id number 11069 [150].

Until this point we have reduced the IceCube experimental data to 10.97 [Hz] while keeping 80 % of the Up-Going NuMu-CC signal weighted as $\frac{d\Phi_\nu}{dE} \propto E^{-2}$. This allows us now to process a more precise reconstruction that will be “passed” to the BDT and will provide a good angular resolution in the final part of this IceCube analysis. This high-level reconstruction is SplineReco with energy estimator (SplineEnEst), as explained in section 5.4.1.

On our sample of 10.97 Hz for experimental data, we run SplineEnEst, where the track angular seed is MPEFit, and the one that gives the energy reconstruction is MPEFitMuEX. Once SplineEnEst is available in our data, a direct cut on the reconstructed zenith provided for the SplineEnEst is applied to define a pre-BDT level. This cut rejects events with a reconstructed zenith smaller than 90° , which means tracks reconstructed to be emitted from the Southern sky. With this cut, the rate of 10.97 Hz is reduced to 8 Hz.

7.2.1 BDT Performance in the Alternative Event Selection

After having obtained an amount of data of ~ 8 Hz via direct cuts, we discriminate signal from background using BDT. The BDT variables that I have used in the alternative event selection are described below.

- LineFit-Velocity: See description in Chapter 5.
- ZTravel: This gives an indication of the travel direction and track length in the vertical coordinate, which is defined as:

$$zTravel = \frac{1}{NHitDoms} \sum_{doms} (Z_{dom_i} - \bar{Z}), \quad (7.4)$$

where Z_{dom_i} is the position of each fired dom, and \bar{Z} is the average of the position of the fired DOMs in the first quartile in time. This quantity is calculated by the HitStatistics module that is part of the CommonVariable project.

- RLogL-SplineReco: explained in the previous section.
- NDirPulses: explained in the previous section.
- DirTrackLength: explained in the previous section.
- EmptyHitsTrackLength: explained in the previous section.

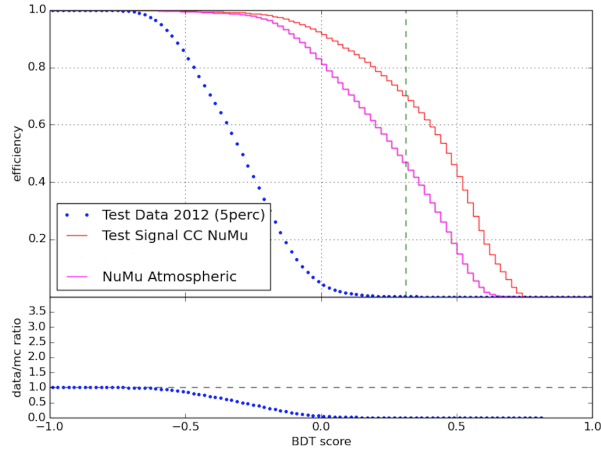
- AvgDomDistQTotDom: explained in the previous section.
- TrackHitsSeparationLength: explained in the previous section.

As indicated above, the BDT allows us to discriminate signal from background, which is performed by what is called the *BDT-Score*. Fig. 7.5 shows the distribution of simulated signal, simulated atmospheric neutrino and experimental data that is kept as a function of the BDT-Score (horizontal axis). In combination with the results displayed in fig. 7.5, fig. 7.6 shows the rate (Hertz) of experimental data and atmospheric neutrinos. The red curve shows the signal distribution, however the signal curve does not reflect a realistic rate, since this has been included just to illustrate the fraction of simulated neutrino signal kept at certain BDT-Score. Note that experimental data contains events that are produced by atmospheric muons, atmospheric neutrinos and possibly astrophysical neutrinos.

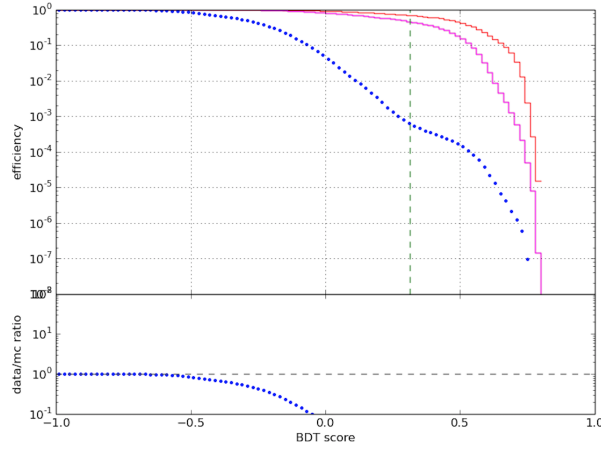
In both figures, 7.5 and 7.6, a vertical dashed line is displayed. This line indicates a suggested BDT-Score threshold that discriminates signal from background under certain conditions. As previously explained, we want to obtain an atmospheric neutrino level, therefore, this condition is constrained to the amount of atmospheric neutrinos that is requested to remain in our experimental data. In this event selection, this condition is defined as: 60% of our experimental data is dominated by NuMu atmospheric neutrinos. This condition yields a suggested BDT-Score threshold of 0.3. The value is also called BDT-Cut, where all the events with a BDT-Score below this value are thrown away, since they have atmospheric muon features.

In fig. 7.6, we can observe that when we move to larger values in the BDT-Score, the simulated atmospheric neutrino rate tends to follow our experimental data rate. Nevertheless, a small discrepancy remains due to the fact that the atmospheric neutrino simulation is based on NuMu events, whereas in our experimental data also a small fraction of electron neutrinos might be present.

The BDT-Cut here is a suggested BDT-Score based on the requirement that 60% of the experimental data is composed on atmospheric NuMu's. Nevertheless, we aim to obtain experimental data optimized for detecting astrophysical neutrinos from our selected sources. The latter can be obtained through the calculation of the discovery potential.



(a) Efficiency (vertical axes) for simulated neutrino signal, atmospheric neutrino and experimental background at different BDT-Cuts.



(b) Efficiency in power of ten scale for simulated neutrino signal, atmospheric neutrino and experimental background at different BDT-Cuts.

Figure 7.5: The vertical axes shows, amount of signal, simulated atmospheric neutrinos, and experimental background as a function of the BDT score. The efficiency is defined as the ratio between the number of events after a certain BDT-Cut, over the initial amount of events.

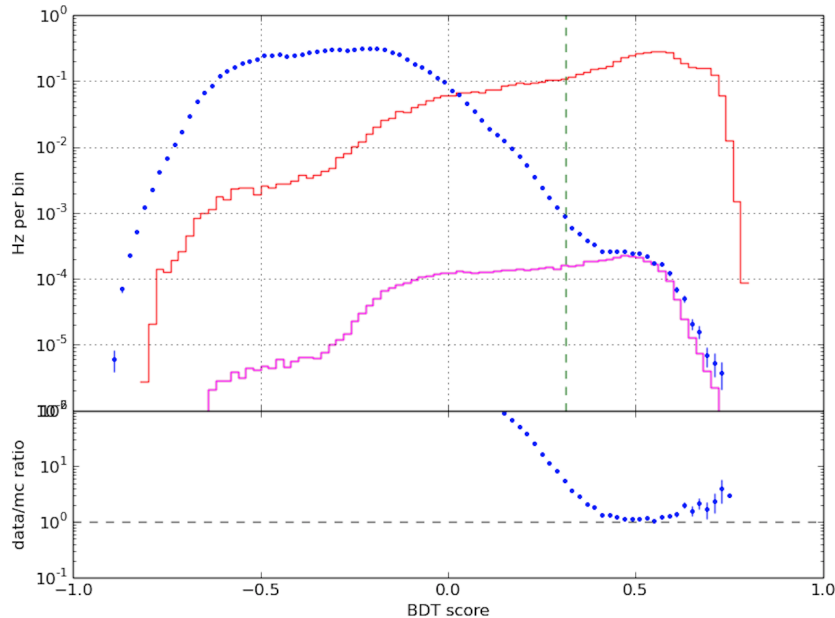


Figure 7.6: BDT score distribution performance when the background is experimental data (blue points) vs NuGen simulated E^{-2} signal (red curve). The figure also shows the NuMu atmospheric neutrino curve (magenta curve). The dashed green vertical line indicates at what BDT score one has to cut in order to obtain an experimental data set dominated by 60% of NuMu atmospheric neutrinos. That BDT score corresponds to: 0.3.

7.2.2 Event Selection Results in terms of the Discovery Potential

To determine the discovery potential, the uncertainty on the direction of the reconstructed track has to be determined, which is obtained by Paraboloid already introduced in section 5.4.2. Nevertheless, in the data used for this analysis, Paraboloid for the SplineEnEst is not available in our data sets. To include Paraboloid in our data sets, is an “expensive” task from the point of view of the CPU computing time. It follows that a data reduction is needed in order to run Paraboloid in a relatively short amount of time. This data reduction is achieved through a “mild” BDT-Cut=0.15, which is a conservative cut compared with the one suggested for the BDT-Score (=0.3). So, we could ensure that with this cut there is basically no signal removal.

Subsequently to the BDT-Cut=0.15, we select a BDT-Score such that we obtain the best discovery potential. The discovery potential is obtained by injecting N times a certain number of signal events, such that in 50% of the times we obtain a test statistic larger than the 5σ threshold value of the background distribution as explained in Chapter 6.3. A background distribution for each object in the Obscured Flat Spectrum Radio AGN population is presented in appendix D. The manner of injecting simulated signal events can be illustrated in the following way. Let us imagine a two dimensional gaussian distribution, in right ascension and declination, which is centered at the source position in the sky. From this distribution, we randomly collect certain number of signal tracks, and we include them in the Likelihood. We repeat this procedure until we reach in 50% of the times a test statistic larger or equal than the threshold indicated previously.

The best discovery potential, so the minimum value of the signal strength to obtain a 5 sigma significance, is determined by varying the BDT-Score. This is performed individually for each object in the Obscured Flat Spectrum Radio AGN sample. The reason for this is the fact that the track reconstruction and the BDT variables have different performance according to the zenith angle. To demonstrate this fact, fig. 7.7 shows the angular resolution per zenith bin, for different energy ranges. This clearly exposes that the performance of an angular reconstruction depends of the zenith angle of the track, and consequently of the declination where we look at. Moreover, this figure also shows that the angular reconstruction loses accuracy for low energy neutrinos, since low energy tracks illuminate fewer DOMs.

To illustrate how the discovery potential varies according to the BDT-Score, two examples are shown in fig. 7.8. These plots correspond to two objects in the Obscured Flat Spectrum Radio AGN population. One clearly sees that the best discovery potentials are achieved when a cut on BDT is applied at 0.38 for the galaxy $4C + 04.77_{\delta=4.4^\circ}$, and at 0.41 for the galaxy $3C371_{\delta=69.82^\circ}$. The results of the best discovery potentials, with the corresponding cuts for the BDT-Score, are exposed in table 7.2 for the entire list of objects in the Obscured Flat Spectrum Radio AGN population.

7.3 Comparison between the Alternative Sample and the Standard Point Source Sample.

Based on the determination of the discovery potential for each individual object in the Obscured Flat Spectrum Radio AGN population, we want to compare our values with the ones obtained with the standard Point Source

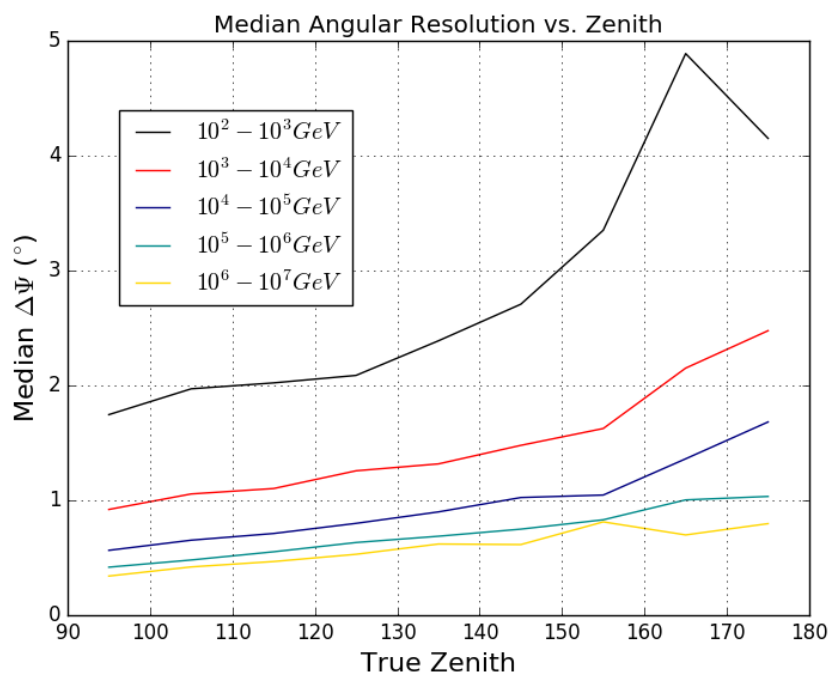
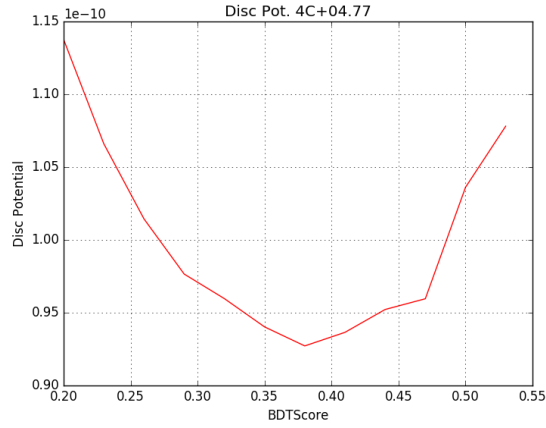
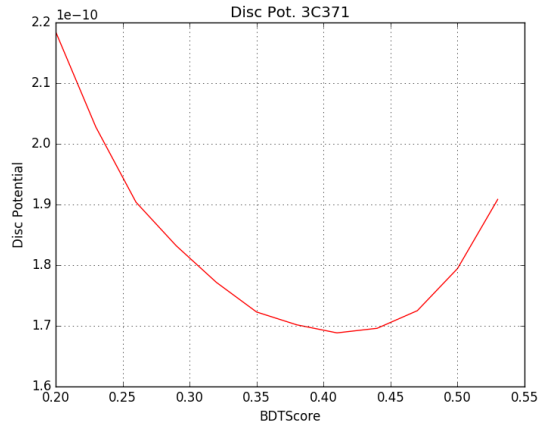


Figure 7.7: Track resolution as a function of the zenith angle for several energy ranges.



(a) Discovery potential vs BDT score cut for the galaxy 4C+04.77, located at $\delta = 4.4^\circ$. The best discovery potential is achieved when a BDT-Cut is set at 0.38.



(b) Discovery potential vs BDT score cut for the galaxy 3C371, located at $\delta = 69.82^\circ$.

Figure 7.8: Discovery potential ($[TeV\ cm^{-2}s^{-1}]$) performance for different BDT score cuts. Each plot corresponds to a single source in the Obscured Flat Spectrum Radio AGN population.

Source	δ	$E^2 \frac{d\Phi}{dE_\nu}^{5\sigma,50\%}$	$E^2 \frac{d\Phi}{dE_\nu}^{90\%}$	BDT-Cut
1H1720+117	11.87	9.552e-11	3.988e-11	0.41
2MASXJ05581173+5328180	53.47	1.348e-10	6.216e-11	0.41
3C371	69.82	1.688e-10	7.604e-11	0.41
4C+04.77	4.667	9.271e-11	3.842e-11	0.38
ARP220	23.50	1.045e-10	4.353e-11	0.44
B21811+31	31.73	1.113e-10	5.150e-11	0.47
CGCG186-048	35.01	1.164e-10	5.536e-11	0.47
GB6J1542+6129	61.49	1.487e-10	7.950e-11	0.5
MRK0668	28.45	1.051e-10	4.794e-11	0.47
NGC3628	13.58	9.451e-11	3.973e-11	0.41
PKS1717+177	17.75	9.881e-11	5.183e-11	0.53
RGBJ1534+372	37.26	1.197e-10	5.719e-11	0.47
SBS0812-578	57.65	1.369e-10	7.796e-11	0.5
SBS1200+608	60.52	1.441e-10	7.871e-11	0.5

Table 7.2: Final BDT-Score cut (BDT-Cut) for each source in the Obscured Flat Spectrum Radio AGN population. This was optimized according to the best discovery potential ($[\text{TeV cm}^{-2}\text{s}^{-1}]$) calculation. Furthermore, the declination δ (in degrees) of the source and the Sensitivity ($[\text{TeV cm}^{-2}\text{s}^{-1}]$) are shown.

Data Type	Season	Amount of data
Experimental	5% of 2012	46 runs, 15 days of data
NuMu Sim	2012, DataSet 11069	2876 (PS), 2310 (This) files

Table 7.3: Data Set used to obtain the results that are presented in fig. 7.9. The NuMu simulation data set is used as: E^{-2} spectrum. PS means Point Source, and “This” indicates the alternative event selection .

sample. This is done in order to have a complete overview of both data sets, and hence, make use of the best one for investigating the Obscured Flat Spectrum Radio AGN population in the IceCube neutrino observatory.

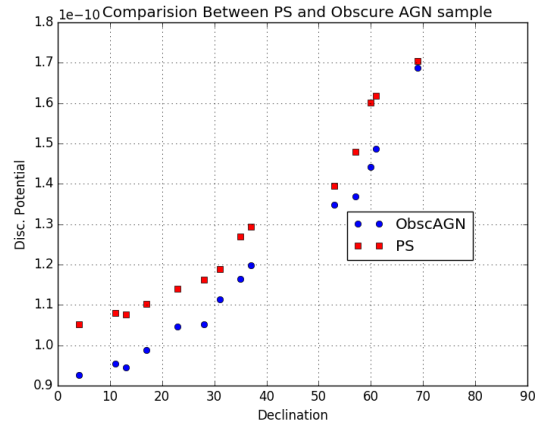
The standard Point Source sample is already at the atmospheric neutrino level, so there is no need to apply further selection procedures on this data set. The comparison was made considering the data set exposed in table 7.3, and the results are presented in fig. 7.9. This figure shows that the discovery potential obtained with the alternative event selection (blue points) yields an improvement of $\sim 10\%$ with respect to the Point Source sample (red points), mainly for sources at lowest declination.

Observing the results displayed in fig. 7.9, we want to understand what causes the difference. The discovery potential involves 2 main observables, effective area and angular resolution, where the effective area is defined as,

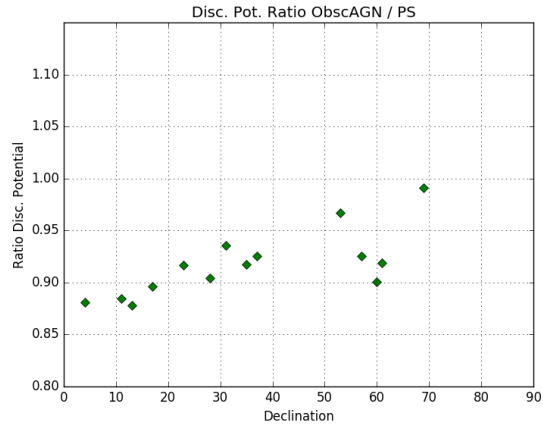
$$A_{eff} = \frac{\text{ObservedEventRate}}{\text{IncomingFlux}} \quad (7.5)$$

The ratio of the effective areas, obtained with the alternative event selection sample and the standard Point Source sample is displayed in fig. 7.10. This figure shows that the alternative event selection sample in general has a lower effective area than the one obtained with the standard Point Source Sample. This result can be attributed to the manner how the event selection was performed in both samples, which includes direct cuts and the BDT variables used.

On the other hand, the angular resolution is presented in fig. 7.11 and 7.12. Here, one can see that the angular resolution in the alternative event selection sample is better than in the case of the standard Point Source sample. As explained above, SplineReco with Energy Estimator was used in the alternative event selection , whereas SplineReco without Energy Estimator is used in the standard Point Source sample.



(a) The discovery potential obtained with the standard Point Source Sample (red squares) vs the one obtained with the alternative event selection (blue circles).



(b) Ratio between the discovery potential obtained with the standard Point Source sample and the alternative event selection, as a function of the declination of each Obscured Flat Spectrum Radio AGN.

Figure 7.9: Comparison between the discovery potential ($[TeV\ cm^{-2}s^{-1}]$) given by the alternative event selection sample and the IceCube standard Point Source sample. Each point represents a source in the Obscured Flat Spectrum Radio AGN population.

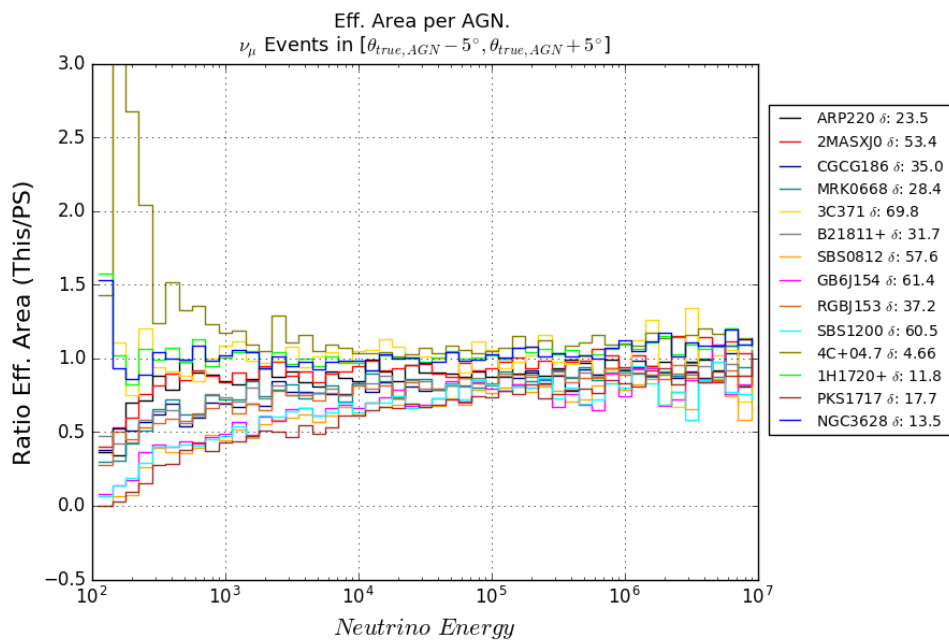


Figure 7.10: Ratio between the effective are obtained with the alternative event selection , vs the standard Point Source Sample. This shows that the alternative event selection in general reflects a lower effective area.

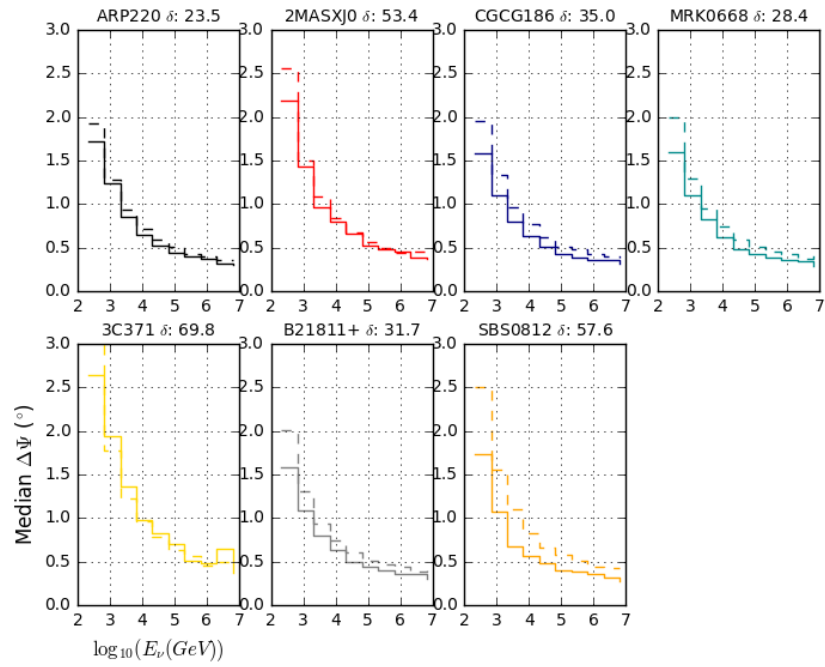


Figure 7.11: Median angular resolution as a function of the true energy for the standard point source sample (dashed lines) and the alternative event selection (solid lines). This is calculated for each individual object in the Obscured Flat Spectrum Radio AGN sample. The events used for each plot are the ones for which the primary neutrino direction falls into a True-zenith band of 5° around the source.

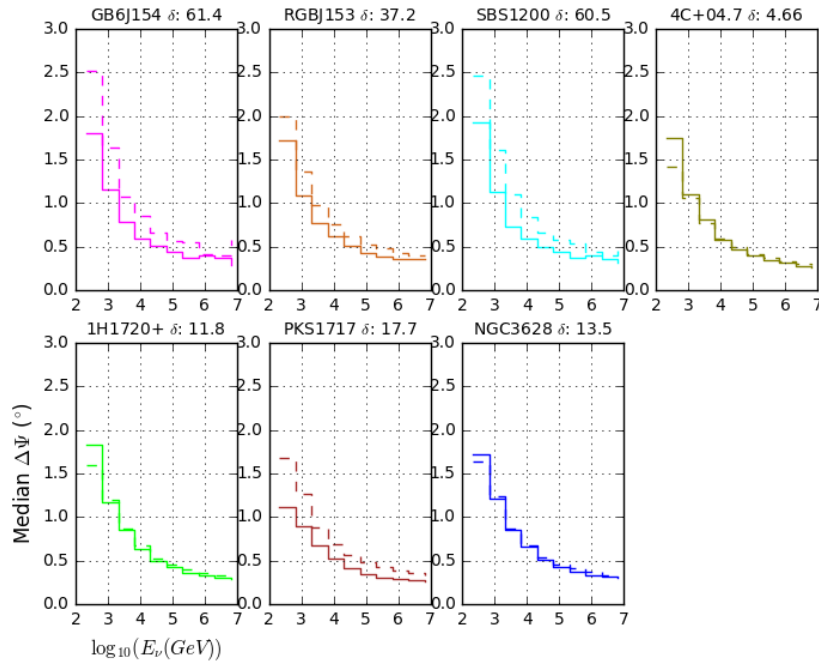


Figure 7.12: Complement of fig. 7.11, for the left seven object in the Obscured Flat Spectrum Radio AGN population. Median angular resolution as a function of the true energy for the standard point source sample (dashed lines) and the alternative event selection (solid lines). This is calculated for each individual object in the Obscured Flat Spectrum Radio AGN sample. The events used for each plot are the ones for which the primary neutrino direction falls into a True-zenith band of 5° around the source.

7.4 The Final Sample for this Analysis, “The Re-processed Point Source Sample”

So far, we can state that the event selection developed for this analysis (the alternative event selection) gives a better discovery potential than the standard Point Source one, which is due to an improvement on the angular resolution. However, the standard Point Source event selection results in a larger effective area. In order to profit from both, the improved angular resolution of the alternative event selection and the better effective area of the standard Point Source sample, a new approach will be followed to obtain the final event sample. This new approach is based on running the SplineReco with Energy Estimator on the standard Point Source sample.

So, on the standard Point Source sample that is already at the atmospheric neutrino level, and contains events from the full sky, we process SplineEnEst. The median angular resolution obtained with SplineEnEst as used in this analysis, is displayed in fig. 7.13³. The resolution for lowest declination δ presents a better performance, since the track is close to the horizon, and consequently crosses more strings of the detector. At the highest declination the track could be misreconstructed as a vertical track, whereas actually it is a track with a small inclination with respect to the strings.

On this event sample, we make a cut on the zenith angle as reconstructed by SplineEnEst, which rejects events with a zenith smaller than 85° . This selection is firstly applied in order to reject tracks coming from the southern hemisphere, which are not considered since the investigated Obscured Flat Spectrum Radio AGN are located in the Northern Sky. Secondly, it is used to speed up the computation of the uncertainty estimator (Paraboloid), and also to be consistent with the definition of the Point Source working group with the data set to study objects in the Northern sky.

We also present the IceCube effective area for this analysis, which is shown in fig. 7.14. This clearly shows that the effective area increases at highest energy, due to the fact that the probability that a neutrino interacts in the IceCube detector increases with the energy. Nevertheless, at highest declination and highest energy the effective area is reduced due to Earth’s

³Notice that the energy estimator used in the settings for SplineEnEst in fig. 7.13, and figures 7.11 and 7.12, are different. The energy estimator to produce the median angular resolution in fig. 7.13 is based on a high level algorithm, which consumes more CPU time, and is only available at the final level of the standard Point Source sample. Whereas the energy estimator used in SplineEnEst as displayed in figures 7.11 and 7.12 is available at Level3.

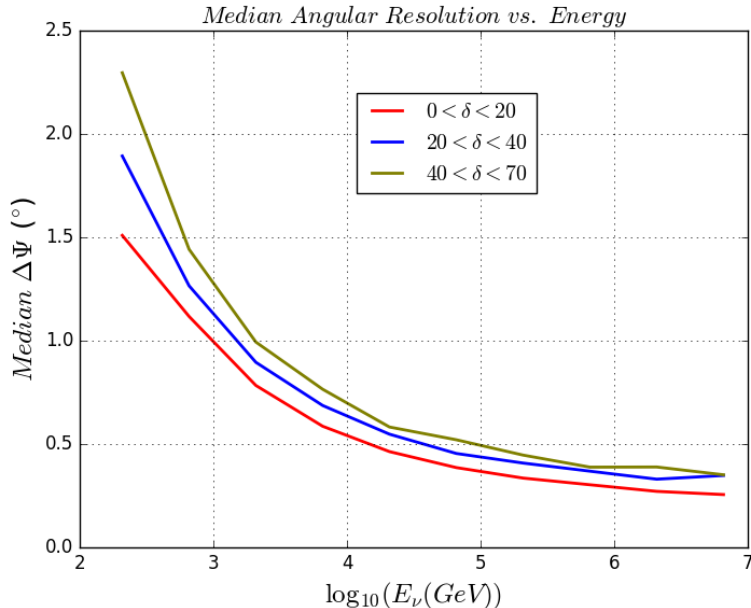


Figure 7.13: Median angular (NuMu-CC) resolution obtained with Splin-eEnEst, as used for the current analysis. The declination ranges used here cover the entire position in the sky of sources in the Obscured Flat Spectrum Radio AGN population. This plot was made using the IceCube simulation dataset 11069.

absorption

Fig. 7.15 shows the comparison between the discovery potentials obtained with the standard Point Source, the Reprocessed Point Source (PSRepro) and the alternative event selection (labeled with “this”). This clearly shows that the sample that provides the best discovery potential is the Reprocessed Point Source sample.

Due to the improvement in the discovery potential observed in the PSRepro, I reprocessed four years of data of this sample in view of this and future analysis. As a sanity check, we show in fig. 7.16 the reconstructed zenith for the four years of the PSRepro sample. This figures exposes by itself that the 4 years of data look “sane”. In table 7.4, we present further information about these four years of data, being the number of runs, number of events, lifetime and rate.

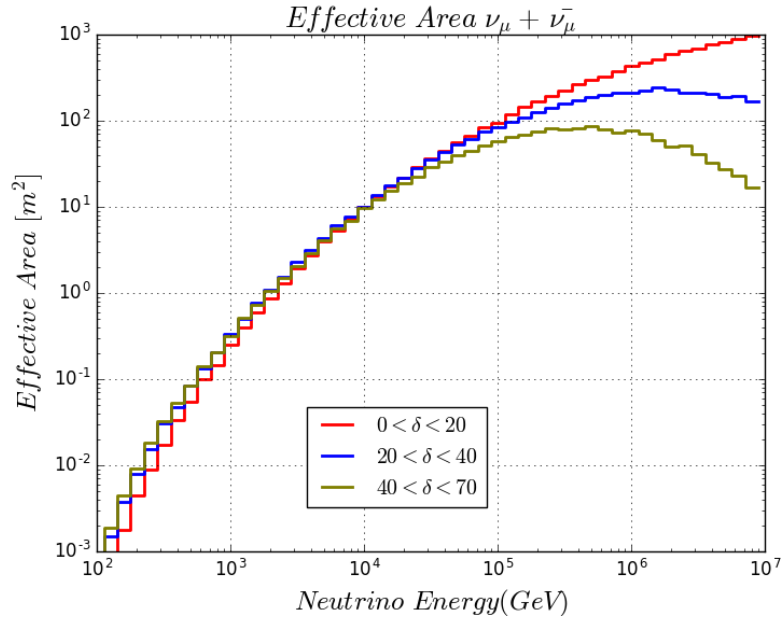
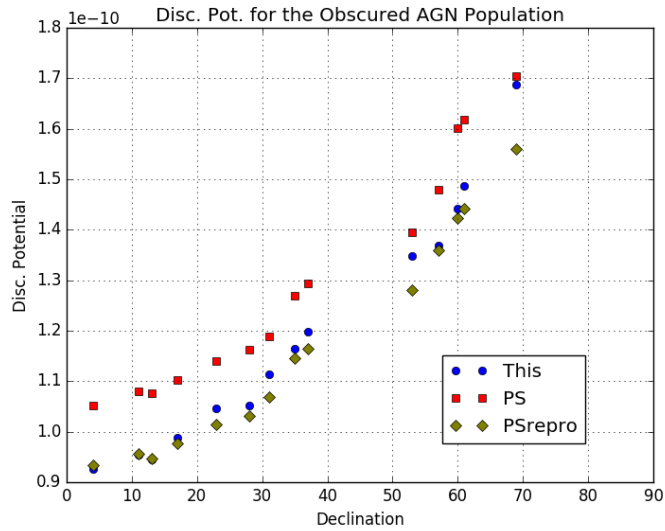


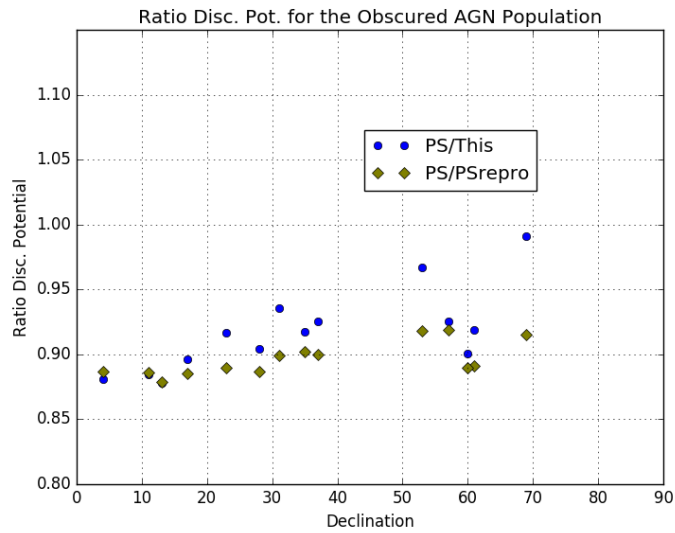
Figure 7.14: NuMu effective area in the IceCube neutrino observatory. The declination ranges used here cover the entire location in the sky of sources in the Obscured Flat Spectrum Radio AGN population. This plot was made using the IceCube simulation dataset 11069.

Year	N Runs	N Events	Lifetime (days)	Rate [mHz]
2012	1169	73493	331.4	2.56
2013	1459	79764	359.7	2.56
2014	1288	80765	360.9	2.59
2015	1296	81617	362.7	2.60

Table 7.4: Information about the Reprocessed Point Source Sample.



(a) The discovery potential obtained with the Point Source, the Reprocessed Point Source and the alternative event selection .



(b) Ratio between the discovery potential obtained with the standard Point Source Sample vs the alternative event selection , plotted against the declination of each Obscured Flat Spectrum Radio AGN.

Figure 7.15: Comparison of discovery potential ($[\text{TeV cm}^{-2}\text{s}^{-1}]$) obtained with the standard Point Source, the Reprocessed Point Source and the alternative event selection .

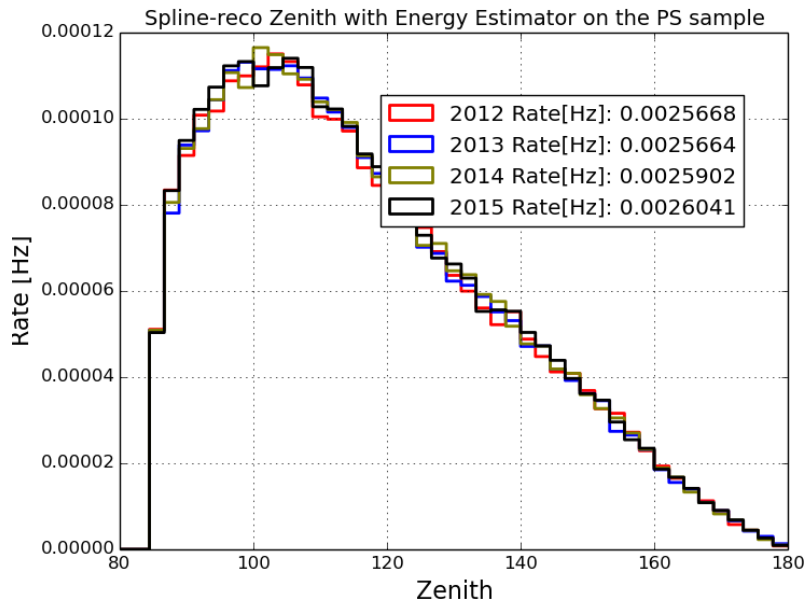


Figure 7.16: Zenith distribution for four years of data of the reprocessed Point Source sample.

Chapter 8

Results and Discussion

Part of the work developed in this PhD thesis includes an AGN selection based on radio and X -ray observations. These AGN are called Obscured Flat Spectrum Radio AGN. This study has been motivated by the fact that no high-energy neutrinos have been observed from the already investigated astrophysical objects, which have relied on the fact that the brightest objects in the sky (as certain subclasses of AGN), might be neutrino sources. In the current work, based on multimessenger arguments, we propose an alternative model of neutrino production in AGN that are obscured instead of bright. These objects are also known as *hidden cosmic-ray accelerators*. In total, 16 objects have been selected as possible sources of high-energy neutrinos, from which 14 sources are in the Northern sky.

These 14 objects were investigated, as part of this PhD work, with data of the IceCube neutrino observatory at the South Pole. The IceCube analysis performed in the current work ended up with an improvement on the discovery potential of about $\sim 10\%$ with respect to previous data samples in IceCube. As indicated in table 7.4, four years of data (2012-2015) of the full IceCube detector (86 strings) were reprocessed, and subsequently analyzed. The total number of events corresponds to 315639, with a lifetime of 1414.7 days, which implies a full rate of ~ 2.58 mHz.

From the search for high-energy neutrinos from obscured flat spectrum radio AGN using the IceCube neutrino observatory, we have set a 90% upper limit $\Phi^{90\%}$ on the neutrino flux ($\nu_\mu + \bar{\nu}_\mu$) expected from each source in the AGN sample, these upper limits are displayed in table 8.1. This was obtained considering a power-law of $\frac{d\Phi_\nu}{dE} \propto E^{-2}$. Furthermore, in table 8.1, we present the pre-trial p-values ¹, γ_ν and number of signal n_s as provided by the

¹A p-value for each source is calculated by minimizing only once the Likelihood for-

Source name	ra	δ	\mathcal{TS}	p-val	n_s	γ_ν	$\Phi^{90\%}$
1H1720+117	261.27	11.87	0.0	1.0	0.0	3.11	6.95E-13
2MASX	89.55	53.47	3.63	0.037	16.12	2.73	1.08E-12
3C371	271.71	69.82	0.82	0.242	5.35	4.0	1.18E-12
4C+04.77	331.07	4.67	0.12	0.412	0.73	2.05	6.50E-13
ARP220	233.74	23.50	0.0	1.0	0.0	4.0	7.46E-13
B21811+31	273.40	31.74	2.51	0.076	11.93	2.85	8.50E-13
CGCG186-048	176.84	35.02	0.0	1.0	0.0	2.88	8.56E-13
GB6J1542+6129	235.74	61.50	0.0	1.0	0.0	2.68	1.07E-12
MRK0668	211.75	28.45	0.24	0.300	2.48	3.76	8.79E-13
NGC3628	170.07	13.59	3.93	0.034	6.88	2.21	7.19E-13
PKS1717+177	259.80	17.75	1.44	0.142	7.81	2.97	7.54E-13
RGBJ1534+372	233.70	37.27	0.30	0.318	3.95	3.05	8.99E-13
SBS0812-578	124.09	57.65	0.11	0.386	1.70	3.84	1.09E-12
SBS1200+608	180.76	60.52	0.0	1.0	0.0	2.46	1.09E-12

Table 8.1: List of sources in the AGN population and the their position (ra, δ) in Equatorial coordinates in degrees. The following values correspond to the fit result that are obtained by maximizing the Likelihood formula. Here we show the test statistic value \mathcal{TS} , the pre-trial p-value, the number of signal-like events n_s and the spectral index γ_ν . The upper limit, within the energy range of 1 TeV - 1 PeV, on the $\nu_\mu + \bar{\nu}_\mu$ flux $\Phi^{90\%}$ is given in units of [$\text{TeV cm}^{-2}\text{s}^{-1}$]. The name 2MASX refers to 2MASXJ05581173+5328180.

minimization of the Likelihood formula, as well as the position (declination δ and right ascension ra) of each source. The test statistic background distribution for each individual Obscured Flat Spectrum Radio AGN, from which we have determined the sensitivity (at 90% of signal above the median of the background distribution as explained in Chapter 6), is presented in Appendix D.

As shown in table 8.1, the two most significant pre-trial p-values are

mula $\mathcal{L}(n_s, \gamma_\nu)$ for non-scrambled data at the source position. Subsequently, a single \mathcal{TS} is computed. Hence, once this \mathcal{TS} is obtained, the pre-trial p-value is given by p-value = $\int_{\mathcal{TS}}^{\infty} \text{FitPDF}_{backg}$, where FitPDF_{backg} is the fitted background probability density function as given in Appendix D. Notice that the smaller the p-value is, the less compatible the observation is with background only.

0.034 and 0.037, which correspond to the objects NGC3628 and 2MASXJ05581173+5328180 respectively. From the pre-trial p-values, we can estimate the post-trial p-value \mathcal{P} according to the number of observations that we used to analyze our data (or number of times that “we look at the sky”), which in our case amounts to 14. This post-trial p-value is given by the Binomial Distribution defined as:

$$\mathcal{P}_p^{14}(k) = \binom{14}{k} p^k (1-p)^{14-k}, k = 0, 1, \dots, 14 \quad (8.1)$$

So, the post-trial p-value \mathcal{P} considering our two (hence, $k = 2$ in eq. 8.1) most significant objects and the more conservative pre-trial p-value ($p = 0.037$) is $\mathcal{P} = 0.08$. Since this is compatible with background, we can not claim the observation of a signal and consequently we have provided the flux upper limits as reflected in table 8.1.

Systematic Errors

The systematic errors in this analysis are reflected by the uncertainties in the obtained neutrino flux ($\nu_\mu + \bar{\nu}_\mu$), which are propagated in the sensitivity and discovery potential calculation [119]. The influence of various systematic effects has been investigated by means of different simulated data sets in which various parameters were stretched within reasonable limits. The main uncertainty corresponds to the DOM efficiency on recording the light. A variation of $\pm 10\%$ on this optical efficiency produces a neutrino flux uncertainty of $\sigma_{OptEff} = 7.5\%$ [163]. On the other hand, the ice properties, as the absorption length of the photons, produces a $\sigma_{AbsLenght} = 5.6\%$ of uncertainty on the flux by varying the absorption length by 10% [164]. Another uncertainty is the photo-nuclear cross section when a muon interacts with a nucleon in ice, which amounts to $\sigma_{xsec,\gamma-N} = 5.9\%$ [165]. Therefore, the total systematic uncertainty in the simulated neutrino flux is,

$$\sigma_{systematic} = \sqrt{\sigma_{OptEff}^2 + \sigma_{AbsLenght}^2 + \sigma_{xsec,\gamma-N}^2} = 11\% \quad (8.2)$$

Discussion of the Upper Limits $\Phi^{90\%}$.

In table 8.1, the upper limits obtained from the Obscured Flat Spectrum Radio AGN investigation using the IceCube detector are presented. These upper limits represent the maximum flux at 90% confidence level that each source can emit to be compatible with the observations of the IceCube neutrino observatory using four years of data. A possible resulting diffuse neutrino flux can be related to such an upper limit by considering the source density in the Universe of the investigated categories (FSRQ, ULIRG and BL Lac). The observed diffuse neutrino flux measured by IceCube, amounts to $\Phi_{\nu}^{dif} = (0.95 \pm 0.3) \cdot 10^{-11} \text{ TeV cm}^{-2} \text{ s}^{-1} \text{ sr}^{-1}$ [166].

One can compare the upper limits obtained in this work, to the neutrino flux that one would expect for a single source at a distance d , under the assumption that its source class is responsible for 100% of the diffuse astrophysical flux detected by IceCube. Assuming that all sources in this class, with a source density \mathcal{H}_0 , emit isotropically at a similar rate, this flux is obtained by [167],

$$\Phi_{\nu}^{rep-obj} = \frac{(0.9 \pm 0.3) \cdot 10^{-12} \text{ TeV}}{\xi_{z,2.4} \mathcal{H}_{0,-5} d_1^2 \text{ cm}^2 \text{ s}}, \quad (8.3)$$

where $\mathcal{H}_0 = \mathcal{H}_{0,-5} 10^{-5} \text{ Mpc}^{-3}$ is the local source density, and $d = d_1 10 \text{ Mpc}$. The quantity $\xi_{z,2.4}$ is a dimensionless parameter, which is related to the redshift evolution of the source ξ_z , via $\xi_{z,2.4} = \xi_z/2.4$ [167]. The factor in the numerator includes the diffuse astrophysical neutrino flux as measured by the IceCube Collaboration [166], as explained in [167]. Note that since this expression only contains the diffuse astrophysical neutrino flux, no implicit assumptions on the neutrino emission model, for example if the emission is lead by pp or $p\gamma$ interactions, are included to obtain these results.

Hereafter, I will show the value $\Phi_{\nu}^{rep-obj}$ for the two most significant objects in table 8.1. Here we also indicate the efficiency parameter η , which reflects up to which percentage the given source class can be responsible for the diffuse astrophysical neutrino flux, under the assumption that all the sources in this class emit isotropically at an equal rate.

As presented in table 8.2, for the object 2MASXJ05581173+5328180 belonging to the FSRQ class we obtain $\eta = 0.388$. It follows that FRSQ objects can only contribute to roughly 39% of the diffuse neutrino flux, under the assumption that 2MASXJ05581173+5328180 is representative for the FSRQ class. On the other hand, for the object NGC 3628 that belongs to the ULIRG class, we find $\eta = 55.4$, and hence ULIRGs can still account for the

Source	$\mathcal{H}_0 \text{ Mpc}^{-3}$	ξ_z	$d \text{ Mpc}$	$\Phi_\nu^{rep-obj}$	$\Phi^{90\%}$	η
NGC 3628	$5 \cdot 10^{-4}$	2.4	12	0.013	0.72	55.4
2MASX	10^{-9}	3.6	147.6	2.78	1.08	0.388

Table 8.2: Information to obtain $\Phi_\nu^{rep-obj}$ as in eq. 8.3. The source density \mathcal{H}_0 for FSRQ, to which the 2MASXJ05581173+5328180 object belongs, and the ξ_z parameter have been obtained from [167]. The source density for starforming galaxies, to which the NGC 3628 galaxy belongs according to the radio catalog [120], is obtained from [168]. The abbreviation 2MASX refers to the object 2MASXJ05581173+5328180. Fluxes in units of $10^{-12} \frac{\text{TeV}}{\text{cm}^2 \text{ s}}$.

diffuse astrophysical neutrino flux. One way to overcome these constraints, could be by assuming that not all objects emit at the same rate, or that the emission is not isotropic. This can be illustrated, for example, by considering a beamed neutrino emission. In this case, objects with a jet pointing towards us can be treated as a single category, which could be decoupled from the ones that have a jet pointing away from Earth. Furthermore, obscured objects could be treated as a different category, since the matter in our line of sight could produce a different neutrino rate as a consequence of the pp interactions.

Summary

Several studies predict the emission of high-energy neutrinos from astrophysical objects. These predictions have only recently been proven by the IceCube Collaboration, which in 2013 reported the first evidence for high-energy extraterrestrial neutrinos at the IceCube neutrino observatory. Nevertheless, the progenitors of these neutrinos have not been identified.

Several astrophysical sources have been investigated in order to find the origin of the high-energy neutrinos observed by IceCube. These investigations have been mainly focused on Gamma Ray Bursts (GRBs) and Active Galactic Nuclei (AGN) with strong emission at the highest frequencies of the electromagnetic spectrum. Nevertheless, so far, there are no indications that can prove that the investigated objects are indeed neutrino emitters.

Due to the fact that there is no clue about the origin of the astrophysical neutrinos, in this thesis we investigated an unexplored class of AGN in neutrino astronomy. This class of AGN is characterized by a weak observed flux at highest energies of the electromagnetic emission, and a radio jet pointing towards us. Therefore, we selected a sample of AGN based on radio and X -ray observations, called Obscured Flat Spectrum Radio AGN. Radio and X -ray photons play the role of multi messengers, where radio observations indicate that particle acceleration takes place at the source, and the relativistic jet (which may contain hadrons) points towards us. On the other hand, a suppressed X -ray flux reveals the presence of obscuring material in our line of sight. Consequently, the obscuring material plays the role of a hadronic beam dump, such that the hadronic interactions can produce mesons and subsequently neutrinos.

From the selected Obscured Flat Spectrum Radio AGN, 14 objects in the Northern sky have been investigated during this PhD work. This has been done using data and resources of the IceCube neutrino observatory at the South Pole. The IceCube data analysis effort mainly consisted of attempting to improve the discovery potential obtained with previous data samples at IceCube. This goal was indeed achieved, and the improvement

on the discovery potential amounts to $\sim 10\%$.

The IceCube results of the Obscured AGN analysis obtained by analyzing 4 years of data (2012-2015), indicate that there is no evidence that allows us to claim an observation of high-energy neutrino emission from any of the 14 investigated objects in the Obscured Flat Spectrum Radio AGN population. In this analysis, the two objects that show the largest significances according to their pre-trial p-values are the galaxies NGC3628 and 2MASXJ05581173+5328180. These two objects fall into the category of FSRQ-ULIRG, as explained in Chapter 4. This might favor FSRQ-ULIRG objects as possible neutrino emitters against BLLac objects, which differ on the fact that the FSRQ objects show X -ray from both the accretion disc and the jet, whereas BLLac typically show emission from the jet. The physical property that causes the contrast in the electromagnetic emission of FSRQ-ULIRG vs BLLac, might also be the responsible of a possible difference in the neutrino emission.

The upper limit for the NGC 3628 object indicates that ULIRGs can not be ruled out as possible astrophysical neutrino sources. As indicated above, the NGC 3628 object is classified as a starforming galaxy in the radio catalog [120], in which a high supernova rate is expected [?]. As indicated in [?], strong shocks produced by hypernovae could accelerate protons up to 10^{17} eV, which would be able to interact with matter, resulting high-energy neutrinos up to 5 PeV. However, another way to produce neutrinos in ULIRGs, could be via jet matter interaction, as in the object Arp 220, where there are indications for the presence of an AGN, which produces extra cosmic rays [125].

To conclude, in this work we have presented a first attempt to identify a new class of possible sources of high-energy astrophysical neutrinos. Analysis of the corresponding IceCube data shows no evidence for a possible signal and as such flux upper limits have been provided. However, various possible improvements have been outlined which may lead to discoveries in the future.

Service work for the IceCube Collaboration

Apart from investigating several angular reconstruction algorithms, which resulted in an improvement on the track angular reconstruction as mentioned before, during my PhD I also provided service work for the IceCube Collaboration.

This service work for the IceCube Collaboration was based on performing tasks for developing and maintaining the IceCube software (IceTray), for which I used 25% of my working time over two years. The group in charge of these kind of tasks is referred to as the “IceCube Software Strike Team”, and is composed by around 12 members.

Apart from maintaining various projects within the IceTray framework, the software tasks that demanded most of my time were related to test the performance of various IceTray modules (so called test-coverage) in two programming languages, C++ and Python. Through these kind of tests, we ensure that a certain module indeed computes correctly what it was designed for. This test-coverage task provided to me a deep knowledge about IceTray and various reconstruction techniques. Furthermore, an essential task that I coped with, was based on merging two C++ track reconstruction algorithms, LineFit and ImprovedLineFit. This merging was needed since they work together to perform a first online filtering at the South Pole IceCube data treatment. By merging these algorithms, we reduce the amount of code in our software, and we achieve a reduction on computing time. This merging was successful, and will be applied in the near future once the online filter scripts are modified.

Furthermore, another service work was to provide an event selection tool for a GRB analysis. This involved the implementation of an angular reconstruction algorithm into the IceTray framework, which could cope with coincident tracks. This reconstruction was written originally using objects in the ROOT framework, and my task was based on implementing it in IceTray framework.

Along with my participation in the IceCube Software Strike Team, I also gave several presentations about modern C++ usage for a group of IceCube members. During these presentations, I always tried to link these talks to an application in IceTray. To my opinion, the more interesting topic that I covered, is about how to “template” a C++ reconstruction algorithm in IceTray. This showed how to design such an algorithm in case it needs to handle a variety of input data.

Outlook

The physics topics covered during this PhD work involved the selection of astrophysical objects as possible neutrino sources, and the experimental analysis of these sources. With respect to the current research, those two topics could be extended in view of future investigations. First of all, a follow up of the selected sources can be accomplished, which could be based on investigating the γ -ray flux observed from the objects in the Obscured AGN population. This could be performed considering the amount of matter in the AGN environment that blocks our line of sight, which was estimated using X -ray data. Firstly, this γ -ray flux inquiry is expected to reveal that indeed the high-energy electromagnetic emission of the investigated objects is attenuated by the presence of an obscuring material. Due to the energy range of these photons, the attenuation is expected to be lead by Compton scattering and pair production (e^-e^+), instead of photo-electric absorption. Secondly, if there is hadronic acceleration at the source and those hadrons interact with a column of matter, the π^0 production would enhance the gamma-ray flux. Nonetheless, as indicated, this flux is expected to be attenuated by the same column of matter, and hence the observed flux at Earth would be enhanced at the electromagnetic frequency domain at which the attenuated γ -rays leave the AGN environment, such as InfraRed. Therefore, this increase might indicate the hadronic origin of gamma-rays from the investigated AGN.

Regarding the source investigations, the follow up of Ultra Luminosity InfraRed Galaxies (ULIRGs) could be an interesting topic in neutrino astronomy, which might be supported by the relatively small p-value found through this current IceCube analysis for the object NGC3628. ULIRGs are characterized by a high emission in the InfraRed band, which could indicate the presence of warm material in the AGN environment, and consequently neutrino production via pN interaction if hadronic acceleration takes place at the source.

Another follow up study that could be accomplished by analyzing Ob-

scured Flat Spectrum Radio AGN, is a full modeling of the neutrino production. The secondary nucleon production via $p\gamma$ and pN can be “guaranteed”, and therefore the challenge would be based on modeling the secondary nucleon interactions with the obscuring material, and the same for the full chain of daughter nucleons. This could indicate the detailed properties of the neutrino spectrum that we would expect from Obscured AGN.

In our selection of Obscured Flat Spectrum Radio AGN, there was a lack of data for studying the radio emission of the investigated AGN in the Southern sky. This was due to the fact that the Molonglo observatory in Australia detects radio emission at a single frequency. The Obscured AGN catalog in the Southern sky could be extended by exploring whether the radio emissions observed by dedicated devices covering this hemisphere would be suitable for this analysis, like for instance observations made with the ALMA radio telescope in Chile. Objects in the Southern sky could be investigated with neutrino observatories in the Northern hemisphere, like for instance the future KM3NeT neutrino observatory at the Mediterranean Sea, which is expected to have an unprecedented angular resolution in neutrino astronomy.

On the other hand, the experimental analysis could be modified in order to investigate possible improvements on the sensitivity for point source analyses in the IceCube neutrino observatory. First of all, according to the event selection presented in the current work and considering the current statistical method for point source analyses, a powerful observable that can provide an improvement in the sensitivity is the track angular resolution. This statement is due to the fact that in my alternative event selection, the discovery potential was $\sim 10\%$ better than the one obtained with the standard Point Source sample. This was achieved by a slight is due to the improvement in the angular resolution, which is enhanced in the Likelihood by the factor $\exp\left(-\frac{|\vec{x}_i - \vec{x}_s|^2}{2\sigma_i^2}\right)$.

To my opinion, a track reconstruction algorithm should be checked in every step with true Monte Carlo pulses, since this would allow to check the efficiency of the algorithm without any dependency on how the reconstructed pulses are obtained and neither the injected noise pulses. This for example, could be applied in new track reconstruction algorithms, or indeed be applied to improve the already existing reconstruction algorithms as SplineReco. After checking that the algorithm works properly with MC pulses, this obviously should be tested with reconstructed pulses.

Abbreviations

- AGN: Active Galactic Nuclei, or Active Galactic Nucleus.
- BDT: Boosted Decision Tree.
- CC: Charged Current.
- DOM: Digital Optical Module.
- FSI: Frequency Spectral Index.
- FSRQ: Flat Spectrum Radio Quasars.
- GRB: Gamma Ray Bursts.
- MC: Monte Carlo.
- NASA: National Aeronautics and Space Administration.
- NC: Neutral Current.
- NED: NASA/IPAC Extragalactic Database.
- NRAO: National Radio Astronomy Observatory.
- NuMu: Muon Neutrino.
- NVSS: NRAO VLA Sky Survey.
- PE: Photo Electron.
- PMT: Photo Multiplier Tube.
- Q_{Tot}: Total Charge in a DOM.
- UHECR: Ultra High Energy Cosmic Ray

- ULIRG: Ultra Luminosity Infrared Galaxy.
- VLA: Very Large Array.
- 1LAC: First LAT AGN Catalog.
- 2LAC: Second LAT AGN Catalog.

Bibliography

- [1] “The nobel prize in physics 1936; victor f. hess nobel lecture.” https://www.nobelprize.org/nobel_prizes/physics/laureates/1936/. The Official Web Site of The Nobel Prize.
- [2] <https://www.auger.org>. Pierre Auger Observatory WebPage.
- [3] H. Kawai *et al.*, “Telescope array experiment,” *Nuclear Physics B - Proceedings Supplements*, vol. 175, pp. 221 – 226, 2008.
- [4] A. Aab *et al.*, “Searches for Anisotropies in the Arrival Directions of the Highest Energy Cosmic Rays Detected by the Pierre Auger Observatory,” *Astrophys. J.*, vol. 804, no. 1, p. 15, 2015.
- [5] P. Tinyakov, “Latest results from the telescope array,” *Nucl. Instrum. Meth.*, vol. A742, pp. 29–34, 2014.
- [6] K. Arisaka, G. B. Gelmini, M. D. Healy, O. E. Kalashev, and J. Lee, “Composition of UHECR and the Pierre Auger Observatory Spectrum,” *JCAP*, vol. 0712, p. 002, 2007.
- [7] R. Blandford, P. Simeon, and Y. Yuan, “Cosmic Ray Origins: An Introduction,” *Nucl. Phys. Proc. Suppl.*, vol. 256-257, pp. 9–22, 2014.
- [8] J. Blümer, R. Engel, and J. R. Hörandel, “Cosmic rays from the knee to the highest energies,” *Progress in Particle and Nuclear Physics*, vol. 63, pp. 293–338, Oct. 2009.
- [9] A. Letessier-Selvon and T. Stanev, “Ultrahigh energy cosmic rays,” *Rev. Mod. Phys.*, vol. 83, pp. 907–942, Sep 2011.
- [10] K. Kotera and A. V. Olinto, “The Astrophysics of Ultrahigh-Energy Cosmic Rays,” , vol. 49, pp. 119–153, Sept. 2011.

- [11] A. Hillas, “The origin of ultra-high-energy cosmic rays,” *Annual Review of Astronomy and Astrophysics*, 1984.
- [12] E. Fermi, “On the origin of the cosmic radiation,” *Phys. Rev.*, vol. 75, pp. 1169–1174, Apr 1949.
- [13] P. Meszaros, “Gamma-Ray Bursts,” *Rept. Prog. Phys.*, vol. 69, pp. 2259–2322, 2006.
- [14] G. R. Farrar and A. Gruzinov, “Giant agn flares and cosmic ray bursts,” *The Astrophysical Journal*, vol. 693, no. 1, p. 329, 2009.
- [15] J. Bahcall and E. Waxman, “High energy astrophysical neutrinos: The upper bound is robust,” *Phys. Rev. D*, vol. 64, p. 023002, Jun 2001.
- [16] D. Guetta, D. Hooper, J. Alvarez-Muniz, F. Halzen, and E. Reuveni, “Neutrinos from individual gamma-ray bursts in the BATSE catalog,” *Astropart. Phys.*, vol. 20, pp. 429–455, 2004.
- [17] J. P. Rachen and P. Meszaros, “Cosmic rays and neutrinos from gamma-ray bursts,” *AIP Conf. Proc.*, vol. 428, p. 776, 1997.
- [18] E. Waxman, “Neutrino astronomy and gamma-ray bursts,” *Phil. Trans. Roy. Soc. Lond.*, vol. A365, p. 1323, 2007.
- [19] F. W. Stecker, C. Done, M. H. Salamon, and P. Sommers, “High-energy neutrinos from active galactic nuclei,” *Phys. Rev. Lett.*, vol. 66, pp. 2697–2700, May 1991.
- [20] M. Ahlers, M. C. Gonzalez-Garcia, and F. Halzen, “GRBs on probation: testing the UHE CR paradigm with IceCube,” *Astropart. Phys.*, vol. 35, pp. 87–94, 2011.
- [21] F. Halzen and E. Zas, “Neutrino fluxes from active galaxies: A Model independent estimate,” *Astrophys. J.*, vol. 488, pp. 669–674, 1997.
- [22] H. Netzer, *The Physics and Evolution of Active Galactic Nuclei*. 2013.
- [23] M. W. E. Smith *et al.*, “The Astrophysical Multimessenger Observatory Network (AMON),” *Astropart. Phys.*, vol. 45, pp. 56–70, 2013.
- [24] <http://baikalweb.jinr.ru>. Baikal Collaboration WebPage.
- [25] C. Perrina, “The ANTARES Neutrino Telescope,” in *Proceedings, Topical Research Meeting on Prospects in Neutrino Physics (NuPhys2014): London, UK, December 15-17, 2014*, 2015.

- [26] A. Karle, “IceCube - status and recent results,” in *Proceedings of the 15th International Workshop on Neutrino Telescopes (Neutel 2013): Venice, March 11-15, 2013*, 2014.
- [27] M. G. Aartsen *et al.*, “Evidence for High-Energy Extraterrestrial Neutrinos at the IceCube Detector,” *Science*, vol. 342, p. 1242856, 2013.
- [28] M. G. Aartsen *et al.*, “Observation of High-Energy Astrophysical Neutrinos in Three Years of IceCube Data,” *Phys. Rev. Lett.*, vol. 113, p. 101101, 2014.
- [29] Abbasi *et al.*, “An absence of neutrinos associated with cosmic-ray acceleration in γ -ray bursts,” , vol. 484, pp. 351–354, Apr. 2012.
- [30] M. G. Aartsen *et al.*, “Search for Prompt Neutrino Emission from Gamma-Ray Bursts with IceCube,” *Astrophys. J.*, vol. 805, no. 1, p. L5, 2015.
- [31] M. G. Aartsen *et al.*, “Searches for Extended and Point-like Neutrino Sources with Four Years of IceCube Data,” *Astrophys. J.*, vol. 796, no. 2, p. 109, 2014.
- [32] M. G. Aartsen *et al.*, “Searches for Time Dependent Neutrino Sources with IceCube Data from 2008 to 2012,” *Astrophys. J.*, vol. 807, no. 1, p. 46, 2015.
- [33] “The large area telescope on the fermi gamma-ray space telescope mission.” <http://fermi.gsfc.nasa.gov>. Fermi Telescope WebPage.
- [34] G. Maggi, S. Buitink, P. Correa, K. D. Vries, G. Gentile, O. Scholten, and N. van Eijndhoven, “Search for high-energy neutrinos from dust obscured Blazars,” *PoS*, vol. ICRC2015, p. 1050, 2016.
- [35] G. Maggi, S. Buitink, P. Correa, K. D. de Vries, G. Gentile, J. L. Tavares, O. Scholten, N. van Eijndhoven, M. Vereecken, and T. Winchen, “Obscured flat spectrum radio active galactic nuclei as sources of high-energy neutrinos,” *Phys. Rev.*, vol. D94, no. 10, p. 103007, 2016.
- [36] K. Murase, D. Guetta, and M. Ahlers, “Hidden Cosmic-Ray Accelerators as an Origin of TeV-PeV Cosmic Neutrinos,” *Phys. Rev. Lett.*, vol. 116, no. 7, p. 071101, 2016.
- [37] <http://www.uni.edu/morgans/astro/course/Notes/section3/new13.html>. WebPage.

- [38] A. S. Wilson and E. J. M. Colbert, “The Difference between radio - loud and radio - quiet active galaxies,” *Astrophys. J.*, vol. 438, pp. 62–71, 1995.
- [39] “Ned lectures.” https://ned.ipac.caltech.edu/level5/Glossary/Essay_fanaroff.html.
- [40] P. Padovani, “Ned lectures.” https://ned.ipac.caltech.edu/level5/Padovani2/Pad_contents.html.
- [41] S. Chandrasekhar, “The highly collapsed configurations of a stellar mass (Second paper),” *Mon. Not. Roy. Astron. Soc.*, vol. 95, pp. 207–225, 1935.
- [42] K. Schwarzschild, “Über das Gravitationsfeld eines Massenpunktes nach der Einsteinschen Theorie,” *Sitzungsberichte der Königlich Preußischen Akademie der Wissenschaften (Berlin)*, 1916, Seite 189–196, 1916.
- [43] B. P. Abbott *et al.*, “Observation of Gravitational Waves from a Binary Black Hole Merger,” *Phys. Rev. Lett.*, vol. 116, no. 6, p. 061102, 2016.
- [44] A. S. Eddington, “A limiting case in the theory of radiative equilibrium,” , vol. 85, p. 408, Mar. 1925.
- [45] D. V. S. Michael E. Peskin, *An Introduction To Quantum Field Theory*. 1995.
- [46] W. Leo, *Techniques For Nuclear And Particle Physics Experiments*. 1987.
- [47] M. Rees, “Accretion and the quasar phenomenon.” https://ned.ipac.caltech.edu/level5/Rees3/Rees_contents.html. NED WebPage.
- [48] S. Bianchi, R. Maiolino, and G. Risaliti, “AGN Obscuration and the Unified Model,” *Advances in Astronomy*, vol. 2012, p. 782030, 2012.
- [49] H. Netzer, “Revisiting the Unified Model of Active Galactic Nuclei,” , vol. 53, pp. 365–408, Aug. 2015.
- [50] R. Maiolino *et al.*, ““Comets” orbiting a black hole,” , vol. 517, p. A47, July 2010.

- [51] S. Massaglia, “Active Galactic Nuclei, Radio Jets and Acceleration of UHECRs,” *Nucl. Phys. Proc. Suppl.*, vol. 190, pp. 79–84, 2009.
- [52] <http://ned.ipac.caltech.edu>. NASA/IPAC Extragalactic Database (NED).
- [53] R. C. JENNISON and M. K. DAS GUPTA, “Fine structure of the extra-terrestrial radio source cygnus i,” *Nature*, vol. 172, pp. 996–997, 1953.
- [54] R. A. e. Perley, “The Expanded Very Large Array: A New Telescope for New Science,” , vol. 739, p. L1, Sept. 2011.
- [55] D. C. J. Bock, M. I. Large, and E. M. Sadler, “Sumss: a wide-field radio imaging survey of the southern sky. I. science goals, survey design and instrumentation,” *Astron. J.*, vol. 117, p. 1578, 1999.
- [56] “The nrao vla sky survey.” <http://www.cv.nrao.edu/nvss/>. NRAO WebPage.
- [57] T. Mauch, T. Murphy, H. J. Buttery, J. Curran, R. W. Hunstead, B. Piestrzynski, J. G. Robertson, and E. M. Sadler, “SUMSS: A wide-field radio imaging survey of the southern sky. 2. The Source catalogue,” *Mon. Not. Roy. Astron. Soc.*, vol. 342, p. 1117, 2003.
- [58] M. Imanishi, K. Nakanishi, and T. Izumi, “ALMA 0.1-0.2 arcsec Resolution Imaging of the NGC 1068 Nucleus: Compact Dense Molecular Gas Emission at the Putative AGN Location,” , vol. 822, p. L10, May 2016.
- [59] K. Nandra, “Reprocessing and the Origin of the Blue Bump in AGN,” in *Reverberation Mapping of the Broad-Line Region in Active Galactic Nuclei* (P. M. Gondhalekar, K. Horne, and B. M. Peterson, eds.), vol. 69 of *Astronomical Society of the Pacific Conference Series*, p. 273, 1994.
- [60] B. Wilkes, “Spectral energy distributions of quasars and agn.” https://ned.ipac.caltech.edu/level5/Sept03/Wilkes/Wilkes_contents.html, 2013. NED WebPage.
- [61] R. Assef *et al.*, “Mid-infrared Selection of Active Galactic Nuclei with the Wide-field Infrared Survey Explorer. II. Properties of WISE-selected Active Galactic Nuclei in the NDWFS Boötes Field,” , vol. 772, p. 26, July 2013.

- [62] S. F. Hnig, M. Kishimoto, K. R. W. Tristram, M. A. Prieto, P. Gandhi, D. Asmus, R. Antonucci, L. Burtscher, W. J. Duschl, and G. Weigelt, “Dust in the Polar Region as a Major Contributor to the Infrared Emission of Active Galactic Nuclei,” *Astrophys. J.*, vol. 771, p. 87, 2013.
- [63] <http://newhealthny.com/services/far-infrared-heat-therapy.html>. InfraRed Picture WebPage.
- [64] A. Koratkar and O. Blaes, “The ultraviolet and optical continuum emission in active galactic nuclei: The status of accretion disks,” *Publications of the Astronomical Society of the Pacific*, vol. 111, pp. 1–30, 1999.
- [65] <http://chandra.si.edu>. Chandra WebPage.
- [66] <https://www.nasa.gov/suzaku>. Suzaku WebPage.
- [67] <http://science.nasa.gov/missions/asca/>. ASCA WebPage.
- [68] <http://sci.esa.int/xmm-newton/>. XMM Newton WebPage.
- [69] <http://swift.gsfc.nasa.gov>. Swift WebPage.
- [70] <https://heasarc.gsfc.nasa.gov/docs/rosat/rosat3.html>. Rosat WebPage.
- [71] <https://www.nasa.gov>. NASA WebPage.
- [72] <http://www.esa.int/ESA>. ESA WebPage.
- [73] <http://www.dlr.de/dlr/en/desktopdefault.aspx/tabid-10008/>. DLR WebPage.
- [74] <http://www.isas.jaxa.jp/e/index.shtml>. ISAS WebPage.
- [75] <http://www.cv.nrao.edu/course/ast534/InverseCompton.html>. National Radio Astronomy Observatory Courses.
- [76] G. Ghisellini, ed., *Radiative Processes in High Energy Astrophysics*, vol. 873 of *Lecture Notes in Physics*, Berlin Springer Verlag, 2013.
- [77] G. Risaliti and M. Elvis, “A panchromatic view of agn.” https://ned.ipac.caltech.edu/level5/March04/Risaliti/Risaliti_contents.html. NED WebPage.

- [78] B. Czerny and M. Elvis, “Constraints on quasar accretion disks from the optical/ultraviolet/soft X-ray big bump,” , vol. 321, pp. 305–320, Oct. 1987.
- [79] Ricci *et al.*, “Phd thesis.” http://www.isdc.unige.ch/~ricci/Website/AGN_in_the_X-ray_band.html. WebPage X-ray figure.
- [80] http://www.isdc.unige.ch/~ricci/Website/AGN_in_the_X-ray_band.html. WebPage X-ray figure.
- [81] The Fermi Collaboration, “The Second Catalog of Active Galactic Nuclei Detected by the Fermi Large Area Telescope,” , vol. 743, p. 171, Dec. 2011.
- [82] A. Abramowski *et al.*, “Flux upper limits for 47 AGN observed with H.E.S.S. in 20042011,” *Astron. Astrophys.*, vol. 564, p. A9, 2014.
- [83] W. Cui, “TeV Astrophysics, A Review,” in *Vulcano Workshop 2006: Frontier Objects in Astrophysics and Particle Physics Vulcano, Italy, May 22-27, 2006*, 2006.
- [84] J. H. Beall and W. Bednarek, “On the hadronic beam model for gamma-ray production in blazars,” *Astrophys. J.*, vol. 510, p. 188, 1999.
- [85] M. Boettcher, A. Reimer, K. Sweeney, and A. Prakash, “Leptonic and Hadronic Modeling of Fermi-Detected Blazars,” *Astrophys. J.*, vol. 768, p. 54, 2013.
- [86] R. J. Protheroe, A. C. Donea, and A. Reimer, “TeV gamma-rays and cosmic rays from the nucleus of M87, a mis-aligned BL Lac object,” *Astropart. Phys.*, vol. 19, pp. 559–568, 2003.
- [87] C. Patrignani *et al.*, “Review of Particle Physics,” *Chin. Phys.*, vol. C40, no. 10, p. 100001, 2016.
- [88] A. Reimer, “On the physics of hadronic blazar emission models,” *Journal of Physics: Conference Series*, vol. 355, no. 1, p. 012011, 2012.
- [89] P. Padovani, “Is there a relationship between bl lacertae objects and flat-spectrum radio quasars?,” *Monthly Notices of the Royal Astronomical Society*, vol. 257, no. 3, p. 404, 1992.

- [90] The Fermi Collaboration, “The First Catalog of Active Galactic Nuclei Detected by the Fermi Large Area Telescope,” , vol. 715, pp. 429–457, May 2010.
- [91] G. Ghisellini *et al.*, “The transition between BL Lac objects and flat spectrum radio quasars,” , vol. 414, pp. 2674–2689, July 2011.
- [92] Institute for Astronomy, University of Hawaii. https://ned.ipac.caltech.edu/level5/Padovani2/Pad_contents.html.
- [93] A. P. Marscher, “Relativistic jets and the continuum emission in QSOs,” , vol. 235, pp. 386–391, Jan. 1980.
- [94] A. Lawrence and M. Elvis, “Misaligned Discs as Obscurers in Active Galaxies,” *ArXiv e-prints*, Feb. 2010.
- [95] A. Barger, ed., *Supermassive Black Holes in the Distant Universe*. 2004.
- [96] H.-R. Klockner, W. A. Baan, and M. A. Garrett, “Investigation of the obscuring circumnuclear torus in the active galaxy Mrk 231,” *Submitted to: Nature*, 2003.
- [97] M. Elvis, “Slicing the Torus: Obscuring Structures in Quasars,” in *Journal of Physics Conference Series*, vol. 372 of *Journal of Physics Conference Series*, p. 012032, July 2012.
- [98] R. Maiolino, G. Risaliti, and M. Salvati, “The effect of bars on the obscuration of active nuclei,” *Astron. Astrophys.*, vol. 341, p. L35, 1999.
- [99] R. Antonucci, “Thermal and Nonthermal Radio Galaxies,” *ArXiv e-prints*, Jan. 2011.
- [100] R. R. J. Antonucci and J. S. Miller, “Spectropolarimetry and the nature of NGC 1068,” , vol. 297, pp. 621–632, Oct. 1985.
- [101] K. Pounds and S. Vaughan, “X-ray reflection in the nearby Seyfert 2 galaxy NGC 1068,” , vol. 368, pp. 707–714, May 2006.
- [102] “Hidden lair at the heart of galaxy ngc 1068.” <https://www.jpl.nasa.gov/spaceimages/details.php?id=PIA20058>. NASA WebPage.

- [103] <http://www.nuclear-power.net/nuclear-power/reactor-physics/interaction-radiation-matter/interaction-gamma-radiation-matter/>. WebPage for Picture.
- [104] M. Berger *et al.*, “Xcom: Photon cross sections database.” <http://www.nist.gov/pml/data/xcom/>. NIST Standard Reference Database.
- [105] P. Adamson *et al.*, “Search for Sterile Neutrinos Mixing with Muon Neutrinos in MINOS,” *Phys. Rev. Lett.*, vol. 117, no. 15, p. 151803, 2016.
- [106] C. Giunti and C. Kim, *Fundamentals of Neutrino Physics and Astrophysics*. 2007.
- [107] R. Gandhi, C. Quigg, M. H. Reno, and I. Sarcevic, “Ultrahigh-energy neutrino interactions,” *Astropart. Phys.*, vol. 5, pp. 81–110, 1996.
- [108] S. J. Brodsky and J. Pumplin, “Photon-Nucleus Total Cross-Sections,” *Phys. Rev.*, vol. 182, pp. 1794–1804, 1969.
- [109] “Deep underground neutrino experiment (dune).” <http://www.dunescience.org>. DUNE WebPage.
- [110] E. O’Sullivan, “Atmospheric Neutrino Status,” in *Neutrino Cross section Future*, 2016.
- [111] M. G. Aartsen *et al.*, “Atmospheric and astrophysical neutrinos above 1 TeV interacting in IceCube,” *Phys. Rev.*, vol. D91, no. 2, p. 022001, 2015.
- [112] “T2k experiment.” <http://t2k-experiment.org>. T2K WebPage.
- [113] “Jiangmen underground neutrino observatory (juno).” <http://english.ihep.cas.cn/rs/fs/juno0815/>. JUNO WebPage.
- [114] “Agua negra deep experiment site (andes).” <http://andeslab.org/index.php>. ANDES WebPage.
- [115] M. Ikeda *et al.*, “Search for Supernova Neutrino Bursts at Super-Kamiokande,” *Astrophys. J.*, vol. 669, pp. 519–524, 2007.
- [116] S. Hummer, M. Ruger, F. Spanier, and W. Winter, “Simplified models for photohadronic interactions in cosmic accelerators,” *Astrophys. J.*, vol. 721, pp. 630–652, 2010.

- [117] E. Fermi, “On the Origin of the Cosmic Radiation,” *Phys. Rev.*, vol. 75, pp. 1169–1174, 1949.
- [118] T. Sjostrand, S. Mrenna, and P. Z. Skands, “PYTHIA 6.4 Physics and Manual,” *JHEP*, vol. 05, p. 026, 2006.
- [119] M. G. Aartsen *et al.*, “All-sky Search for Time-integrated Neutrino Emission from Astrophysical Sources with 7 yr of IceCube Data,” *Astrophys. J.*, vol. 835, no. 2, p. 151, 2017.
- [120] S. van Velzen, H. Falcke, P. Schellart, N. Nierstenhöfer, and K. Kampert, “Radio galaxies of the local universe. All-sky catalog, luminosity functions, and clustering,” , vol. 544, p. A18, Aug. 2012.
- [121] P. Correa, “Bachelor thesis, vrije universiteit brussel, 2015..”
- [122] https://root.cern.ch/root/html526/MATH_MINUIT_Index.html. ROOT Documentation.
- [123] P. K. G. Williams and G. C. Bower, “Evaluating the Calorimeter Model with Broadband, Continuous Spectra of Starburst Galaxies Observed with the Allen Telescope Array,” , vol. 710, pp. 1462–1479, Feb. 2010.
- [124] C. D. Wilson, N. Rangwala, J. Glenn, P. R. Maloney, L. Spinoglio, and M. Pereira-Santaella, “Extreme Dust Disks in Arp 220 as Revealed by ALMA,” , vol. 789, p. L36, July 2014.
- [125] T. M. Yoast-Hull, J. S. Gallagher, S. Aalto, and E. Varenus, “Gamma-Ray Emission from Arp 220: Indications of an Active Galactic Nucleus,” *Mon. Not. Roy. Astron. Soc.*, vol. 469, p. L89, 2017.
- [126] Y. Uchiyama, C. M. Urry, C. C. Cheung, S. Jester, J. Van Duyne, P. Coppi, R. M. Sambruna, T. Takahashi, F. Tavecchio, and L. Maraschi, “Shedding New Light on the 3C 273 Jet with the Spitzer Space Telescope,” *Astrophys. J.*, vol. 648, pp. 910–921, 2006.
- [127] H. Falcke, E. Koerding, and S. Markoff, “A Scheme to unify low - power accreting black holes: Jet - dominated accretion flows and the radio / x-ray correlation,” *Astron. Astrophys.*, vol. 414, pp. 895–903, 2004.
- [128] A. Merloni, S. Heinz, and T. Di Matteo, “A Fundamental plane of black hole activity,” *Mon. Not. Roy. Astron. Soc.*, vol. 345, p. 1057, 2003.

- [129] P. Abreu *et al.*, “Measurement of the proton-air cross-section at $\sqrt{s} = 57$ TeV with the Pierre Auger Observatory,” *Phys. Rev. Lett.*, vol. 109, p. 062002, 2012.
- [130] J. Ahrens *et al.*, “Sensitivity of the IceCube detector to astrophysical sources of high energy muon neutrinos,” *Astropart. Phys.*, vol. 20, pp. 507–532, 2004.
- [131] R. Abbasi *et al.*, “The Design and Performance of IceCube DeepCore,” *Astropart. Phys.*, vol. 35, pp. 615–624, 2012.
- [132] The IceCube Collaboration, “Cosmic ray composition and energy spectrum from 1-30 PeV using the 40-string configuration of IceTop and IceCube,” *Astroparticle Physics*, vol. 42, pp. 15–32, Feb. 2013.
- [133] M. G. Aartsen *et al.*, “The IceCube Neutrino Observatory: Instrumentation and Online Systems,” *JINST*, vol. 12, no. 03, p. P03012, 2017.
- [134] The IceCube Collaboration, “First Neutrino Point-Source Results from the 22 String Icecube Detector,” , vol. 701, pp. L47–L51, Aug. 2009.
- [135] S. R. Klein, “IceCube: A Cubic Kilometer Radiation Detector,” *IEEE Trans. Nucl. Sci.*, vol. 56, pp. 1141–1147, 2009.
- [136] <http://www.scifun.ed.ac.uk/card/images/left/cosmic-rays.jpg>.
- [137] S. I. Dutta, M. H. Reno, I. Sarcevic, and D. Seckel, “Propagation of muons and taus at high-energies,” *Phys. Rev.*, vol. D63, p. 094020, 2001.
- [138] T. Feusels, J. Eisch, C. Xu, and for the IceCube Collaboration, “Reconstruction of IceCube coincident events and study of composition-sensitive observables using both the surface and deep detector,” *ArXiv e-prints*, Dec. 2009.
- [139] M. G. Aartsen *et al.*, “Characterization of the Atmospheric Muon Flux in IceCube,” *Astropart. Phys.*, vol. 78, pp. 1–27, 2016.
- [140] <http://software.icecube.wisc.edu/documentation/doxygen/linefit/>. IceCube Software Documentation.

- [141] S. Schoenen and L. R. for the IceCube Collaboration, “Detection of a multi-pev neutrino-induced muon event from the northern sky with icecube.” *The Astronomer’s Telegram* 7856, (2015).
- [142] S. Schoenen and L. R. on behalf of the IceCube Collaboration, “Detection of a multi-pev neutrino-induced muon event from the northern sky with icecube.” <http://www.astronomerstelegam.org/?read=7856>.
- [143] P. Desiati, T. Kuwabara, T. K. Gaisser, S. Tilav, and D. Rocco, “Seasonal Variations of High Energy Cosmic Ray Muons Observed by the IceCube Observatory as a Probe of Kaon/Pion Ratio,” in *Proceedings, 32nd International Cosmic Ray Conference (ICRC 2011): Beijing, China, August 11-18, 2011*, vol. 1, pp. 78–81, 2011.
- [144] “Seasonal variations in atmospheric muon rate.” <http://icecube.wisc.edu/~drocco/Wiki.pdf>. Internal IceCube Documentation.
- [145] “Tracking and data relay satellite (tdrs).” https://www.nasa.gov/directorates/heo/scan/services/networks/txt_tdrs.html. NASA WebPage.
- [146] J. Feintzeig, “Phd dissertation, searches for point-like sources of astrophysical neutrinos with the icecube neutrino observatory.” University of Wisconsin-Madison (2014).
- [147] “Icecube software documentation.” <http://software.icecube.wisc.edu/documentation/projects/neutrino-generator/index.html>.
- [148] “Karlsruhe institute of technology website.” <https://www.ikp.kit.edu/corsika/>. CORSIKA WebPage.
- [149] “Icecube software webpage.” <http://software.icecube.wisc.edu/documentation/>.
- [150] <http://grid.icecube.wisc.edu/simulation/dataset/11069>. IceCube Simulation Wiki Page.
- [151] <http://software.icecube.wisc.edu/documentation/projects/paraboloid/index.html>. IceCube Software Documentation.
- [152] O. Botner. <https://events.icecube.wisc.edu/getFile.py?access?sessionId=52&resId=0&materialId=0&confId=68>. Talk given at The IceCube Particle Astrophysics Symposium (2015).

- [153] J. Braun, J. Dumm, F. De Palma, C. Finley, A. Karle, and T. Montaruli, “Methods for point source analysis in high energy neutrino telescopes,” *Astropart. Phys.*, vol. 29, pp. 299–305, 2008.
- [154] C. Kopper, W. Giang, and N. Kurahashi, “Observation of Astrophysical Neutrinos in Four Years of IceCube Data,” *PoS*, vol. ICRC2015, p. 1081, 2016.
- [155] P. Correa. https://drive.google.com/file/d/0B8CXP-wGzu1_c2E3eTZsQ1FCbzA/view. Presentation given at the IIHE IceCube meeting, March 16, 2017.
- [156] https://wiki.icecube.wisc.edu/index.php/IC86_Muon_Level3 and http://code.icecube.wisc.edu/projects/icecube/browser/IceCube/sandbox/jfeintzeig/MuonL3_IC86/trunk/python/level3_Cuts.py. IceCube Documentation.
- [157] M. Honda, T. Kajita, K. Kasahara, S. Midorikawa, and T. Sannuki, “Calculation of atmospheric neutrino flux using the interaction model calibrated with atmospheric muon data,” *Phys. Rev.*, vol. D75, p. 043006, 2007.
- [158] W. Daelemans and K. Morik, eds., *Machine Learning and Knowledge Discovery in Databases*. Springer, 2008.
- [159] <http://software.icecube.wisc.edu/documentation/projects/pybdt/index.html>. IceCube Software Documentation.
- [160] S. Coender, private communication. <http://icecube.wisc.edu/~coenders/html/build/html/ic86-bdt/bdt.html#bdt-precut-and-high-level-reconstructions>.
- [161] N. van Eijndhoven, O. Fadiran, and G. Japaridze, “Implementation of a Gauss convoluted Pandel PDF for track reconstruction in Neutrino Telescopes,” *Astropart. Phys.*, vol. 28, pp. 456–462, 2007.
- [162] <http://software.icecube.wisc.edu/documentation/projects/CommonVariables/index.html>. IceCube Software Documentation.
- [163] The IceCube Collaboration, “Calibration and characterization of the IceCube photomultiplier tube,” *Nuclear Instruments and Methods in Physics Research A*, vol. 618, pp. 139–152, June 2010.

- [164] M. G. Aartsen *et al.*, “The IceCube Neutrino Observatory Part VI: Ice Properties, Reconstruction and Future Developments,” in *Proceedings, 33rd International Cosmic Ray Conference (ICRC2013): Rio de Janeiro, Brazil, July 2-9, 2013*, 2013.
- [165] E. V. Bugaev and Yu. V. Shlepin, “Photonuclear interaction of high-energy muons and tau leptons,” *Phys. Rev.*, vol. D67, p. 034027, 2003.
- [166] M. G. Aartsen *et al.*, “Observation of High-Energy Astrophysical Neutrinos in Three Years of IceCube Data,” *Phys. Rev. Lett.*, vol. 113, p. 101101, 2014.
- [167] M. Ahlers and F. Halzen, “Pinpointing Extragalactic Neutrino Sources in Light of Recent IceCube Observations,” *Phys. Rev.*, vol. D90, no. 4, p. 043005, 2014.
- [168] M. Kowalski, “Status of High-Energy Neutrino Astronomy,” *J. Phys. Conf. Ser.*, vol. 632, no. 1, p. 012039, 2015.

Appendices

Appendix A

Table with AGN in a limited volume sample and with a radio jet pointing towards Earth

The shown values are: declination “dec” (in degrees), right ascension “ra” (in degrees), redshift (z), frequency spectral index ($\alpha_R + \sigma_{\alpha_R}$) between 843 MHz and 5 GHz, the radio flux f_ν (Jy) at $1.4 \cdot 10^9$ [Hz] (radio) and the X-ray flux at $3.02 \cdot 10^{17}$ [Hz] (X-ray) for the 62 selected flat spectrum radio AGN.

Object name	dec	ra	$z \times 10^2$	$\alpha_R + \sigma_{\alpha_R}$	f_{ν}^{radio}	$f_{\nu}^{\text{X-ray}}$
1ES1215+303	30.12	184.47	13.00	-0.06	0.45	8.25e-06
NGC5506	-3.21	213.31	0.62	-0.44	0.34	6.15e-07
PKS2155-304	-30.23	329.72	11.60	-0.08	0.44	2.18e-05
3C371	69.82	271.71	5.10	0.08	2.26	8.79e-07
B21811+31	31.74	273.40	11.70	0.05	0.19	1.96e-07
RBS0958	20.24	169.28	13.92	0.98	0.10	1.11e-05
NGC1275	41.51	49.95	1.76	0.51	14.60	8.65e-05
SBS0812+578	57.65	124.09	5.39	-0.36	0.10	5.02e-07
Mkn180	70.16	174.11	4.53	-0.20	0.23	1.16e-05
PKS0447-439	-43.84	72.35	10.70	0.42	0.16	3.54e-06
PMNJ0152+0146	1.79	28.17	8.00	-0.05	0.06	1.28e-06
1H0323+022	2.42	51.56	14.70	1.04	0.07	3.99e-06
NGC2110	-7.46	88.05	0.78	-0.40	0.30	3.97e-07
NGC1052	-8.26	40.27	0.50	0.86	0.59	3.78e-08
GB6J1542+6129	61.50	235.74	11.70	0.31	0.10	1.71e-07
TXS2320+343	34.60	350.68	9.80	-0.09	0.10	3.61e-07
GB6J1053+4930	49.50	163.43	14.04	0.69	0.06	2.72e-07
3C273	2.05	187.28	15.83	0.04	42.61	1.88e-05
1H0323+342	34.18	51.17	6.10	-0.37	0.59	1.03e-06
B32247+381	38.41	342.52	11.87	0.72	0.10	8.11e-07
NGC4278	29.28	185.03	0.21	-0.19	0.40	1.97e-07
TXS1148+592	58.99	177.85	11.80	-0.09	0.18	2.67e-07
OQ530	54.39	214.94	15.26	0.26	0.87	3.54e-07
ARP220	23.50	233.74	1.81	-0.22	0.32	1.30e-08
Mkn421	38.21	166.11	3.00	-0.01	0.66	0.000
NGC3690	58.56	172.13	1.04	-0.49	0.71	1.37e-07
RGBJ1534+372	37.27	233.70	14.28	0.25	0.02	7.55e-08
1ES1440+122	12.01	220.70	16.31	0.24	0.06	2.59e-06
BLLacertae	42.28	330.68	6.86	-0.04	0.39	6.38e-07
SBS1200+608	60.52	180.76	6.56	-0.10	0.17	2.49e-07
2MASX	53.47	89.55	3.50	-0.38	0.40	2.65e-08
WComae	28.23	185.38	10.20	-0.40	0.68	4.30e-07
ON246	25.30	187.56	13.50	0.34	0.27	7.35e-07
1H1914-194	-19.36	289.44	13.70	-0.06	0.48	1.28e-06
PKS1349-439	-44.21	208.24	5.00	0.10	0.44	7.94e-07
S31741+19	19.59	265.99	8.40	-0.40	0.55	1.40e-06
PKS2005-489	-48.83	302.36	7.10	-0.08	1.26	1.63e-05
1ES0806+524	52.32	122.45	13.80	0.01	0.18	2.73e-06
PKS1424+240	23.80	216.75	16.00	-0.27	0.43	1.18e-06

Object name	dec	ra	$z \times 10^2$	$\alpha_R + \sigma_{\alpha_R}$	f_ν^{radio}	$f_\nu^{\text{X-ray}}$
4C+04.77	4.67	331.07	2.70	-0.27	0.40	2.54e-07
RXJ1136.5+6737	67.62	174.13	13.42	0.05	0.04	4.88e-06
NGC0262	31.96	12.20	1.50	0.77	0.29	4.08e-08
H1426+428	42.67	217.14	12.91	-0.13	0.03	1.08e-05
TXS1055+567	56.47	164.66	14.33	0.03	0.22	1.04e-06
Mkn501	39.76	253.47	3.37	-0.12	1.48	2.05e-05
1H1720+117	11.87	261.27	1.80	0.74	0.12	3.80e-06
RBS0970	42.20	170.20	12.40	0.25	0.02	2.58e-06
NGC6521	62.61	268.95	2.75	-0.24	0.29	2.58e-07
IZw187	50.22	262.08	5.54	-0.25	0.20	6.75e-06
UGC03927	59.68	114.38	4.05	-0.24	0.55	2.86e-07
IC4374	-27.02	211.87	2.18	-0.11	0.65	5.06e-06
NGC3628	13.59	170.07	0.28	-0.30	0.34	1.74e-09
1ES1959+650	65.15	300.00	4.70	-0.004	0.24	1.26e-05
PMNJ0847-2337	-23.62	131.76	6.07	0.08	0.14	8.48e-07
APLibrae	-24.37	229.42	4.90	-0.02	2.10	3.88e-07
MG1J010908+1816	18.27	17.28	14.50	0.60	0.09	1.49e-06
H2356-309	-30.63	359.78	16.54	-0.33	0.06	1.61e-05
CGCG186-048	35.02	176.84	6.31	-0.08	0.56	1.46e-07
PKS1717+177	17.75	259.80	13.70	-0.03	0.57	1.18e-07
MRK0668	28.45	211.75	7.66	0.86	0.72	1.27e-08
SBS1646+499	49.83	251.90	4.75	-0.01	0.18	2.88e-07
PKS1440-389	-39.14	220.99	6.55	0.07	0.11	3.16e-06

Appendix B

BDT Variables

Here we present the BDT variables that were used for my alternative event selection, and the standard Point Source event selection. Those were introduced in Chapter 7. The distributions below were plotted with the remaining events previous to the BDT performance. The distributions in red represent experimental background, whereas the curves in blue expose the distributions for NuMu simulated neutrino signal with E^{-2} spectrum.

Note that as indicated in the vertical axes, the distributions are normalized, which is done with the purpose of scaling both distributions. This normalization reflects,

$$\sum_{bins} \text{BinWidth} \times \text{BinHeight} = 1 \quad (\text{B.1})$$

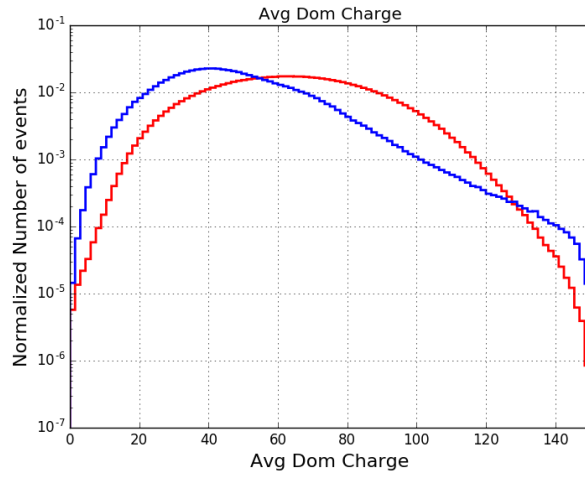


Figure B.1: AvgDomDistQTotDom.

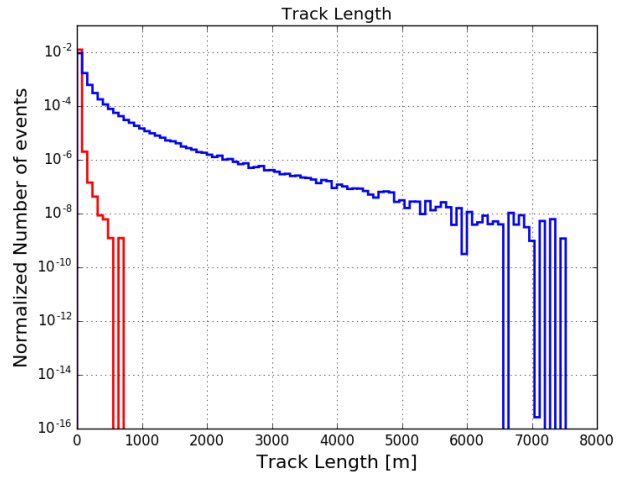


Figure B.2: DirTrackLength.

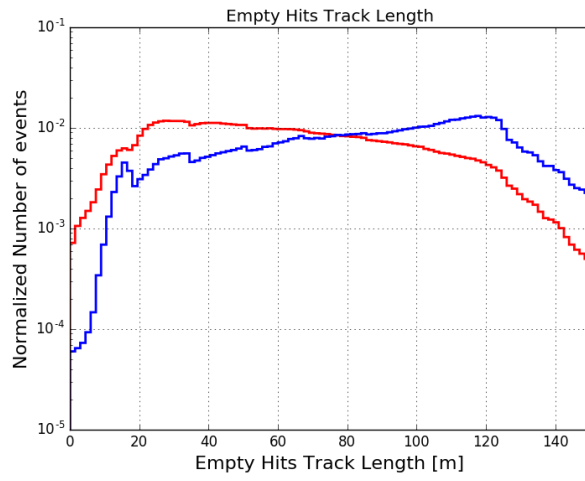


Figure B.3: EmptyHitsTrackLength.

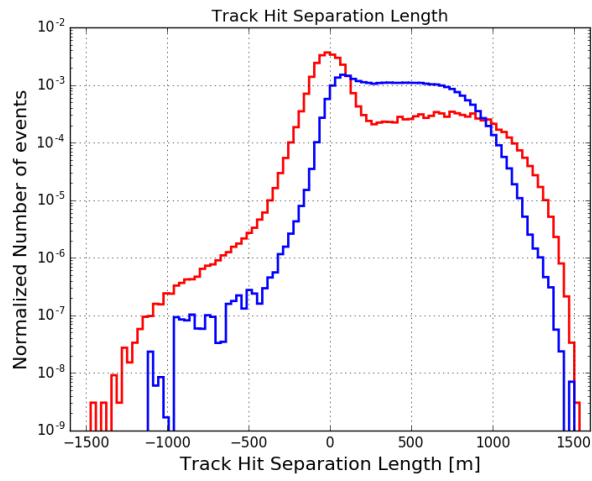


Figure B.4:

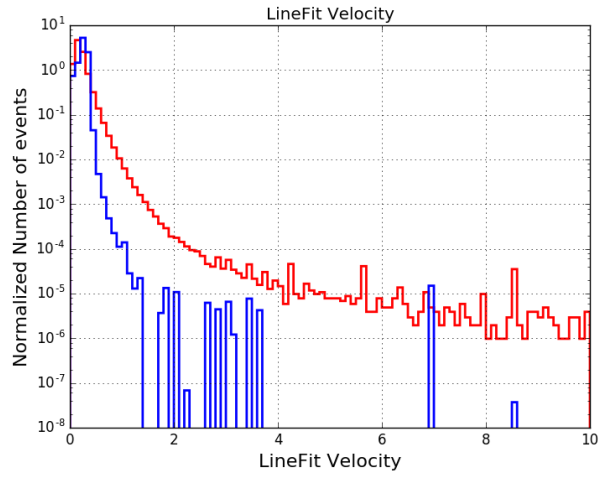


Figure B.5: LineFit-Velocity.

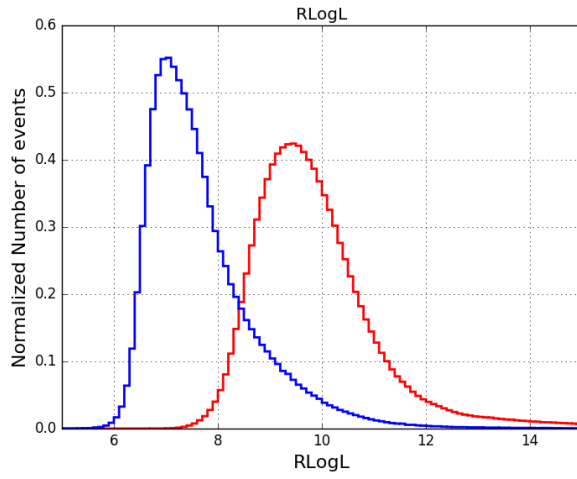


Figure B.6: RLogL-SplineReco.

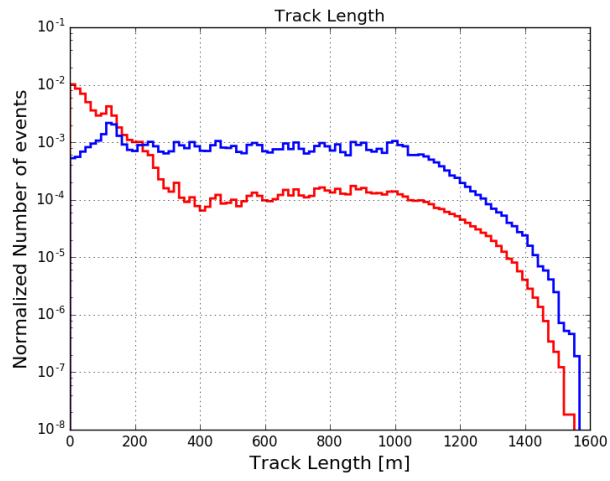


Figure B.7: DirTrackLength.

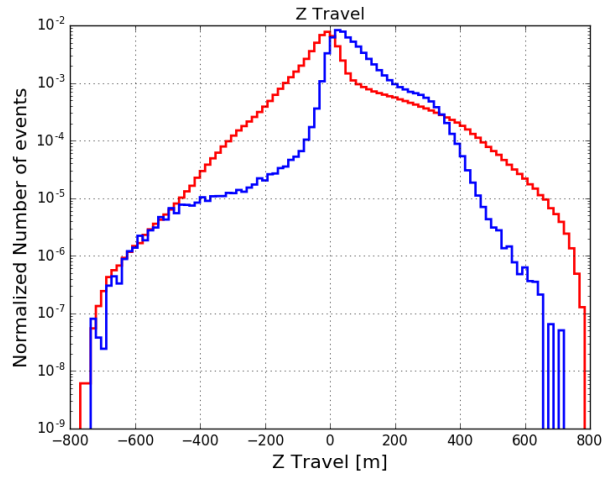


Figure B.8: ZTravel

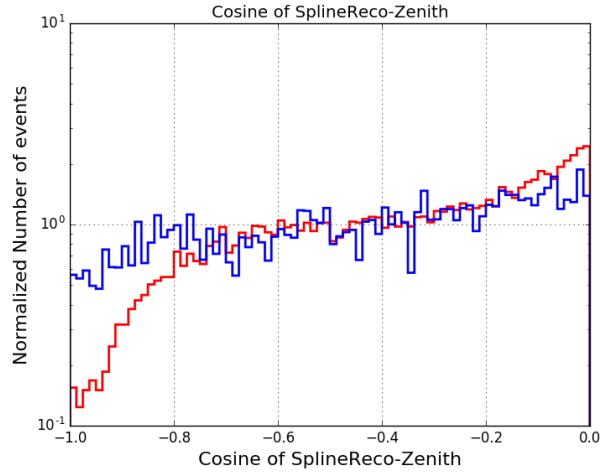


Figure B.9: Cosine of the zenith angle as defined by SplineReco. This is used in the Level3 for Point Source sample, and the files used to make this plot are located in /data/ana/Muon/level3/ at Madison.

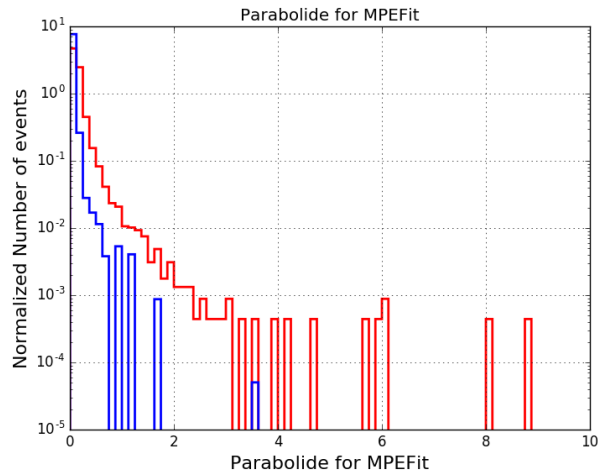


Figure B.10: MPEFit directional uncertainty estimator calculated by Parabolide. This is used in the Level3 for Point Source sample, and the files used to make this plot are located in /data/ana/Muon/level3/ at Madison.

Appendix C

Comparison between the Reprocessed Point Source and Diffuse Samples

In order to make sure that we are using the best available data set for this analysis, I decided to investigate the IceCube Diffuse data set as well, and compare it with the PSRepro sample. The comparison was made using the full year of data 2012, and the simulated data set 11069. Further information of the data set used for this comparison can be seen in table C.1. The small difference in the amount of experimental data, is due to the fact that two good runs are excluded in the diffuse sample. Those two runs had a very short lifetime, which probably was the reason to exclude them from the final diffuse sample. The difference in the amount of simulated files is due to what was found in the data warehouse of both samples. However, I take these differences into account when calculating the discovery potentials for both samples.

The diffuse sample already contains a SplineReco with energy estimator,

Data Type	Season	Amount of data
Exp	full 2012	331.38 (PSRepro), 331.35 (Dif) days
NuMu Sim	2012, DataSet 11069	6089 (PSRepro), 3920 (Dif) files

Table C.1: Data Set used to obtain the results that are presented in fig. C.1. The NuMu simulation data set is used as: E^{-2} spectrum. Dif indicates diffuse sample, and Exp refers to experimental data.

which is called in the diffuse sample “SplineMPEIC”. This sample is composed for tracks coming from the Northern Sky, hence, this contains events with a zenith larger (or equal) than 85 degrees as computed by SplineMPEIC. The container of pulses used for this reconstruction excludes the pulses from the DeepCore array. Furthermore, this differs from the one that I use in the seed for the reconstructed energy.

Note that the Diffuse sample does not have Paraboloid as angular estimator for the error on the SplineMPEIC reconstruction, therefore I had to run Paraboloid on the diffuse sample.

The comparison between the PSRepro and Diffuse sample is presented in fig. C.1. Here, the injected neutrino signal follows a power law of $\frac{d\Phi_\nu}{dE} \propto E^{-2}$. Therefore, there is no dependency on the signal spectral index γ_ν in the Likelihood formula as explained in Chapter 6, and the only parameter that directs the signal-background discrimination is the number of signal-like events n_s . From fig. C.1, it is seen that both samples agree rather well.

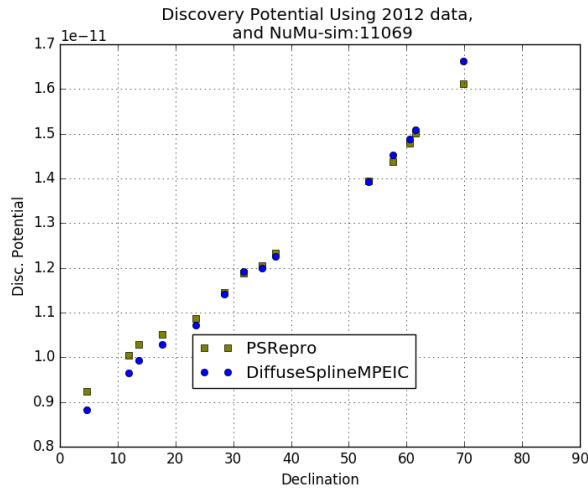


Figure C.1: Discovery potential comparison between the PSRepro and Diffuse sample. In this case, the Likelihood formula does not depend on the neutrino spectral index γ_ν . The discovery potential units are given in $[\text{TeV cm}^{-2}\text{s}^{-1}]$.

The comparison between the PSRepro and Diffuse sample with a γ_ν dependency in the Likelihood formula 6.1 was also checked. This comparison was made for different neutrino power laws (as the neutrino is emitted). The ratios between the discovery potentials obtained with the PSRepro sample

over the one achieved with the Diffuse sample are displayed in fig. C.2. The PSRepro sample shows an improvement with respect to the Diffuse sample mainly for sources at a declination above of 20° . For softer spectra, as $\gamma = 3$, the improvements are enhanced, which is based on the fact that the Diffuse sample keeps less events at low energy with respect to the PSRepro sample. Furthermore, since the reconstruction used in the Diffuse sample excludes the pulses in the DeepCore array at the IceCube detector, this loses accuracy at low energy.

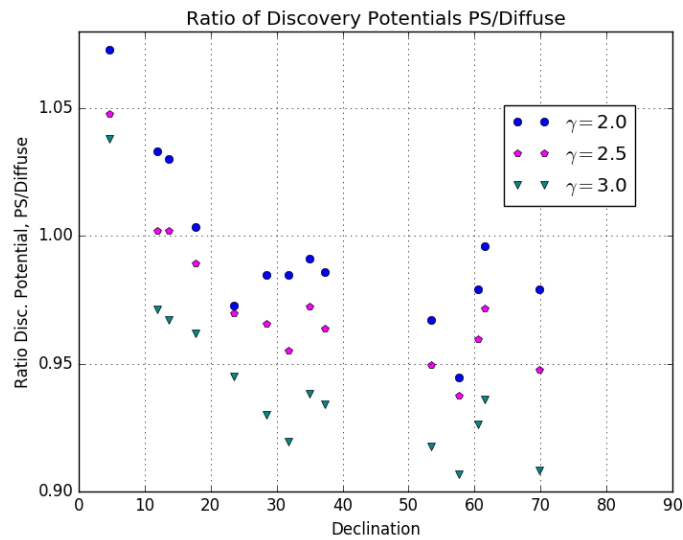


Figure C.2: Ratio of the discovery potentials obtained with the PSRepro and Diffuse sample. These ratios are shown for 3 different neutrino spectral index as they were emitted at the source.

Appendix D

Test Statistic Background Distribution for the Obscured Flat Spectrum Radio AGN

Here we present the test statistic background distribution for each object in the Obscured Flat Spectrum Radio AGN population as used for calculating the sensitivity-flux in table 8.1. Each distribution has been calculated by scrambling background events 10^5 times in right ascension. These events are contained in a declination range of 5° around the source position, and integrated in the whole right ascension, as reconstructed by SplineEnEst. Nevertheless, in order to ensure that there is no neutrino signal in this background distribution emitted from the sources in the Obscured Flat Spectrum Radio AGN population, and to profit from the fact that the IceCube sensitivity is invariant under an azimuthal rotation, the source position is shifted 180° in right ascension.

For each time that we scramble the background events, we obtain a test statistic value \mathcal{TS} , as described in Section 6.2. As eq. 6.5 exposes, \mathcal{TS} grows when $\mathcal{L}(\vec{x}_s, n_s, \gamma_\nu)$ increases with respect to $\mathcal{L}(\vec{x}_s, 0)$. The increase of the Likelihood $\mathcal{L}(\vec{x}_s, n_s, \gamma_\nu)$ is due to the fact that n_s grows as a consequence of the maximization and subsequent evaluation of the Likelihood at the parameter n_s (see section 6.1).

The vertical dashed-red line in the distributions below indicates the \mathcal{TS} value at which 5σ is reached, which I refer to as $\mathcal{TS}_{5\sigma}$. The latter is displayed in the figures below along the dashed-red line. In other words, the integrated

probability of the fit to all the normalized trial-entries with a \mathcal{TS} equal or larger than $\mathcal{TS}_{5\sigma}$ amounts to $2.87 \cdot 10^{-7}$.

The figures below also show the name of the each Obscured Flat Spectrum Radio AGN and its declination δ and right ascension α . Furthermore, in each figure, a diagonal dashed line is displayed, which fits the background test statistic distribution according to a χ^2 distribution. This fit is necessary to determine the test statistic value $\mathcal{TS}_{5\sigma}$, since as the figures expose, there are no entries at such \mathcal{TS} value. Obtaining statistically sufficient entries around the $\mathcal{TS}_{5\sigma}$ threshold would require at least 10^9 scrambling iterations, which is unrealistic in view of CPU time.

